UNIVERSITY OF CALIFORNIA SAN DIEGO

Array Processing for Atmospheric Sensing

A dissertation submitted in partial satisfaction of the
requirements for the degree
Doctor of Philosophy

in

Electrical Engineering (with a specialization in Signal and Image Processing)

by

Mark Wagner

Committee in charge:

       Professor Peter Gerstoft, Chair
       Professor William Hodgkiss
       Professor Ryan Kastner
       Professor Bhaskar Rao
       Professor Hee-chun Song

2020

The dissertation of Mark Wagner is approved, and it is acceptable in quality and form for publication on microfilm and electronically:

_____

_____

_____

_____

Chair

University of California San Diego

2020

DEDICATION

To the Electrical Engineering department at Umass Amherst, whose professors

inspired this degree.

TABLE OF CONTENTS

LIST OF FIGURES

ACKNOWLEDGEMENTS

Thanks to my advisor Professor Peter Gerstoft, who has supervised me gracefully through the years. Thanks to Santosh Nannuru and Yongsung Park, who have both given me inspiration in times when it was needed, and thank you Ali Dormiani for your contribution to designing, building, and maintaining the Noiselab Pier Array.

Thanks to all members of the Noiselab. The sense of community within the lab has been invaluable in my professional development.

Thanks to Ted Rogers at Space and Naval Warfare Systems Center, San Diego, CA. His helpful conversations have greatly influenced my work over the years.

This dissertation is a collection of papers that were published or submitted for publication. The text of Chapter Two is in full a reprint of the material as it appears in Mark Wagner, Peter Gerstoft, and Ted Rogers, "Estimating Refractivity from Propagation Loss in Turbulent Media," *Radio Science* 51.12 (2016): 1876-1894.

The text of Chapter Three is in full a reprint of the material as it appears in Mark Wagner, Santosh Nannuru, and Peter Gerstoft, "Compressive MIMO Beamforming of Data Collected in a Refractive Environment," *Radio Science* 52.12 (2017): 1458-1471.

The text of Chapter Four is in part and under some rearrangements a reprint of the material as it appears in Mark Wagner, Yongsung Park, and Peter Gerstoft, "Gridless DOA Estimation and Root-MUSIC for Non-Uniform Arrays," *IEEE Transactions on Signal Processing*, submitted 2020.

The text of Chapter Five is in part and under some rearrangements a reprint of material under preparation for submission as Mark Wagner, Herbert Groll, Ali Dormiani, Venkatesh Sathyanaryanan, Christoph Mecklenbräuker, and Peter Gerstoft, "Phase Coherent Electromagnetic Measurements in a Refractive Environment"

The dissertation author was the primary researcher and author, and the co-authors listed in these publications directed and supervised the research which forms the basis for this dissertation.

VITA

2014	B. S. in Electrical Engineering *cum laude*, University of Massachusetts Amherst
2016	M. S. in Electrical Engineering (Signal and Image Processing), University of California San Diego
2020	Ph. D. in Electrical Engineering (Signal and Image Processing), University of California San Diego
2011	Internship, CASA Radar Lab, University of Massachusetts Amherst
2012	Internship, MIT Lincoln Laboratory
2013	Research Assistant to Prof. Robert Jackson, University of Massachusetts Amherst
2016-2018	Teaching Assistant to Prof. Peter Gerstoft, ECE 228, Machine Learning for Physical Applications
2014-2020	Research Assistant to Prof. Peter Gerstoft, Noiselab director, University of California San Diego

PUBLICATIONS

Wagner, M., Gerstoft, P. and Rogers, T. "Estimating Refractivity from Propagation Loss in Turbulent Media", *Radio Science*, (2016).

Schamberg, G., Ba, D. and Wagner, M. "Efficient low-rank spectrotemporal decomposition using ADMM", *IEEE Statistical Signal Processing Workshop*, (2016).

Wagner, M., Nannuru, S. and Gerstoft, P. "Compressive MIMO Beamforming of Data Collected in a Refractive Environment", *Radio Science*, (2017).

Wagner, M., Bianco, M., Nannuru, S. and Gerstoft, P. "Array Shape Calibration Using Low Rank Projections", *52nd Asilomar Conference on Signals, Systems, and Computers. IEEE*, (2018).

Wagner, M. Park, Y. and Gerstoft, P."Gridless DOA Estimation via Alternating Projections?, International Conference on Acoustics, Speech, and Signal Processing, Brighton, UK, (2019).

Wagner, M. Park, Y. and Gerstoft, P. "Gridless DOA Estimation and Root-MUSIC for Arrays of Arbitrary Geometry", *submitted, IEEE Transactions on Signal Processing*, (2020).

Wagner, M. Groll, H., Dormiani, A., Sathyanarayanan, V. and Gerstoft, P. "Phase Coherent Electromagnetic Measurements in a Refractive Environment", *submitted, Radio Science*, (2020).

ABSTRACT OF THE DISSERTATION

Array Processing for Atmospheric Sensing

by

Mark Wagner

Doctor of Philosophy in Electrical Engineering (with a specialization in Signal and Image Processing)

University of California San Diego, 2020

Professor Peter Gerstoft, Chair

Refractivity is an important atmospheric parameter which determines the propagation speed of electromagnetic (EM) waves traveling through the lower troposphere. The vertical refractivity gradient of the atmosphere dictates how much the wavefront of a radio wave will bend away from a straight-line path from its transmitter. For instance, the refractivity profile over a terrestrial path generally causes radio waves to curve towards the Earth, effectively increasing the 'radio horizon' past that of the optical horizon. Over a marine channel however, the refractivity profile of the atmosphere can be highly variable and occasionally forms spurious natural waveguides known as 'ducts,' which allow for abnormally long range propagation and

other anomalous effects such as increased clutter and holes in radar measurements. As a result, it is desirable to be able to track the refractivity profile of the atmosphere to better predict and exploit the behavior of EM equipment in the presence of ducts.

Currently, the state-of-the-art in atmospheric refractivity research involves inference of the atmospheric refractivity profile from observations of the propagation loss from EM waves transmitted from a known location. Though this method has found some success, it is limited by the fact that there are often many refractivity profiles resulting in similar observed propagation loss. Thus, it is often impossible to know for certain the atmospheric refractivity profile from propagation loss alone.

In this dissertation, it is suggested that additional information about atmospheric refractivity can be found by measuring array specific parameters such as the direction of arrival (DOA) and array signal to noise ratio (ASNR) of a wavefront in addition to its propagation loss. The topic of DOA estimation is discussed in depth, from classical techniques to the advancement of state-of-the-art DOA estimation algorithms. The construction of a passive receiver array and first long term measurements of the DOA of an over the horizon signal propagating through a refractive marine channel are detailed. These measurements show that the time series of DOA and ASNR fluctuations correlate strongly with atmospheric parameters related to refractivity, implying that wavefront DOA and ASNR could be used to infer additional information about the atmospheric refractivity profile.

Chapter 1

Introduction

1.1   Background

In December 1901, Guglielmo Marconi transmitted the first wireless message across the Atlantic, from Cornwall, England to St John's, Canada. This was not the first proof that information could be sent and received from a distance without a physical wire connecting the two points of transmission, however, it was the first time that a wireless communication system had been proven practically useful and commercially marketable. Today, nearly every communication and remote sensing technology uses some form of wireless propagation. As a result, the understanding and modeling of the behavior of electromagnetic (EM) waves and their propagation paths has become an important topic of research.

The primary goal of this dissertation is to advance the understanding of radio wave propagation as it is observed in coastal maritime channels. In particular, the focus is towards shortfalls in the current state-of-the-art techniques for estimating the vertical refractivity profile of the atmosphere. Atmospheric refractivity has been a topic of research over the last half century because it causes many anomalous propagation phenomenon [1, 2, 3, 4, 5], thus it is desirable to be able to determine the refractivity structure of the atmosphere in order to predict its effects on

EM equipment.

The topics covered in this dissertation include,

1. *Electromagnetic Wave Propagation:* The behavior of EM waves of various wavelength as they propagate through a medium is covered in depth. The split step parabolic equation (PE) method [6, 7, 8] for simulating the path loss of a wave traveling through a refractive environment is used to demonstrate the expected propagation path of transmitted signals. We look at the effects of turbulence on the result of the PE method, and attempt to draw conclusions about how well a refractivity profile may be inferred from path loss measurements.

2. *Array Processing:* Array processing, particularly direction of arrival (DOA) estimation [9], is examined as a possible method for improving the estimation of the atmospheric refractivity profile. A chapter is devoted to the development of a novel gridless DOA estimation algorithm which can also be generalized to arrays of arbitrary geometry.

3. *Radio System Design:* In the final chapter of this work, a 24 element phase coherent passive receiver array is designed and built for the measurement of the DOA of over the horizon signals. This is the first such array of its kind, and measurements of the DOA and array signal to noise ratio (ASNR) of digital television signals are compared against propagation loss to determine if DOA and ASNR might hold additional information, possibly useful for improvement of future refractivity inversion.

1.2   Atmospheric Refractivity

Refraction is the change in direction of propagation of a wave due to the non-uniform speed of propagation at different points along its path. Because Earth's atmosphere is more dense towards the Earth's surface and the density of the atmosphere determines the speed of radio

waves propagating through it. Radio waves traveling through the atmosphere are known to refract towards Earth's surface. The refractive index, n, is defined as

$$n = c/v \,, \tag{1.1}$$

where c is the speed of light in vacuum and v is the speed of light in the medium. Near Earth's surface n is typically 1.000350. Because n is close to unity, another variable N known as *refractivity* is adopted for clarity

$$N = (n-1) \times 10^6 \,. \tag{1.2}$$

Atmospheric refractivity is a function of temperature T, pressure P, and partial water vapor e.

$$N = 77.6[P/T + 4810e/T^2] \,, \tag{1.3}$$

where P and e are measured in hectoPascals (hPa) and T is measured in Kelvin (K). When tracking the height of propagating electromagnetic waves over the earth's surface it becomes necessary to account for the curvature of the earth. A variable M, *modified refractivity*, is defined to transform the Earth to a flat surface:

$$M = N + (h/a) * 10^6 = N + .157h \,, \tag{1.4}$$

where h is height above earth's surface and a is the radius of the earth in km.

There are several well known propagation regimes which are typically defined by the gradient of $M(z)$, where z represents height above Earth's surface in meters. These propagation regimes include standard atmosphere ($0.079 \leq \frac{\partial M}{\partial z} \leq 0.157$ M-units/m), super-refraction ($0 \leq \frac{\partial M}{\partial z} < 0.079$ M-units/m), sub-refraction ($0.157 < \frac{\partial M}{\partial z}$ M-units/m), and ducting ($\frac{\partial M}{\partial z} < 0$ M-units/m) [10, 11]. Standard atmosphere and super-refraction result in radio waves bending slightly towards Earth's surface, while sub-refraction results in radio waves being bent away from Earth, into outer

space. Of the propagation regimes, ducting is often studied because it has a 'trapping' effect for EM waves caught within the duct. The result is that ducts act as naturally occurring waveguides capable of bending EM waves over the radio horizon to be detectable at significantly longer ranges than would otherwise be expected under any other refractive conditions.

1.2.1   Ducting

Whereas other propagation regimes are defined by a supposedly constant gradient in Earth's atmospheric refractivity profile, the refractivity profile associated with ducting has more specific structure. A duct is defined as any refractivity profile with a trapping layer, where the trapping layer of a duct is a region in which $\frac{\partial M}{\partial z} < 0$ [10]. The trapping layer can either start at the surface of the earth (surface based duct) or at some non-zero elevation (elevated duct). The trapping layer can be parameterized by its height, thickness, and the difference in modified refractivity between the top and bottom of the duct (known as M deficit).

An important subset of surface based ducts are known as evaporation ducts, which are common above water and are caused by a large humidity gradient just above the water's surface. Evaporation ducts can range in height from a few meters to several tens of meters, and are known to be common in warm coastal regions such as the Southern coast of California [12]. The seasonal frequency of ducting events is thought to be maximum in the summer months [13], though this is not certain because wide scale monitoring of atmospheric refractivity is not yet practical.

The dominant factor determining atmospheric refractivity is water vapor pressure (see (1.3)). The reason why ducting is most commonly observed in coastal and marine environments is because atmospheric processes involving hydrolapse (rapid change in moisture with height) often result in the formation of a duct. This is nearly always true directly over the ocean [14], and will most likely lead to an evaporation duct. Ducting is known to be particularly common over the Southern coast of California [15].

4

1.2.2 Refractivity from Propagation Loss

The adverse effects of ducting on radar measurements have been the driving force for many studies on EM propagation through refractive environments, most of which narrowly focus on received signal strength [16, 17, 18, 19, 20]. Many more studies have revolved around simulations of EM wave propagation through known refractive environments [7, 8], typically performed using some form of the parabolic equation (PE) method [6].

One strain of research, known as 'refractivity inversion' focuses on trying to infer the refractivity profile of the atmosphere from measurements of propagation loss. Propagation loss is typically taken from radar clutter, or simulated using the PE method. There is extensive literature on refractivity inversion techniques [2, 4, 21, 22].

In chapter 2, the method of estimating refractivity from propagation loss using PE simulation is examined with the addition of simulated atmospheric turbulence. The results somewhat call into question the fidelity of refractivity inversion given that the function mapping refractivity to propagation loss is not one to one. Additionally, turbulence in both the atmosphere and the measurements lead to significantly increased uncertainty in the results of the inversion. Finally, the non-convexity of the equations governing refractivity inversion result in difficult optimization problems that must be solved using sub-optimal methods. Despite uncertainty in the inversion, it is not difficult to identify whether a duct is or is not present, rather the difficultly lies in identifying the exact structure of the duct.

1.3 Direction of Arrival Estimation

The benefit of receiving wireless signals at an array of sensors rather than a single sensor is that by tracking the spatial phase pattern of the signal across the array, it is possible to determine the direction of arrival (DOA) of the wavefront. DOA is an array exclusive parameter in the sense that it can only be measured at an array. It is also one of the most well studied topic in the field

of signal processing. Recently, the focus of DOA estimation has turned from classical subspace based DOA algorithms including MUSIC, root-MUSIC, and ESPRIT [23, 24, 25, 26] to newer compressive sensing based methods such as compressive DOA estimation [27, 28, 29] capable of achieving higher resolution from fewer measurements.

An advantage of compressive DOA estimation is that the classic limitation requiring as many measurement snapshots as source signals no longer exists. However, compressive techniques are not without drawbacks. Compressive DOA estimation involves picking the DOAs composing the measurements as a linear combination of a few vectors from a user defined dictionary. Typically the dictionary represents an evenly spaced grid of possible DOAs, and because real signals do not lie neatly on a grid, the issue of 'grid mismatch' can arise.

As a response came the class of *gridless* DOA estimation algorithms [30, 31, 32], which attempt to explain the measurements as a sparse combination of *atoms* picked from a known manifold. Gridless DOA estimation methods are sometimes known as atomic norm minimization (ANM) techniques because they are based on the minimization of the atomic norm of a set of measurements.

In chapter 3, 2D compressive DOA estimation is applied to a set of over the horizon array measurements taken in a coastal environment to identify the direction of departure (DOD) and DOA of the wavefronts. The goal is to identify patterns associated with ducting towards determining if DOD and DOA can be informative measurements for refractivity inversion. As stated in section 1.2.2, up until this point, only propagation loss of a refracted signal has been explored towards refractivity inversion. By also taking into consideration the DOA of the wavefront, the refractivity inversion may be improved significantly.

In chapter 4 the theory of gridless DOA estimation is examined closely. Two major drawbacks of gridless DOA estimation are its complicated implementation, and that it exclusively applies to uniformly sampled signals, i.e. measurements taken at a uniform linear array. We introduce new theory which generalizes the Vandermonde decomposition of a Toeplitz matrix.

The generalization allows for gridless DOA estimation, as well as the classical root-MUSIC DOA estimation algorithm [23] to be extended to non-uniform arrays. It is also shown that the optimization involved in gridless DOA estimation need not be relaxed to a convex form. Instead, the non-convex optimization can be solved directly using the alternating projections algorithm [33, 34]. The proposed solution is shown to have speed and accuracy rivaling that of the convex approach whilst also being conceptually simpler.

Finally, in chapter 5 a 24 element, phase coherent receiver array is constructed for the purpose of measuring the DOA and array signal to noise ratio (ASNR) of long range signals of opportunity propagating over the horizon in a refractive environment. The purpose of the measurement campaign to determine if the DOA of over the horizon signals fluctuates measurably, and whether these measurements can be used to enhance refractivity inversion. Conclusions and a discussion on best future research directions are provided in chapter 6.

1.4   Thesis Overview

The overarching theme and conclusion of this research is summarized by the following statement:

> **Thesis Statement:** *Array exclusive measurements such as array signal to noise ratio and direction of arrival can likely be used to enhance the accuracy of refractivity inversion.*

In particular, this work has laid the groundwork for future studies to incorporate array measurements into refractivity inversion by proving,

1. A phase coherent array system can be constructed at relatively low cost from consumer available hardware and be used to measure variation in both the DOA and ASNR of EM signals propagating through a refractive environment.

2. The DOA of long range EM signals propagating through a refractive channel does vary by a measurable amount, and this variation is related to atmospheric conditions.

3. The ASNR of long range EM signals propagating through a refractive channel is better correlated with parameters associated with atmospheric refractivity than measurements of propagation loss by individual sensors.

Considering the main effect of atmospheric refractivity is to bend EM waves from their straight line path, it seems likely that DOA measurements contain some information about atmospheric refractivity that will eventually be used for refractivity inversion. The measurements from the array constructed in this work are, to our knowledge, the first experimental record conclusively showing long term DOA fluctuation in RF signals propagating over the horizon. While the final step of mapping DOA and ASNR measurements to specific refractivity profiles has not yet been attempted, the work contained herein constitutes the preliminary steps towards this goal.

Bibliography

[1] P. Gerstoft, D.F. Gingras, L.T. Rogers, and W.S. Hodgkiss, "Estimation of radio refractivity structure using matched-field array processing," *Antennas and Propagation, IEEE Transactions on*, vol. 48, no. 3, pp. 345–356, 2000.

[2] P. Gerstoft, L.T. Rogers, J.L. Krolik, and W.S. Hodgkiss, "Inversion for refractivity parameters from radar sea clutter," *Radio science*, vol. 38, no. 3, 2003.

[3] C.O. Ao, T.K. Meehan, G.A. Hajj, A.J. Mannucci, and G. Beyerle, "Lower troposphere refractivity bias in gps occultation retrievals," *J. Geophys. Research: Atmospheres*, vol. 108, no. D18, 2003.

[4] C. Yardim, P. Gerstoft, and W.S. Hodgkiss, "Estimation of radio refractivity from radar clutter using Bayesian Monte Carlo analysis," *IEEE Trans. Antennas. Prop.*, vol. 54, no. 4, pp. 1318–1327, 2006.

[5] P. Lopez, "A 5-yr 40-km-resolution global climatology of superrefraction for ground-based weather radars," *J. Appl. Meteorol. Climatol.*, vol. 48, no. 1, pp. 89–110, 2009.

[6] D.J. Thomson and N.R. Chapman, "A wide-angle split-step algorithm for the parabolic equation," *J. Acoust. Soc. Am.*, vol. 74, no. 6, pp. 1848–1854, 1983.

[7] G.D. Dockery, "Modeling electromagnetic wave propagation in the troposphere using the parabolic equation," *IEEE Trans. Antennas. Prop.*, vol. 36, no. 10, pp. 1464–1470, 1988.

[8] A.E. Barrios, "A terrain parabolic equation model for propagation in the troposphere," *IEEE Trans. Antennas. Prop.*, vol. 42, no. 1, pp. 90–98, 1994.

[9] T E. Tuncer and B. Friedlander, *Classical and modern direction-of-arrival estimation*, Academic Press, 2009.

[10] WL Patterson, "User?s manual for advanced refractive effect prediction system, space and naval warfare systems center, atmospheric propagation branch, san diego, ca, april 2005," .

[11] Merrill I Skolnik, *RADAR systems*, McGraw-Hill, NY, 2001.

[12] Q. Wang, K. Franklin, R. Yamaguchi, D.G. Ortiz-Suslow, D.P. Alappattu, C. Yardim, and R. Burkholder, "Ducting conditions during casper-west field campaign," in *2018 IEEE International Symposium on Antennas and Propagation*. IEEE, 2018, pp. 877–878.

[13] Q. Zhang, K. Yang, and Y. Shi, "Spatial and temporal variability of the evaporation duct in the gulf of aden," *Tellus A*, vol. 68, no. 1, pp. 29792, 2016.

[14] S.M. Babin, G.S. Young, and J.A. Carton, "A new model of the oceanic evaporation duct," *J. Applied Meteorology*, vol. 36, no. 3, pp. 193–204, 1997.

[15] R.A. Pappert and C.L. Goodhart, "Case studies of beyond-the-horizon propagation in tropospheric ducting environments," *Radio Sci.*, vol. 12, no. 1, pp. 75–87, 1977.

[16] V.W. Pidgeon, "Frequency dependence of radar ducting," *Radio Sci.*, vol. 5, no. 3, pp. 541–549, 1970.

[17] K.D. Anderson, "Radar detection of low-altitude targets in a maritime environment," *IEEE Trans. Antennas. Prop.*, vol. 43, no. 6, pp. 609–613, 1995.

[18] C.Y.D. Sim and E.M. Warrington, "Signal strength measurements at frequencies of around 300 mhz over two sea paths in the british channel islands," *Radio Sci.*, vol. 41, no. 03, pp. 1–13, 2006.

[19] W.T. Thompson and T. Haack, "An investigation of sea surface temperature influence on microwave refractivity: The wallops-2000 experiment," *J. Appl. Meteorol. Climatol.*, vol. 50, no. 11, pp. 2319–2337, 2011.

[20] Q. Wang, D.P. Alappattu, S. Billingsley, B. Blomquist, R.J. Burkholder, A.J. Christman, E.D. Creegan, T. De Paolo, D.P. Eleuterio, and H.J.S. Fernando, "Casper: Coupled air–sea processes and electromagnetic ducting research," *Bulletin of the American Meteorological Society*, vol. 99, no. 7, pp. 1449–1471, 2018.

[21] C. Yardim, P. Gerstoft, and W.S Hodgkiss, "Tracking refractivity from clutter using Kalman and particle filters," *IEEE Trans. Antennas. Prop.*, vol. 56, no. 4, pp. 1058–1070, 2008.

[22] A. Karimian, C. Yardim, P. Gerstoft, W.S. Hodgkiss, and A.E. Barrios, "Refractivity estimation from sea clutter: An invited review," *Radio Sci.*, vol. 46, no. 06, pp. 1–16, 2011.

[23] A. Barabell, "Improving the resolution performance of eigenstructure-based direction-finding algorithms," in *ICASSP'83. IEEE Inter. Conf. Acoustics, Speech, and Sig. Proc.* Citeseer, 1983, vol. 8, pp. 336–339.

[24] B.D. Rao and K.V. Hari, "Performance analysis of root-MUSIC," *IEEE Trans. Acoust., Speech, Signal Process.*, vol. 37, no. 12, pp. 1939–1949, 1989.

[25] M. Pesavento, A.B. Gershman, and M. Haardt, "Unitary root-music with a real-valued eigendecomposition: A theoretical and experimental performance study," *IEEE Trans. Sig. Proc.*, vol. 48, no. 5, pp. 1306–1314, 2000.

[26] H.L. Van Trees, *Optimum array processing: Part IV of detection, estimation, and modulation theory*, John Wiley & Sons, 2004.

[27] A. Xenaki, P. Gerstoft, and K. Mosegaard, "Compressive beamforming," *J. Acoust. Soc. Am.*, vol. 136, no. 1, pp. 260–271, 2014.

[28] A. Xenaki and P. Gerstoft, "Grid-free compressive beamforming," *J. Acoust. Soc. Am.*, vol. 137, no. 4, pp. 1923–1935, 2015.

[29] P. Gerstoft, A. Xenaki, and C.F. Mecklenbräuker, "Multiple and single snapshot compressive beamforming," *J. Acoust. Soc. Am.*, vol. 138, no. 4, pp. 2003–2014, 2015.

[30] G. Tang, B.N. Bhaskar, P. Shah, and B. Recht, "Compressed sensing off the grid," *IEEE Trans. Inf. Theory*, vol. 59, no. 11, pp. 7465–7490, 2013.

[31] E.J. Candès and C. Fernandez-Granda, "Towards a mathematical theory of super-resolution," *Commun. Pure Appl. Math.*, vol. 67, no. 6, pp. 906–956, 2014.

[32] Z. Yang and L. Xie, "On gridless sparse methods for line spectral estimation from complete and incomplete data," *IEEE Trans. Signal Process.*, vol. 63, no. 12, pp. 3139–3153, 2015.

[33] J. von Neumann, *Functional Operators, Volume 2: The Geometry of Orthogonal Spaces.*, vol. 2, Princeton University Press, 1951.

[34] H. Attouch, J. Bolte, P. Redont, and A. Soubeyran, "Proximal alternating minimization and projection methods for nonconvex problems: An approach based on the Kurdyka–Lojasiewicz inequality," *Math. Oper. Res.*, vol. 35, no. 2, pp. 438–457, 2010.

Chapter 2

Estimating Refractivity from Propagation Loss in Turbulent Media

This chapter estimates lower atmospheric refractivity (M-profile) given an electromagnetic (EM) propagation loss (PL) measurement. Specifically, height-independent PL measurements over a range of 10-80 km are used to infer information about the existence and potential parameters of atmospheric ducts in the lowest 1 km of the atmosphere. The main improvement made on previous refractivity estimations is inclusion of range-dependent fluctuations due to turbulence in the forward propagation model. Using this framework, the maximum likelihood (ML) estimate of atmospheric refractivity has good accuracy, and with prior information about ducting the maximum a priori (MAP) refractivity estimate can be found. Monte Carlo methods are used to estimate the mean and covariance of PL, which are fed into a Gaussian likelihood function for evaluation of estimated refractivity probability. Comparisons were made between inversions performed on propagation loss data simulated by a wide angle parabolic equation (PE) propagation model with added homogeneous and inhomogeneous turbulence. It was found that the turbulence models produce significantly different results, suggesting that accurate modeling of turbulence is key.

2.1 Introduction

Refractivity of a medium represents the amount which an electromagnetic (EM) wave will bend while propagating through the medium. Atmospheric refractivity is of particular interest because there exist common height-varying refractivity profiles, which act as waveguides for EM waves, known as ducts. The atmospheric inversion layer is primarily responsible for ducts and separates the colder and more humid mixed layer from the free troposphere; thus, there exists a large negative humidity gradient. Turbulence in the inversion layer will cause more humidity variation in that layer relative to other layers. This will cause more refractivity fluctuations in the inversion layer.

Ducting is a naturally occurring event that is known to cause anomalies in long range EM equipment. Examples of these anomalies include unusually long operational range or increased clutter in return signals. For operators of EM equipment it is beneficial to know when a ducting phenomenon is occurring to better understand the possible effects on system performance. Thus, it is desirable to have some way to characterize the qualities of a duct from simple measurements. Because it is known that variation in atmospheric refractivity causes variation in PL measurements [1], it may be possible to infer a refractivity profile from PL.

From a range independent refractivity profile parameterized by $\mathbf{m}$ (defined in section 2.2.1), a deterministic matrix of PL over height and range can be computed from a forward model $F(\mathbf{m})$ (defined in section 2.3). The parabolic equation (PE) method is used for this calculation [2]. The forward model can be used to find the appropriate M-profile that statistically best recreates a measured PL.

Turbulence, parameterized by C_n^2, causes random fluctuations in refractivity [3], which in turn propagate through the forward model, $F(\mathbf{m}, C_n^2)$ resulting in fluctuations in PL obeying an unknown distribution. C_n^2 is a parameter relating to the magnitude of fluctuations in refractivity from atmospheric turbulence. Stochastic variation in the forward model is expected to increase

with range due to the compounding effect of fluctuations as they propagate forward [4]. As a result, even small perturbations in refractivity can lead to large changes in PL at longer distances.

For inversion, the effects of turbulence mean:

1. The forward model for PL, $F(\mathbf{m}, C_n^2)$, is now stochastic. As a result, a means to calculate an average PL vector given $\mathbf{m}$ and C_n^2 becomes important.

2. The fluctuations in refractivity will have an effect on fluctuations in PL. The distribution of refractivity fluctuations must be modeled, as well as the distribution of the resulting fluctuations in PL.

3. The uncertainty in the PL vector will increase with range. In previous inversions [5, 6, 7, 8] uncertainty was assumed range independent, an assumption which does not hold when turbulence is present. This time a full covariance matrix of PL, $\mathbf{C}_d$, must be calculated to find the likelihood of a measurement given $\mathbf{m}$ and C_n^2.

This work attempts to build upon previous efforts to estimate refractivity from clutter [9], [10], [5] with the added component of randomness from atmospheric turbulence. The primary goals are to find an accurate method of modeling turbulence and to describe the effect on refractivity estimations.

2.2 Theory

2.2.1 Refractivity

Bending of the propagation path of an electromagnetic wave due to variation in the speed of light is known as refraction, and is the cause of ducting phenomenon. The refractive index n is defined as

$$n = c/v \, , \tag{2.1}$$

where c is the speed of light in vacuum and v is the speed of light in the medium being propagated through. Near the earth's surface n is typically 1.000350. Because n is close to unity, another variable N known as refractivity is adopted for clarity

$$N = (n-1) \times 10^6 .$$ (2.2)

Atmospheric refractivity is a function of temperature T, pressure P, and partial water vapor e.

$$N = 77.6[P/T + 4810e/T^2] ,$$ (2.3)

where P and e are measured in hectoPascals (hPa) and T in Kelvin (K). When tracking the height of propagating electromagnetic waves over the earth's surface it becomes necessary to account for the curvature of the earth. A variable M, Modified refractivity, is defined to transform the earth to a flat surface:

$$M = N + (h/a) * 10^6 = N + .157h ,$$ (2.4)

where h is height above earth's surface and a is the radius of the earth in km.

In the radar community, atmospheric ducts are represented by a refractivity profile which varies with height, but is often assumed to be range independent. A sample M-profile representing the case where both an evaporation and surface-based duct exists is shown in Fig. 2.1. It is only necessary to know a few deterministic parameters of a refractivity profile for adequate description of the propagation environment [11], so we limit description of the refractive environment to five variables organized into vector $\mathbf{m}$, with elements m_i representing the ith parameter. From $\mathbf{m}$ all realistic M-profiles can be constructed. The five parameters are shown in Figure 2.1.

An M-profile can be generated from $\mathbf{m}$ and used as input to the forward model, which is an electromagnetic wide angle split step fast Fourier transform PE [12, 13]. The forward model is set with parameters of the wave in question which includes transmitter height, max range
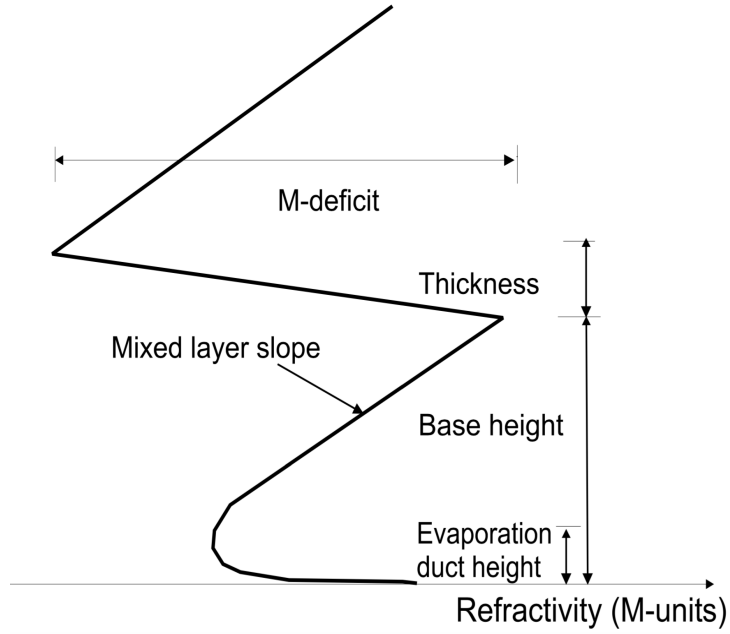
Figure 2.1: Refractivity profile representing a ducting phenomenon.

of propagation, frequency, height and range step size, height of measurements, and maximum

propagation angle (and will later also take in turbulence structure coefficient of the atmosphere,

C_n^2). The forward model calculates PL of the specified wave over height and range. Because

realistic measurements of PL are generally taken at one height, only the height of measurement

is kept. This height is an internal parameter of the model which can be altered to match the

situation being simulated. The output, $F(\mathbf{m})$, of the forward model is an N_f dimensional vector

corresponding to the theoretical propagation loss at the given height.

2.2.2 Turbulence

When the forward model $F(\mathbf{m})$ is run, a deterministic output is generated which can be

exactly recomputed given an identical input $\mathbf{m}$. In reality, the propagation pattern of an EM

wave through a steady duct shows short-term fluctuations. This is because turbulence causes

atmospheric variables such as temperature, pressure, and vapor pressure to fluctuate constantly,

which in turn cause the mean refractivity profile to fluctuate constantly and results in the scattering

of waves propagating through the atmosphere [14]. This section adds stochastic fluctuations to the refractivity profile so that the forward model can realistically reflect randomness introduced by turbulence.

Stochastic Elements of Refractivity

It is assumed that the M-profile is subject to continuous fluctuations due to atmospheric turbulence. To model fluctuations in refractivity due to turbulence the refractivity profile is split into two parts: a range independent mean refractivity $\langle n(z) \rangle$, and a stochastically fluctuating part $\tilde{n}(x,z)$

$$n(x,z) = \langle n(z) \rangle + \tilde{n}(x,z) \ . \tag{2.5}$$

where $\langle . \rangle$ represents mean. While $\langle n(z) \rangle$ is deterministic and can be fully specified by $\mathbf{m}$, $\tilde{n}(z)$ is stochastic and requires a spectrum to generate realizations.

Structure Function

The structure function is defined as the covariance of the difference of a process between position vector r and $r + \Delta r$ where Δr is a displacement vector from starting location r [15].

$$D_n(r, \Delta r) = \langle [n(r) - n(r + \Delta r)]^2 \rangle \tag{2.6}$$

where $n(r)$ is the refractivity at point r. If we assume that the structure function is identical from all starting positions and orientations (which is the assumption of local homogeneity), then equation (2.6) becomes a functions of just $\mathbf{r} = |\Delta r|$. Local homogeneity is an assumed in Kolmogorov's second similarity hypothesis [16]. Using dimensional analysis, it was concluded that the structure function of a medium-scale turbulent field is a function of distance $\mathbf{r}$ from the starting location and obeys

$$D_n(\mathbf{r}) \propto C_n^2 \mathbf{r}^{2/3} \tag{2.7}$$

17

where C_n^2 is the structure function constant of the subscripted variable n and represents the magnitude of $\tilde{n}(z)$. Note that (2.7) applies only to medium-scale fluctuations. Structure functions of large and small-scale fluctuations are modeled by different equations because the shape of their spectrums is modeled differently than that of medium-scale fluctuations [17].

Equation (2.7) is known as the simplified Kolmogorov's 2/3 law and condenses all unknowns into the structure function constant C_n^2. The structure function constant can be obtained from physical measurement; however, it is known that its value changes with height above the boundary layer. We initially assume height independence of C_n^2 to preserve the assumption of homogeneity. Later we redact this assumption and observe the effect on the accuracy of our inversion.

Modeling Turbulence

We choose a robust spectral model that has been used in similar studies known as the von Karman spectrum, visualized in Fig. 2.2.

$$S_n(\kappa) = .033 C_n^2 (\kappa^2 + L_0^{-2})^{-11/6} \exp\left(-\kappa^2/\kappa_m^2\right),\tag{2.8}$$

where κ represents wave number, $\kappa_m = 5.92/l_0$ (known as the inner scale wavenumber parameter), and l_0 is the boundary between medium and small scale fluctuations, L_0 is the boundary between large and medium scale fluctuations known as the integral length scale. The major advantage of the von Karman spectrum is that it approximates Kolmogorov's power law for spatial frequencies $L_0^{-1} < \kappa < l_0^{-1}$ and allows for tuning at other wave numbers. The von Karman spectrum is attractive for its simplicity; however, the algorithm is robust enough that it may be replaced for more accurate spectral models if desired. Additionally, the assumption of homogeneous turbulence in the marine boundary layer is less accurate [18], and will be addressed in section 2.2.3.
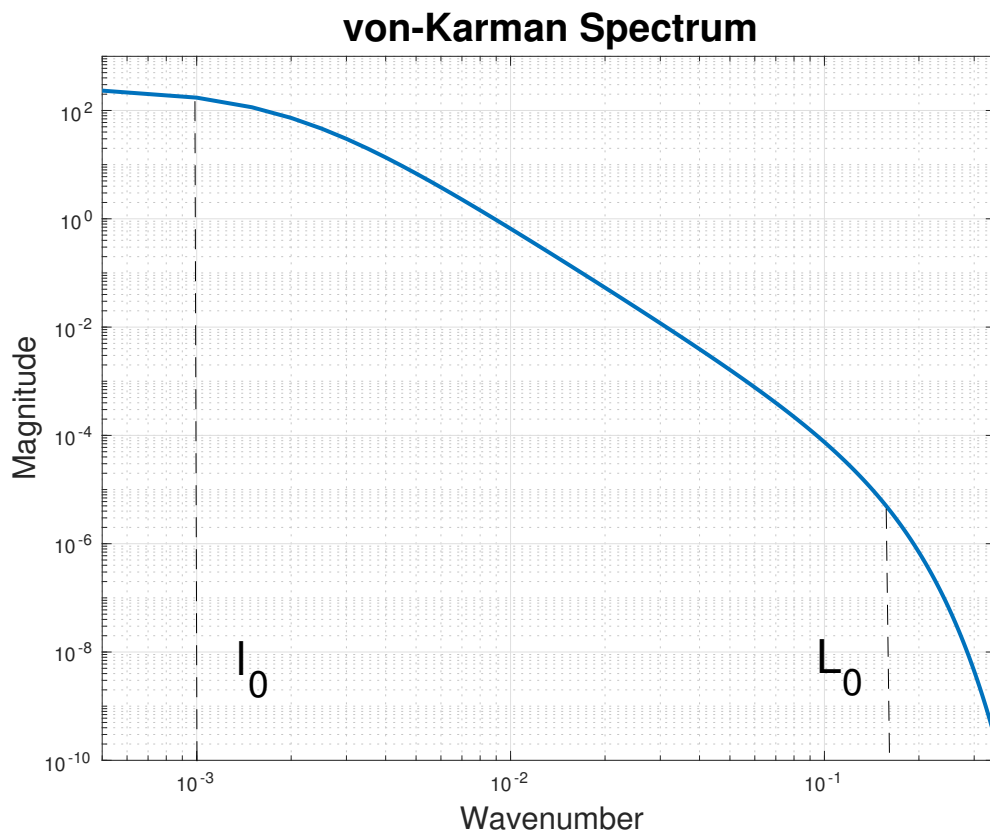
Figure 2.2: von Karman spectrum divided into large, medium, and small scale subranges.

Realizations of $\tilde{n}(z)$ are found using [19]. An approximate realization U_z of the M point spectrum $S_n(\kappa)$ can be generated using the equation

$$\tilde{n}(z) = U_z = \frac{1}{\sqrt{M}} \sum_{k=0}^{M-1} U_k \exp^{-j2\pi\varepsilon_k z} \tag{2.9}$$

where $\varepsilon_k = \frac{k}{M}\varepsilon_{max}$, ε_{max} is the Nyquist spatial frequency of the desired signal, $j = \sqrt{-1}$, and U_k is defined as

$$U_k = \begin{cases} \sqrt{S_n(0)}W_0, & k = 0 \\ \sqrt{\frac{1}{2}S_n(\varepsilon_k)}(W_{2k-1} + jW_{2k}), & 1 \le k < \frac{M}{2} \\ \sqrt{S_n(\varepsilon_{max})}W_{M-1}, & k = \frac{M}{2} \\ U_k = U_{M-k}^*, & \frac{M}{2} < k \le M-1 \end{cases} \tag{2.10}$$

Here S_n is the spectrum from which the realizations must match, and W_k is the kth element of a sequence drawn from $N(0,1)$. Intuitively, (2.10) is creating a signal which is the product of Gaussian noise and an envelope spectrum which will have a purely real inverse Fourier transform. Equation (2.9) simply transforms the end result of (2.10) to a vector which is considered an accurate realization of turbulent noise over height. In practice we generate many independent realizations of $\tilde{n}(z)$ which are used to model turbulence over a large scale 2 dimensional grid representing height and range. Simulations of PL with and without turbulent noise are shown in Fig. 2.3.

2.2.3 Inhomogeneous Turbulence

The marine atmospheric boundary layer (MABL) is a turbulent stratified flow. When fully developed, it consists of a surface layer, mixed layer, and an entrainment zone (often an inversion layer) under the free troposphere. The pressure gradients and geostrophy in the free troposphere produce the wind forcing on the boundary layer. The MABL is evolving continuously in time and space (e.g., a continuous injection of moisture from ocean surface evaporation, radiant heating,
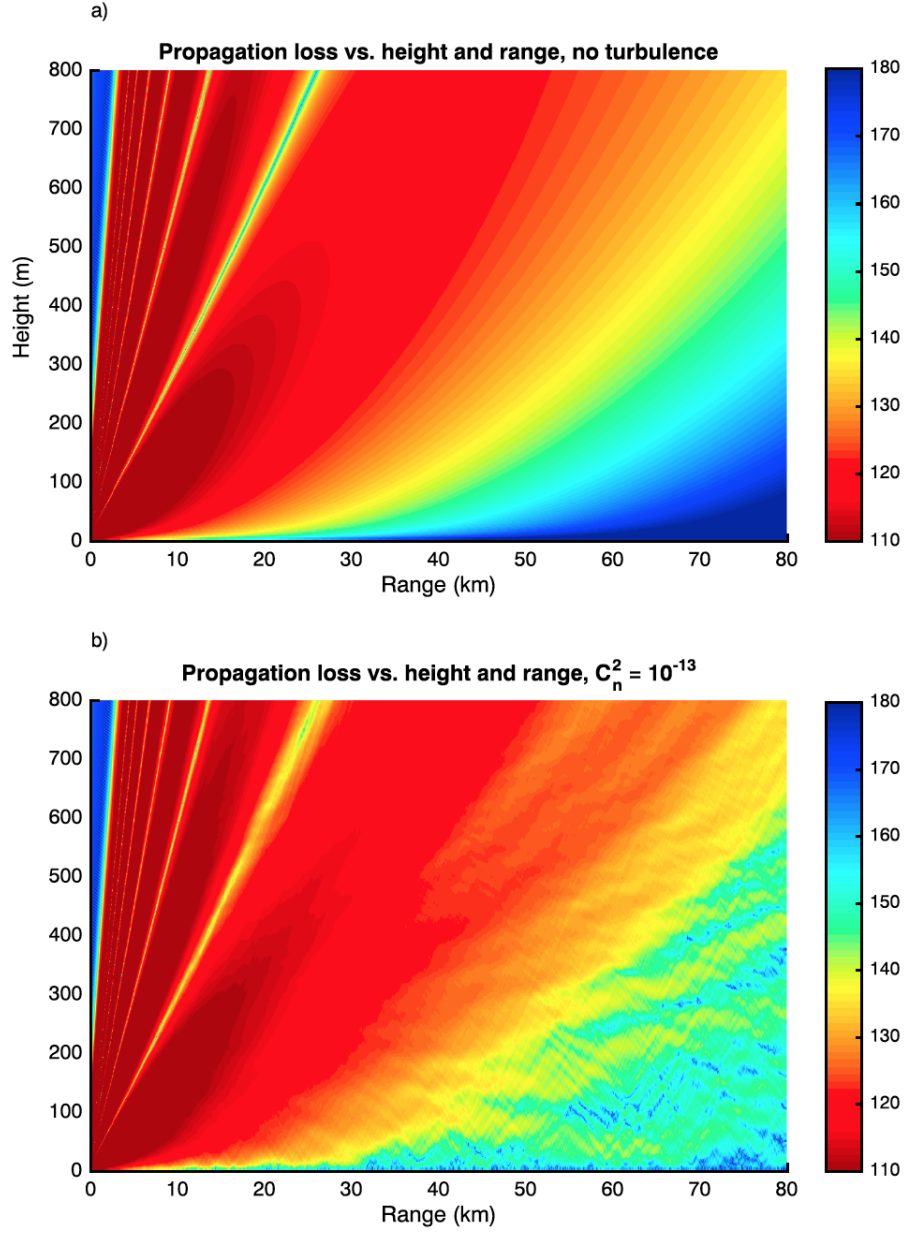
Figure 2.3: Propagation loss (PL) at 1 GHz propagating through standard atmosphere refractivity profile over height and range, (a) without turbulence, (b) with turbulence parameterized by $C_n^2 = 10^{-13}$.

and cooling). However, the rate of change in the horizontal is much less than in the vertical. If the mass of a MABL layer is constant, the horizontal pressure gradient and the stresses at each interface sum to zero. The stress at the ocean arises from the friction between the surface layer and the ocean. Above that, combinations of stability and shear provide the balance of stresses and the horizontal pressure gradient at each layer. Higher stability (associated with a positive virtual potential temperature gradient) dampens turbulence, while more shear gives more turbulence. The mixed layer is (nearly) neutrally stable and with low shear, but in the inversion layer both stability and shear are much larger. The point is that turbulence in the inversion layer might not be greater or smaller than in the mixed layer.

Eddies, however, displace particles such that air samples at a given height have a distribution of water vapor content corresponding to the horizontal mean properties of the air at nearby heights. Thus, the stronger the magnitude of water vapor gradient, the larger the variance of the water vapor at that height. Since water vapor is the dominant term in the refractivity, the variability of refractivity can be much larger in the inversion layer than in the mixed layer.

Use of numerical simulation techniques such as Large Eddy Simulation (LES) [20] has shown that the magnitude of $\tilde{n}(z)$ can increase more than ten-fold near the inversion layer of a duct. This implies that C_n^2 varies over height when a duct is present, hitting a maximum in the middle of the inversion layer and returning to a nearly constant value above the duct. We attempt to model fluctuations subject to height-varying $C_n^2(z)$ and refer to turbulence generated under this model as inhomogeneous turbulence.

A simulation of inhomogeneous turbulence was conducted by changing C_n^2 from a constant value to a function of height, $C_n^2(z)$, then generating corresponding realizations of $\tilde{n}(z)$. A simple formula was created for $C_n^2(z)$ which models an increase in C_n^2 around the middle of a ducts inversion layer.

$$C_n^2(z) = C_s \left[1 + K \exp \left(\frac{-(z - (m_3 + \frac{m_4}{2}))^2}{(\frac{m_4}{2})^2} \right) \right] \tag{2.11}$$

22

where C_s represents the reference value of C_n^2, m_3 and m_4 are the base height and thickness of the duct respectively, and K can be adjusted to give any desired maximum to the function $C_n^2(z)$. Eq (2.11) creates a C_n^2 profile which increases $(1 + K)$ fold at the inversion layer. Approximate realizations of $n_{ih}(z)$ following (2.11) are generated as follows,

$$n_{ih}(z) = \tilde{n}(z) \left[1 + K \exp \left(\frac{-(z - (m_3 + \frac{m_4}{2}))^2}{(\frac{m_4}{2})^2} \right) \right] \tag{2.12}$$

where $n_f(z)$ is generated using $C_n^2 = C_s$. It has been shown that (2.12) produces accurate realizations of $n_{ih}(z)$ [21] if the medium can be assumed quasi homogeneous, an assumption which is popular in similar wave propagation studies [22], [23].

For inversions in the preceding examples, (2.12) is used to generate inhomogeneous turbulence with $K = 9$ to achieve a tenfold increase in C_n^2 at the inversion layer. The increase in C_n^2 makes refractivity fluctuations larger just below the duct interface by increasing turbulent fluctuations. [20] suggests this is more consistent with reality than constant $C_n^2(z)$. The forward model was run on two refractivity profiles with identical parameters except for m_5, representing M-deficit. The two values of m_5 used change the profile from a surface based duct to an elevated duct. Results of the forward model runs using both homogeneous and inhomogeneous turbulence models are shown in Figures. 2.4, and 2.5. Theoretically, only surface based ducts should cause trapping of propagating waves between the duct height and earths surface [24], Fig. 2.5 shows that the inhomogeneous turbulence model can produce similar trapping in elevated ducts.

2.3   Stochastic Forward Model

As previously stated, a PE method [25] is used to calculate the amplitude $U(x,z)$ of propagative EM fields over a grid of ranges x and heights z. The PE method is derived from the
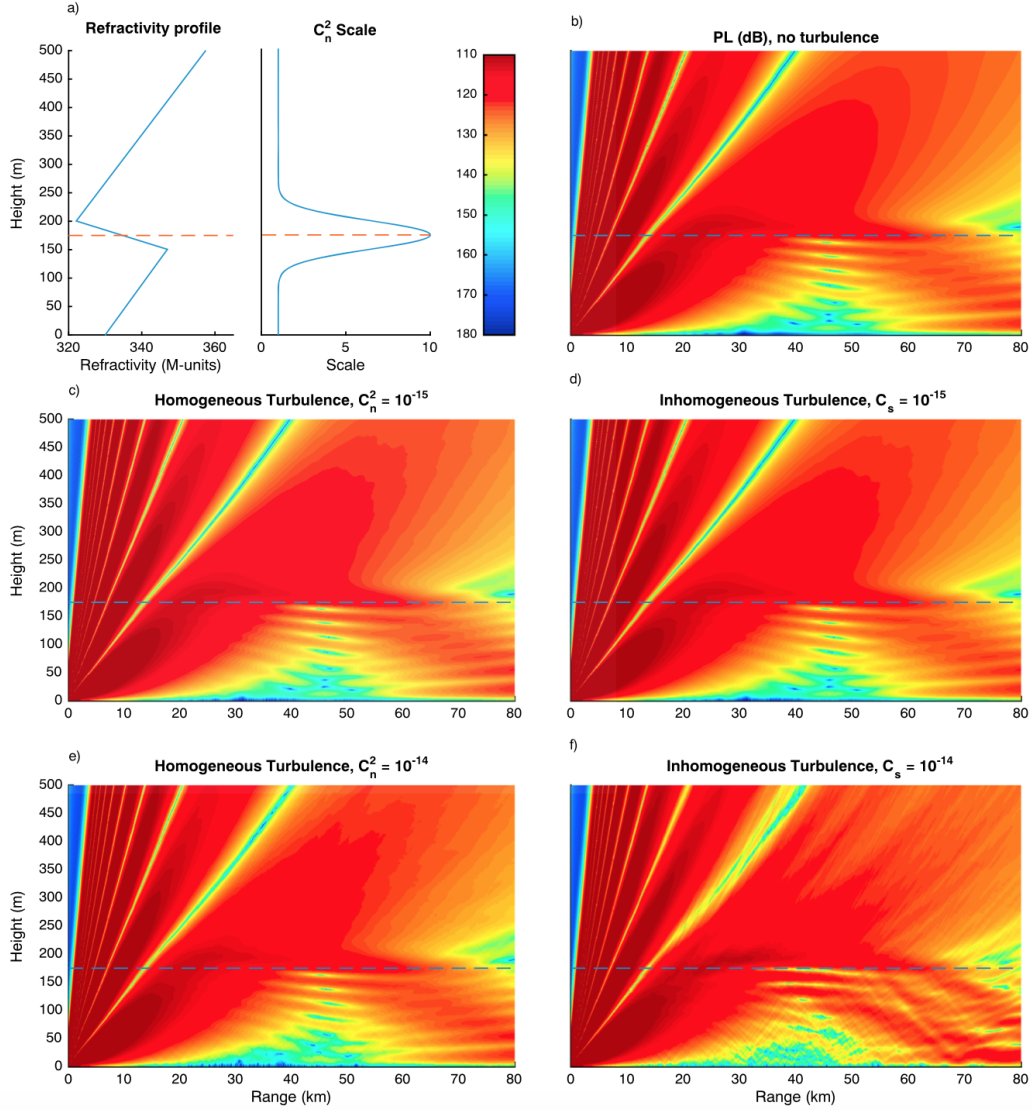
Figure 2.4: (a) Surface based duct refractivity profile and C_n^2 profile. (b) Propagation loss (PL) of 1 GHz wave given refractivity and C_n^2 profiles in (a) under no turbulence. PL calculated assuming homogeneous turbulence given in (c) $C_n^2 = 10^{-15}$ and (e) 10^{-14}. PL calculated assuming inhomogeneous turbulence given in (d) $C_s = 10^{-15}$, and (f) 10^{-14}.

24
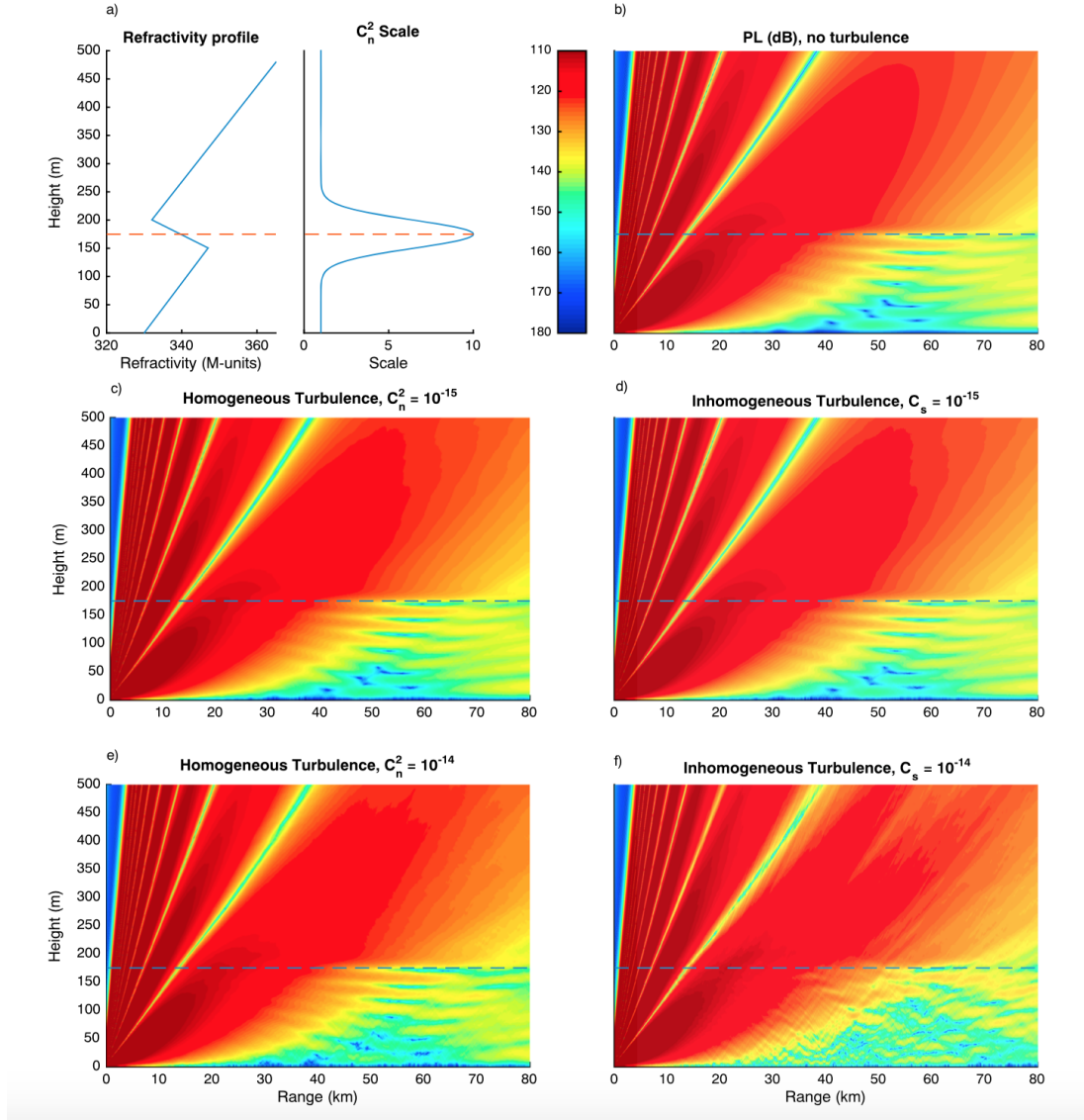
Figure 2.5: (a) Elevated duct refractivity profile and C_n^2 profile. (b) Propagation loss (PL) of 1 GHz wave given refractivity and C_n^2 profiles in (a) under no turbulence. PL calculated assuming homogeneous turbulence given in (c)$C_n^2 = 10^{-15}$ and (e) 10^{-14}. PL calculated assuming inhomogeneous turbulence given in (d) $C_s = 10^{-15}$ and (f) 10^{-14}.

parabolic equation [13]

$$\frac{\partial U(x,z)}{\partial x} = \left[\frac{jk_0}{2}(n^2 - 1) + \frac{j}{2k_0}\frac{\partial^2}{\partial z^2} \right] U(x,z) \tag{2.13}$$

$$= \left[\frac{jk_0}{2}\left(\langle n(z) \rangle^2 + \tilde{n}(x,z)^2 - 1 \right) + \frac{j}{2k_0}\frac{\partial^2}{\partial z^2} \right] U(x,z) \tag{2.14}$$

$$= [A(x,z) + B(z)]U(x,z) \tag{2.15}$$

$$A(x,z) = \frac{jk_0}{2}\left[\langle n(z)^2 \rangle + \tilde{n}(x,z)^2 - 1 \right]; \quad B(z) = \frac{j}{2k_0}\frac{\partial^2}{\partial z^2} \tag{2.16}$$

where $k_0 = \omega/c$ is a reference wave number and $j = \sqrt{-1}$. The solution to (2.16) can be written
as

$$U(x + \delta x, z) = U(x,z)\exp\left[\int_x^{x+\delta x}(A + B)\mathrm{d}x \right] \tag{2.17}$$

$$\approx U(x,z)\exp\left[(A + B)\delta x \right] \tag{2.18}$$

$$\approx U(x,z)\exp\left[A\delta x \right]\exp\left[B\delta x \right]. \tag{2.19}$$

Equation (2.18) assumes A varies slowly with range, while equation (2.19) assumes A and
B commute; however, A and B only commute for n constant in z. Error introduced by the
assumptions of equations (2.18) and (2.19)is discussed in section 2.3.2. The split performed in
equation (2.19) is the basis of the split step PE method.

The stochastic forward model is an augmented version of the PE forward model denoted
as $F(\mathbf{m}, C_n^2)$, where $\mathbf{m}$ is the refractivity profile parameter vector and C_n^2 is the structure function
constant of the observed turbulence which corresponds to the magnitude of $\tilde{n}(z)$. Specification of
C_n^2 allows control of the variance of $\tilde{n}(z)$ which is generated inside the model and added to $\langle n(z) \rangle$.

2.3.1 Parabolic Equations and Simulating Turbulence

The numeric solution to the split step PE method defined in equation (2.19) is written as

$$U(x+\delta x, z) = \frac{1}{2\pi}\exp[j\kappa\phi(z)]\mathrm{F}^{-1}\left[e^{\mathrm{WAPE}}\mathrm{F}\left[U(x,z)\right]\right] \tag{2.20}$$

where $\mathrm{F}[\cdot]$ represents the Fourier transform (FT), κ is the wave number, WAPE is the standard wide angle PE propagator, and $\exp[j\kappa\phi(z)]$ is known as the transmittance function. The PE method is summarized as follows [13]: a Fourier transform of the starting field propagating in the x direction is taken with respect to z and multiplied by a propagation filter. The inverse transform is then taken and multiplied by a transmittance function which accounts for the change in phase between range x and $x+\delta x$. The PE algorithm marches down the x axis, calculating each successive field amplitude using the previous field amplitude as input. The transmittance function $\phi(z)$ comes from the $e^{A\delta x}$ term in equation (2.19) and is defined as

$$\phi(z) = \frac{1}{2}\int_{x}^{x+\delta x}\left[\langle n(x,z)\rangle^2 + \tilde{n}(x,z)^2 - 1\right]\mathrm{d}x + z\delta x/a_e, \tag{2.21}$$

where a_e is the Earth radius in kilometers and the term $z\delta x/a_e$ has been added to correct for the curvature of the Earth. Knowing the ratio $\tilde{n}/\langle n\rangle \ll 1$ and neglecting second-order terms, we simplify the integral (2.21) so that only fluctuations over δx are nontrivial

$$\phi(z) = \left[\langle n(z)\rangle^2 - 1 + z/a_e\right]\delta x + \tilde{\phi}(z) \tag{2.22}$$

$$\tilde{\phi}(z) = \int_{x}^{x+\delta x}\tilde{n}(x',z)^2\mathrm{d}x' \tag{2.23}$$

where $\tilde{\phi}(z)$ is the randomly fluctuating part of the transmittance function. The transmittance function represents total phase change of the wave over range step δx, so to generate accurate realizations of PL using the PE method, we must know the spectrum of fluctuations integrated

over a distance δx, generate realizations of this spectrum using (2.9), and add them to the transmittance function at every range step. This spectrum is known as the *transverse spectrum*. The transverse spectrum is obtained from the spectrum of refractivity (2.8) through integration of the corresponding autocorrelation function over range (assuming $\delta x > L_0$) [21].

$$S_t(\kappa_z) \approx \frac{0.033(2\pi)^2}{\left(\kappa_z^2 + L_0^{-2}\right)^{4/3}} \delta x C_n^2 \pi^{1/2} \frac{\Gamma(4/3)}{\Gamma(11/6)} \ . \tag{2.24}$$

Note that this paper assumes the existence of a universal statistical description of small-scale turbulence which may not actually exist [26], [27]. If later research leads to a more accurate method of modeling realizations of turbulence, it may be substituted into this work without changing the inversion algorithm. For notational simplicity we will continue to denote fluctuations in refractivity generated from the transverse spectrum in (2.24) as $\tilde{n}(z)$. We simplify our algorithm by generating independent realizations of $\tilde{n}(z)$ at each range step of the PE, an assumption that will be explored in the next section.

2.3.2 Sources of Error in the PE

Here the sources of error in the forward model $F(\mathbf{m}, C_n^2)$ are explored. As mentioned in the previous section, there are several approximations made by the PE method and its modification for the inclusion of turbulence. Our goal is to identify each source of error and quantify their magnitudes. The sources of error include limitations in range and height step size by the turbulence model, approximations made in the derivation of the PE method, error in the turbulence model, and effects of polarization which are not considered by the model.

Height and Range Resolution

To generate independent realizations of refractivity fluctuations in height between ranges x and $x + \delta x$, we have assumed that the range step δx is large enough that fluctuations between

28

range steps are independent. The integral length scale introduced in section 2.2.2 is the integral of the longitudinal correlation between two points distance r apart.

$$L_0 = \int_0^\infty R(r)\mathrm{d}r \tag{2.25}$$

where $R(r)$ is the autocorrelation function of refractivity as a function of distance r between the points. Equation (2.25) reveals that the integral length scale is a measure of the minimum distance between uncorrelated points; therefore, so long as $L_0 < \delta x$, simulated turbulence will be independent between realizations of $\tilde{n}(z)$ at range steps δx apart. Recall the model spectrum in equation (2.8) uses L_0 as a parameter. Here $L_0 = 10$ m was used. This value was also used in a similar study on turbulence modeling [28]. Experimental measurements of the integral length scales of wind velocity and temperature find values between 2 and 20 m [29]. We have assumed that the integral length scale of refractivity is similar to that of wind velocity and temperature, a reasonable assumption considering refractivity is a function of temperature.

The range step size of our forward model is primarily a function of signal frequency f_c [4]

$$\delta x = \frac{\pi c}{f_c \sin^2(\theta_{\max})} \tag{2.26}$$

where c is the speed of light in a vacuum and $\theta_{\max}$ is the maximum propagation angle of the propagating wave and has been set to $7.45°$ for all inversions to emulate a directional antenna. According to (2.26), EM wave frequencies that result in range steps larger than the integral length scale are acceptable. Plugging $L_0 = 10$ m and $\theta_{\max} = 7.45°$ into equation (2.26) we get a maximum acceptable simulated wave frequency of $f_c = 5.61$ GHz.

Now we turn to the height step size, which we will denote as δz. The maximum height step is $\delta z = L_0$ because for larger step sizes fluctuations in turbulence are uncorrelated, defeating the purpose of modeling turbulence from a spectrum. The minimum height step is $\delta z = l_0$ because the von Karman spectrum is not accurate for wave numbers larger than l_0^{-1}. The value of δz in

29

the PE model is selected according to

$$\delta z = \frac{c}{2 f_c \sin(\theta_{\max})} \tag{2.27}$$

Once calculated, the value of δz is rounded down such that the number of height steps between the ocean surface and the maximum simulated height is a power of 2. The maximum height is an input to the forward model; each inversion in this paper uses max height equal to 1 km and results in 1024 evenly spaced height steps between 0 and 1000 m. Experimental values of l_0 are on the scale of 10^{-3} to 10^{-2} m.

Note that a model spectrum typically used to describe turbulence in wind velocity is being used to model that of refractivity. This may be a source of error because refractivity is a function of T, P, and e, (see equation (2.3)) all of which have some relation to wind velocity but are not identical. A wind velocity model spectrum is used because wind velocity is an area of significantly more focus in the literature than T, P, and e.

Error From Assumptions in the PE Method

Two assumptions are made in the Parabolic equation, equations (2.17)–(2.19). The first assumption is that the refractivity profile varies slowly in range, and the second assumption is that terms A and B commute. While our model assumes range independence of the refractivity profile, stochastic variations from $\tilde{n}$ cause changes in refractivity between range steps. Additionally, A and B do not commute because B is a differential operator and n is expected to change in z. An evaluation of the error caused by ignoring the commutator term on a range dependent PE is performed in [2], where it is found that

$$E = \delta x \left[jk_0 n \frac{\partial \tilde{n}}{\partial x} U(x,z) + n \frac{\partial n}{\partial z} \frac{\partial U}{\partial z} + \frac{nU}{2} \frac{\partial^2 n}{\partial z^2} + \frac{U}{2} \left(\frac{\partial n}{\partial z} \right)^2 \right] + O\left[(\delta x)^2 \right] \tag{2.28}$$

which depends on range step δx, wave frequency, and refractive index gradient in both x and z directions and is guaranteed to increase on the order of δx^2. Simulations performed here use range step sizes on the order of 100 m, at 1 GHz, so the commutator error may become a significant source of error at this range. It is possible to reduce this error by using an alternate splitting of the PE, which may be implemented in future work.

Errors in the Turbulence Model

The proposed forward model, $F(\mathbf{m}, C_n^2)$ handles turbulence and refractivity separately, by inserting randomly generated fluctuations described by C_n^2 to an environment with an independent refractivity profile parameterized by $\mathbf{m}$. However, there is some evidence of a connection between C_n^2 and $\mathbf{m}$, especially in an inversion layer, through the dissipation rate of turbulence [30]. Turbulence is a dissipative mechanism for kinetic energy cascading from large to small scales. The input for this energy is primarily wind shear, which can influence the temperature gradient in the z direction, and by proxy the refractivity gradient within a duct. Thus, the simplified model used here does not fully reflect the interactions between turbulence and refractivity, which may be a future focus.

Error From Polarization

The PE method is a forward-scatter approximation to the Helmholtz wave equation for either the electric field of a horizontally polarized wave or the magnetic field of a vertically polarized wave [13]. Wave polarization impacts the solution of the PE at the boundaries, here between ocean and air. Our PE forward model solves only for the electric field associated with a horizontally polarized wave and assumes a Dirichlet boundary condition on the ocean surface [31].This implies the ocean is a perfectly conducting surface. Because a rough ocean will not perfectly reflect all energy, it might be better modeled with a nonzero impedance [31], [32].

2.4 Bayesian Inversion

We now infer $\langle n(z) \rangle$ given PL measurement vector $\mathbf{d}$ under a Bayesian framework. The unknown variables are the entries of the $\mathbf{m}$ vector, with unknown posterior probability distribution (pdf). The joint pdf of $\mathbf{m}$ is the probability of $\mathbf{m}$ given the N_d dimensional data $\mathbf{d}$, $p(\mathbf{m}|\mathbf{d})$ is known as the posterior pdf. The $\mathbf{m}$ with the highest probability is the maximum a posteriori (MAP) solution. Using Bayes rule, we obtain the posterior pdf

$$p(\mathbf{m}|\mathbf{d}) = \frac{p(\mathbf{d}|\mathbf{m})p(\mathbf{m})}{p(\mathbf{d})} \tag{2.29}$$

It is clear from (2.29) that the posterior pdf depends on three terms, $p(\mathbf{d}|\mathbf{m}), p(\mathbf{m})$, and $p(\mathbf{d})$. Our goal is to find an expression for each distribution.

Though knowledge of the prior on $\mathbf{m}$ may be attainable, we assume that it has a uniform distribution. If some knowledge of the refractivity profile later becomes available through measurement or some statistical means, it can be utilized by this framework. The distribution $p(\mathbf{d})$ is known as the evidence and is given as

$$p(\mathbf{d}) = \int_m p(\mathbf{d}|\mathbf{m})p(\mathbf{m})d\mathbf{m} \ . \tag{2.30}$$

The evidence is not of importance here. The term reduces to a constant, serving as a normalization factor to ensure $p(\mathbf{m}|\mathbf{d})$ integrates to unity. Neglecting the evidence gives

$$p(\mathbf{m}|\mathbf{d}) \propto p(\mathbf{d}|\mathbf{m})p(\mathbf{m}) \ , \tag{2.31}$$

where $p(\mathbf{d}|\mathbf{m})$ is the likelihood function.

2.4.1 Likelihood Function

To create a likelihood function, we model the measurement vector $\mathbf{d}$ as

$$\mathbf{d} = g_K(\mathbf{m}) + n \tag{2.32}$$

where n is a noise vector of measurement and model error and $g_K(\mathbf{m})$ is the average of K realizations of $F(\mathbf{m}, C_n^2)$ to reduce stochastic fluctuations in the forward model

$$g_K(\mathbf{m}) = \frac{1}{K} \sum_{k=1}^{K} F(\mathbf{m}, C_n^2)_k . \tag{2.33}$$

We model $\mathbf{n}$ as a Gaussian noise vector

$$n \in N(0, \Sigma_d) \tag{2.34}$$

where Σ_d is the true covariance matrix of $\mathbf{d}$ which we approximate with $\mathbf{C}_d$ the maximum likelihood estimate of K runs of $\mathbf{f}(\mathbf{m}, C_n^2)$.

Because n is Gaussian, we use the standard zero mean Gaussian likelihood function to measure the likelihood of $\mathbf{d}$ coming from refractivity profile $\mathbf{m}$.

$$p(\mathbf{d} \mid \mathbf{m}) = \frac{1}{\sqrt{(2\pi)^{N_d} |\mathbf{C}_d|}} \exp\left(-\frac{(\mathbf{d} - g_K(\mathbf{m}))^T \mathbf{C}_d^{-1} (\mathbf{d} - g_K(\mathbf{m}))}{2} \right), \tag{2.35}$$

where N_d is the length of $\mathbf{d}$. Note that $\mathbf{C}_d$ might be singular because of computer precision errors caused by extremely small variance at short ranges. Adding a small diagonal load is recommended to prevent computation errors. Because the likelihood function is strictly monotonic and the terms outside the exponential do not contain input $\mathbf{d}$, we simplify equation (2.35) to an objective function

$$\phi = (\mathbf{d} - g_K(\mathbf{m}))^T \mathbf{C}_d^{-1} (\mathbf{d} - g_K(\mathbf{m})), \tag{2.36}$$
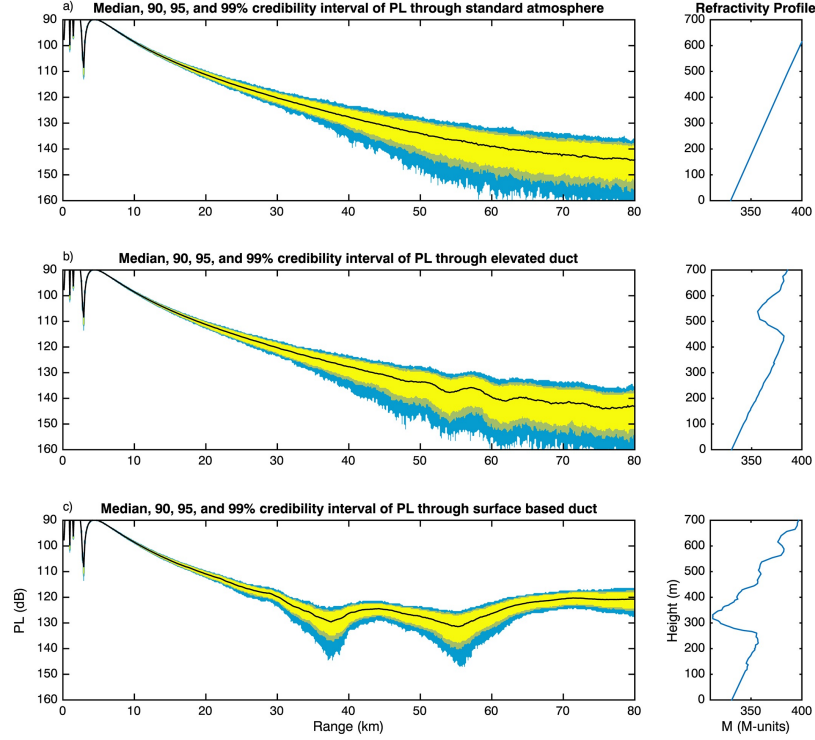
Figure 2.6: Median and 90, 95, and 99% credibility interval of propagation loss (PL) for 300 MHz wave propagating through a) standard atmosphere, b) elevated duct, c) surface based duct with $C_n^2 = 10^{-14}$. Generated from $N = 500$ Monte Carlo trials assuming homogeneous turbulence.

which must be minimized.

2.4.2 Genetic Algorithm

From (2.36) we have an objective function for evaluating the MAP estimate of **m**. To uncover the MAP estimate $\hat{\mathbf{m}}$, we run a genetic algorithm (GA) over the continuous space of possible **m**, choosing realistic upper and lower bounds on the parameters of the M-profile. The crossover rate of the GA was set to 0.9 for all inversions, though the parameters of the GA may be adjusted to assure more or less accurate results at the cost of computation time. A plot of GA convergence per forward model run for various population sizes is shown in Figure 2.7 computed using identical observation vectors **d**. Note that our convergence plot is evaluating the objective function in equation (2.36). Each line in Figure 2.7 represents the average of five inversion runs
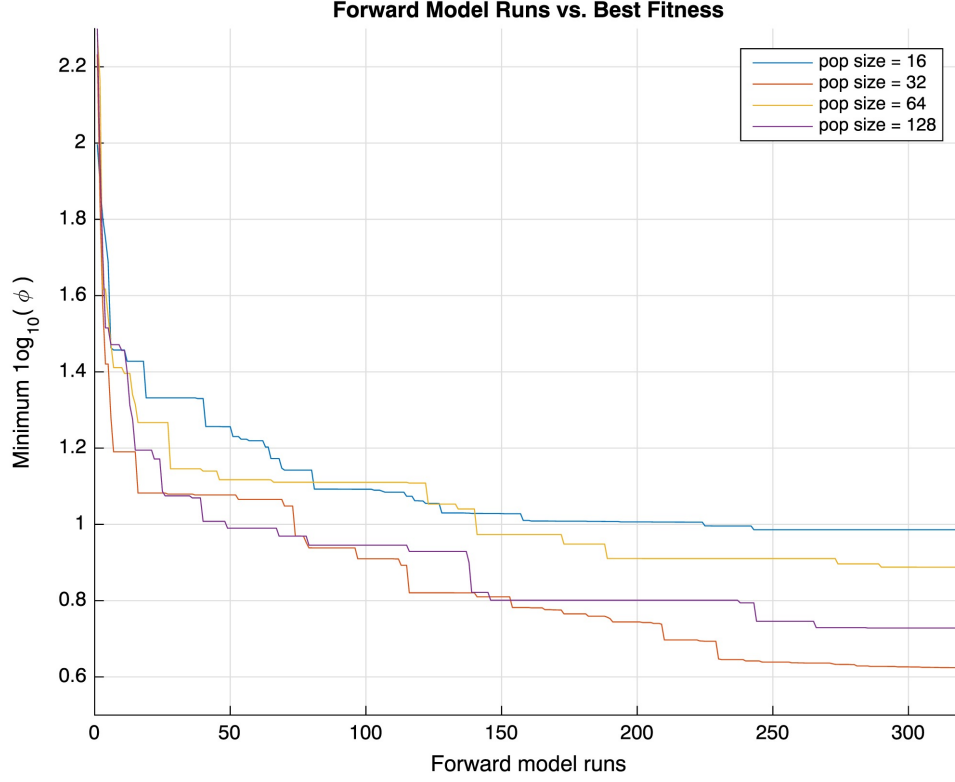
Figure 2.7: Average convergence of GA with population sizes [16, 32, 64, 128] for measurement **d** taken from elevated duct refractivity environment with $C_n^2 = 10^{-15}$

to account for randomness. It appears that a population size of 32 has the best convergence properties. All inversions performed in this paper were performed with a population size of 32 over 10 generations.

2.4.3 The "No-Duct" Case

In practice it is often the case that no duct is present in the refractivity profile being evaluated; however, this scenario is represented by only a few of the possible **m** vectors. Given the parameterized M-profile in section 2.2.1, a standard atmosphere case where no duct is present is described only when m_1, m_4, and m_5 are zero, and $m_2 \approx .113$ M-units. Given this circumstance, use of a GA becomes problematic for two reasons. First, the GA is designed to sample sparsely over the search space and navigate to a maximum point stochastically. If the no duct case is not

sampled by the algorithm (which is likely), it will lead to misidentification of a no duct event as a ducting event almost certainly. Next, in the scenario where the no duct $\mathbf{m}$ is evaluated, another $\mathbf{m}$ can be scored as slightly more likely than the no duct case due to measurement noise.

Introduction of a prior probability on the space of $\mathbf{m}$ vectors is needed to remedy the shortcomings of the optimization. Use of a prior requires slight modifications in (2.31) to account for the prior probability of no duct.

Using a uniform prior over the set of all ducting events and a corresponding prior for the no duct case is a simple method that may be used with good success. The set of $\mathbf{m}$ vectors, $\mathbf{M}_{nd}$, which denote no duct are described by $\mathbf{m} \in [0, .13, m_3, 0, 0]$. All other $\mathbf{m}$ vectors denote some type of duct. Using this knowledge we have

$$p(\mathbf{m} \mid \mathbf{d}) \propto p(\mathbf{d} \mid \mathbf{m})p(\text{duct}), \quad \mathbf{m} \in \mathbf{M}_{nd} \tag{2.37}$$

$$p(\mathbf{m} \mid \mathbf{d}) \propto p(\mathbf{d} \mid \mathbf{m})p(\text{no duct}), \quad \mathbf{m} \notin \mathbf{M}_{nd} . \tag{2.38}$$

The probability of the no duct case should reasonably reflect the frequency of ducting phenomenon in the region where $\mathbf{d}$ was measured and can be obtained from a climatology database [8] or from a numerical weather prediction algorithm[33]. To avoid problems incurred when the genetic algorithm does not evaluate the probability of a no duct scenario, the likelihood of the no duct $\mathbf{m}$ vector should be evaluated prior to running the algorithm and compared to the results.

2.4.4 Inversion Algorithm

The inversion algorithm is explained in detail below:

1. Measure both $\mathbf{d}$ and average C_n^2.

2. Evaluate equation (2.38) using $\mathbf{d}$, and $\mathbf{C}_d$, $g_K(\mathbf{m})$ simulated with any $\mathbf{m} \in \mathbf{M}_{nd}$. The resulting probability is the probability of a no duct scenario.

3. Make an initial guess $\mathbf{m}_0$. Generate the corresponding $\mathbf{C}_{d_0}$ using N Monte Carlo trials of $F(\mathbf{m}_0, C_n^2)$.

4. Run the GA. The output is $\mathbf{m}_1$.

5. Generate $\mathbf{C}_{d_1}$, rerun the GA using $\mathbf{C}_{d_1}$.

6. Repeat N times

7. Evaluate (2.37) with input $\hat{\mathbf{m}}$ and (2.38) using $\mathbf{m} \in \mathbf{M}_{nd}$. The $\mathbf{m}$ with greatest probability parameterizes the estimated refractivity.

Step 2 is evaluating the probability of no duct and can be discarded if there is no prior information about the environment being simulated. Step 3 asks for a user input, $\mathbf{m}_0$, which is used as an initial guess at the duct being estimated. If nothing is known about the duct, then the user may as well use the standard atmosphere profile from the previous step. This item is important because calculation of the covariance $\mathbf{C}_d$ is the most computationally expensive part of the algorithm. Precalculation of $\mathbf{C}_d$ speeds the inversion up considerably but requires that the algorithm is iterative. Steps 4 through 6 are the main algorithm. An optimal solution is found by the GA using the suboptimal $\mathbf{C}_d$ from the initial guess, the GA outputs the highest fitness solution $\mathbf{m}_{opt}$ and calculates the corresponding $\mathbf{C}_{d_{opt}}$. The process then repeats until the algorithm has run a set number of times. The final step compares the likelihood of the solution $\hat{\mathbf{m}}$ with the probability of the standard atmosphere (taking into account the prior likelihood of a standard atmosphere).

2.5   Inversion Results

Figure 2.8 shows the 90, 95, and 99% credibility intervals of the pdf of PL through standard atmosphere, elevated duct, and surface- based duct refractivity profiles estimated from
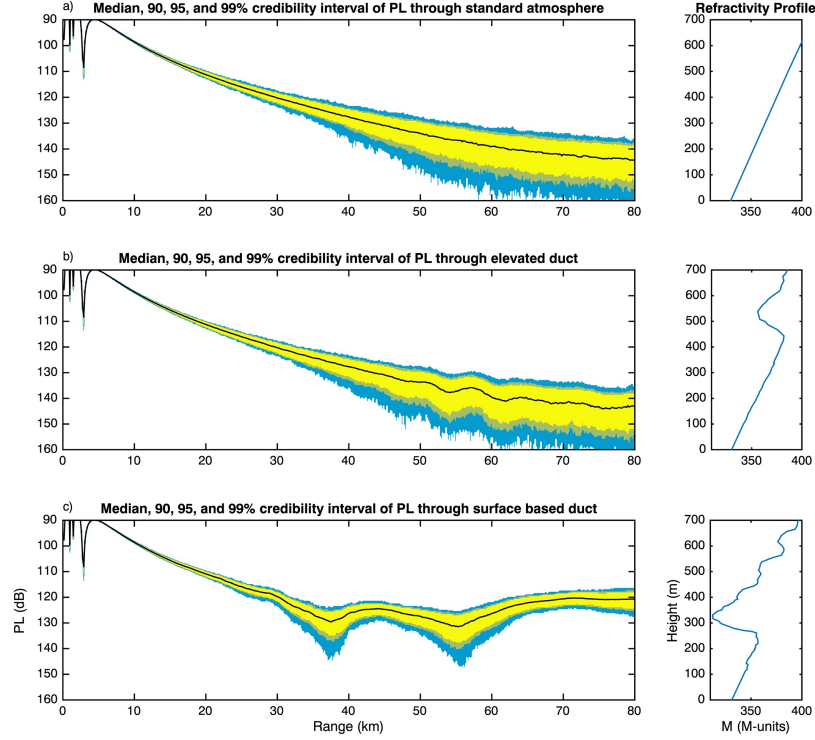
Figure 2.8: Median and 90, 95, and 99% credibility interval of propagation loss (PL) for 300 MHz wave at 20 m propagating through (a) standard atmosphere, (b) elevated duct, and (c) surface-based duct with structure function constant $C_n^2 = 10^{-14}$. Generated from 500 Monte Carlo trials assuming homogeneous turbulence.

500 Monte Carlo trials under homogeneous turbulence generated by (2.9) and (2.10) and spectrum described by (2.24) . From Figure 2.8 we see that when simulating homogeneous turbulence, the distribution of PL through standard atmosphere and elevated duct refractivity profiles is nearly identical, while surface-based ducts alter the distribution of PL significantly. Accordingly, we expect our inversion algorithm should estimate surface-based ducting profiles well but be unable to distinguish elevated ducts from standard atmosphere refractivity profiles.

Figure 2.9 shows the same distributions generated with $C_n^2(z)$ described by (2.12) with $K = 9$. For the elevated duct profile we estimated $m_3 = 443$ m, $m_4 = 95$ m and for the surface-based duct $m_3 = 260$ m, $m_4 = 70$ m. $C_n^2(z)$ remains unchanged for the standard atmosphere profile because there is no inversion layer where turbulence is expected to increase. Under this scheme both elevated and surface-based ducts produce unique distributions and therefore should
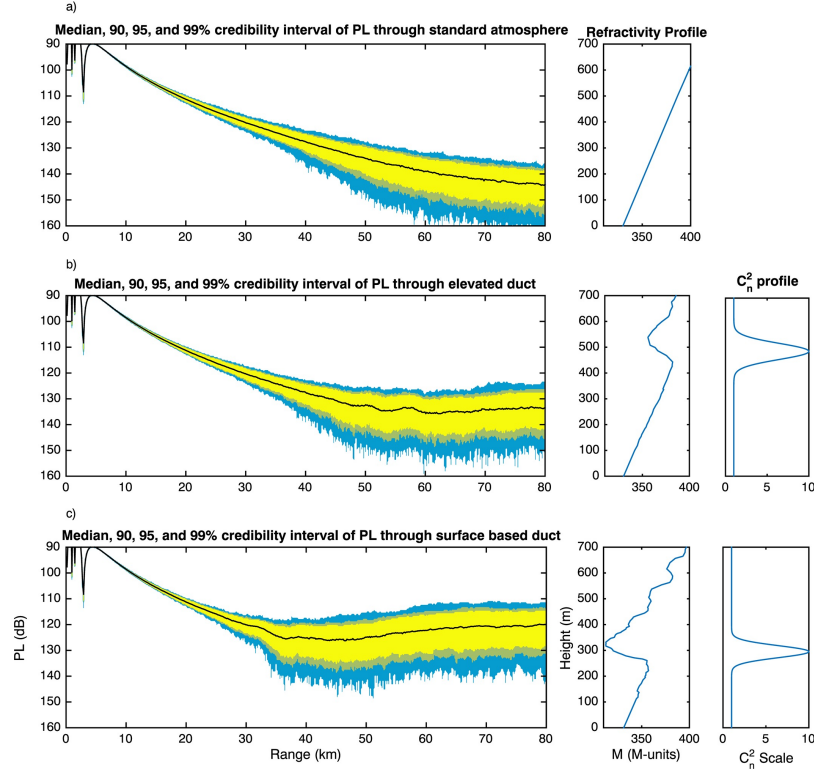
Figure 2.9: Median and 90, 95, and 99% credibility interval of propagation loss (PL) for 300 MHz wave at 20 m propagating through (a) standard atmosphere, (b) elevated duct, and (c) surface-based duct with structure function constant $C_n^2 = 10^{-14}$. Generated from 500 Monte Carlo trials assuming inhomogeneous turbulence.

allow for inversion. A key observation from Figures 2.8b and 2.9b is how the height-dependent C_n^2, when modeled as having an increase at the inversion (section 2.2.3), impacts beyond-line-of-sight (BLOS) propagation for the elevated duct case considered. In Figure 2.8b the median propagation loss over the region from 60 to 80 km is 142 dB over 500 realizations. In Figure 2.9b (height-dependent), the value is 135 dB. This suggests that failing to account for the C_n^2 increase at the inversion can negatively bias propagation estimates in the BLOS region. Note that this is consistent with the differences between with and without height dependence show in Figure 2.5. Figure 2.10 shows the covariance matrix, $\mathbf{C}_d$, of PL of a wave propagating through a surface-based duct under both homogeneous and inhomogeneous turbulence. The covariance matrices were sampled from 500 runs of the forward model using the true refractive environment. Information

conveyed in these covariance matrices is absent from the inversion algorithm when assuming $\mathbf{C}_d = \alpha\mathbf{I}$. The parameters of the forward model for the refractivity inversion were chosen such that the propagating wave would be trapped between any existing ducts and the ocean surface. If the wave was to propagate at too steep an angle, it would not be trapped in the duct and we might as well be working with a standard atmosphere. Outside the possibility that the transmitted wave is not trapped by an existing duct, the transmitter height and propagation angle of the wave should not impact inversion accuracy because the algorithm works by evaluating the first- and second- order statistics of the specific wave being modeled. The same can be said for the height at which PL is measured.

All figures and inversions were performed using PL at constant 20 m height (from the ocean surface) from a transmitter at 10 m transmitting a 300 MHz wave over an 80 km range with vertical beam width of 0.209 radians. The transmitter was pointed horizontally such that the wave propagated normal to the line formed between the transmitter and the ocean surface. The genetic algorithm used in the inversion ran over 10 generations with a population size of 32 and a crossover fraction of 0.1. Each inversion consisted of 60 GA runs. Inversions were run comparing 60 iterations of the algorithm in section 2.4.4 and 60 inversions where $\mathbf{C}_d = \sigma^2\mathbf{I}$. The two inversion strategies are compared in Figures 2.11 and 2.12. The initial measurement vector, $\mathbf{d}$, was simulated using the forward model propagating through the true refractivity profile over an 80 km range. The simulated $\mathbf{d}$ vector was 1234 points long, with a step size of 64 m. Two refractive environments were estimated. First, a surface-based duct from the VOCAR 1993 experiment [34] with homogeneous turbulence generated by (2.9) and (2.10) and spectrum described by (2.24). Next, an elevated duct from the VOCAR 1993 experiment with inhomogeneous turbulence simulated using (2.12). An inhomogeneous turbulence model is used for inversions on the elevated duct because Figures 2.8 and 2.10 show that under a homogeneous turbulence model, the elevated duct will be nearly indistinguishable from a standard atmosphere profile.
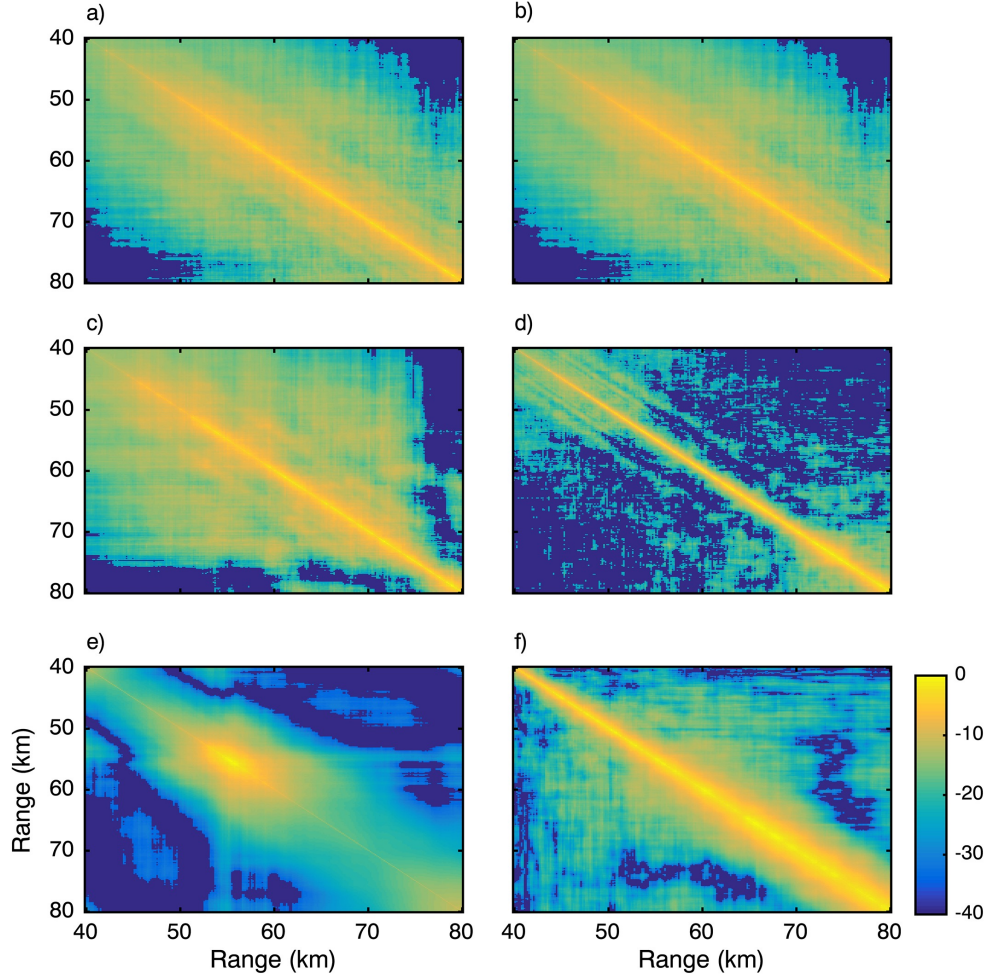
Figure 2.10: Estimated covariance matrix (in dB) of propagation loss at 20 m height through (a and b) standard atmosphere, (c and d) VOCAR elevated duct, and (e and f) VOCAR surface-based duct. Homogeneous turbulence model used in Figures 2.10a, 2.10c, and 2.10e. Inhomogeneous turbulence used in Figures 2.10b, 2.10d, and 2.10f. Estimates made using (500) forward model runs of propagation loss using $C_n^2 = 10^{-13}$.
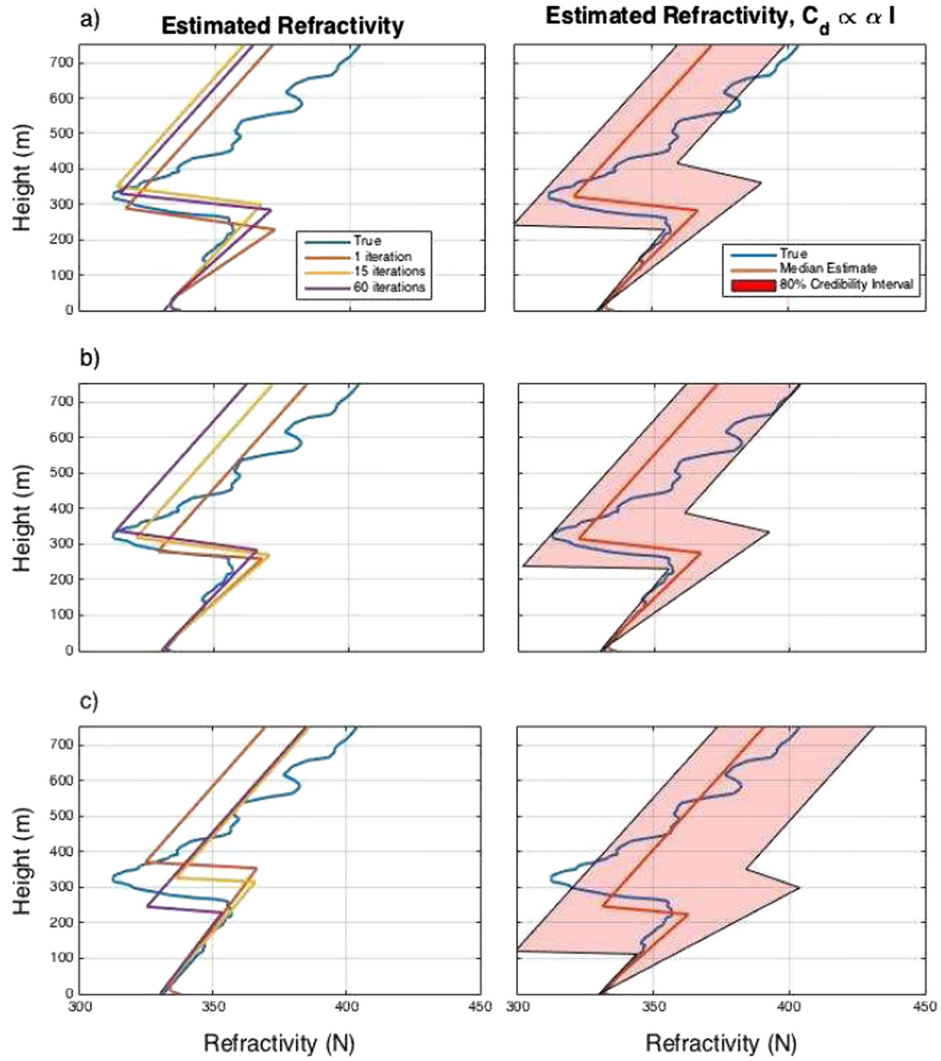
Figure 2.11: Estimated refractivity for surface-based duct measured in VOCAR 1993 experiment assuming homogeneous turbulence, (a) $C_n^2 = 10^{-17}$, (b) $C_s = 10^{-15}$, and (c) $C_s = 10^{-13}$. (left column) Inversions performed using Monte Carlo estimate of C_d (Figures 2.11a– 2.11c); (right column) C_d assumed proportional to $\alpha \mathbf{I}$.
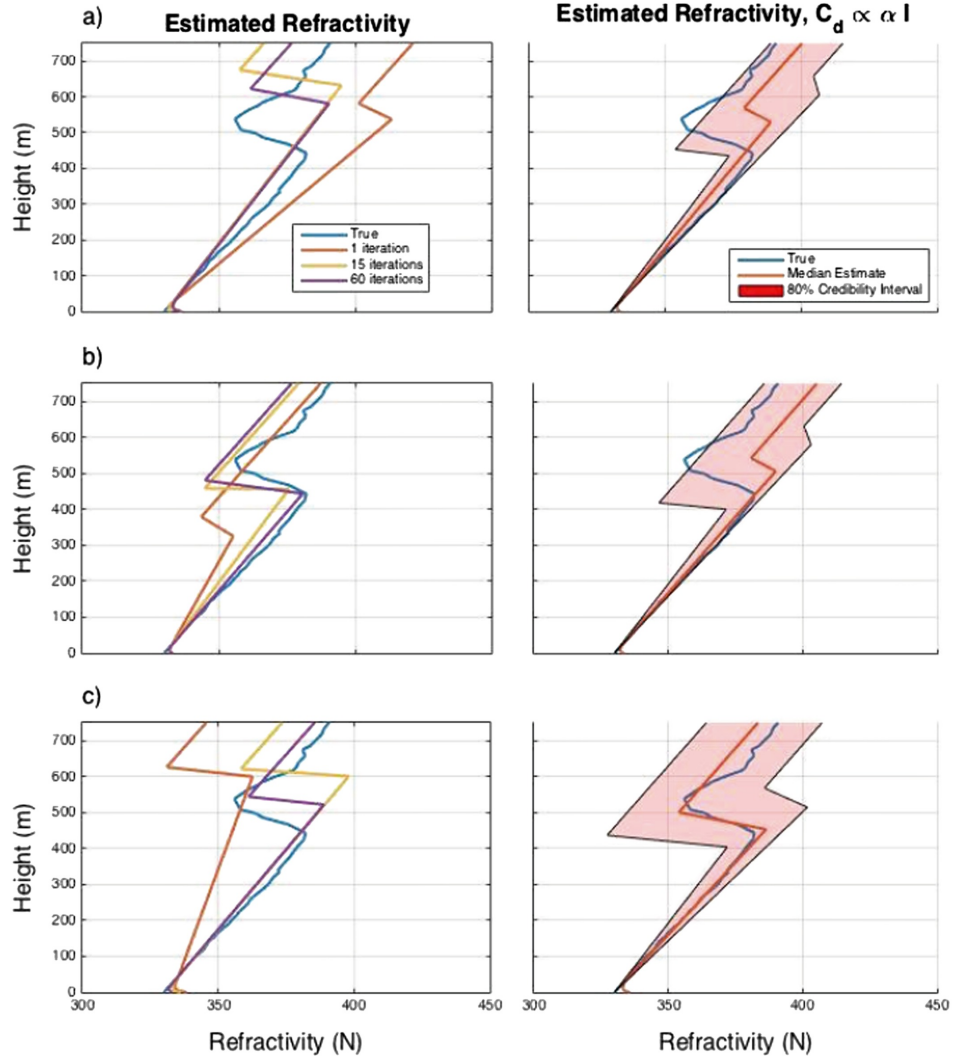
Figure 2.12: Estimated refractivity for elevated duct measured in VOCAR 1993 experiment assuming inhomogeneous turbulence, (a) $C_n^2 = 10^{-17}$, (b) $C_s = 10^{-15}$, and (c) $C_s = 10^{-13}$. (left column) Inversions performed using Monte Carlo estimate of C_d; (right column) C_d assumed proportional to $\alpha \mathbf{I}$.

Figure 2.11 has two columns. The left column shows the inversion result after 1, 15, and 60 iterations of the algorithm in sec 2.4.4. The right column shows the median and 80% credibility intervals of the estimated refractivity profiles after 60 independent inversions. Both columns show inversions performed on a surface-based duct over a range of C_n^2 values assuming homogeneous turbulence. Figure 2.11 show that the iterative algorithm hits an accurate solution after 15 iterations and does not change significantly in subsequent iterations. The Monte Carlo trials which ignore $\mathbf{C}_d$ produce an accurate median solution but have a wide credibility interval, indicating that individual solutions may not be very accurate. Both inversion methods appear to lose accuracy as C_n^2 increases. Figure 2.12 is consistent with Figure 2.11 in these regard.

2.6 Conclusions

An inversion scheme was proposed for estimation of atmospheric refractivity given measured PL $\mathbf{d}$ at constant height in presence of turbulence. The mean and covariance of error in PL measurements was estimated using Monte Carlo trials and used to evaluate a likelihood function for parameterized refractivity profiles. A genetic algorithm was then applied to search over the parameter space to find the MAP refractivity profile, which was compared in accuracy to refractivity profiles found using a likelihood function assuming spatially uncorrelated errors ($\mathbf{C}_d \propto \mathbf{I}$).

Two models of turbulence were used to simulate refractivity fluctuations, a homogeneous model where C_n^2 was constant, and a more realistic inhomogeneous model where C_n^2 reached a distinct peak at the inversion layer. Inversion results showed that the inhomogeneous turbulence profile caused elevated ducts to produce trapping below the inversion layer, an effect which is limited to surface-based ducts in nonturbulent environments. Additionally, despite the increased refractivity fluctuations introduced by the inhomogeneous turbulence, inversion under such a scheme produced accurate estimates of the parameters of an elevated duct which otherwise would

have been mistaken for a standard atmosphere profile. The results suggest that turbulence can significantly alter PL of waves traveling through atmospheric ducts by increasing the strength of existing ducts.

For inversions, use of Monte Carlo trials to estimate covariance of PL appeared to increase the accuracy of inversions performed on ducts with ambiguous mean PL patterns. Analysis of PL from standard atmosphere and elevated and surface-based duct refractivity profiles showed that homogeneous and inhomogeneous turbulence models produced different PL distributions for the same refractivity profiles. Turbulence can have a significant impact on the distribution of PL, so accuracy of refractivity inversion is limited by our ability to correctly model turbulence.

2.7   Acknowledgments

The text of Chapter Two is in full a reprint of the material as it appears in Mark Wagner, Peter Gerstoft, and Ted Rogers, "Estimating Refractivity from Propagation Loss in Turbulent Media," *Radio Science* 51.12 (2016): 1876-1894.

Bibliography

[1] N.E. Lentini and E.E. Hackett, "Global sensitivity of parabolic equation radar wave propagation simulation to sea state and atmospheric refractivity structure," *Radio Science*, vol. 50, no. 10, pp. 1027–1049, 2015.

[2] KH Craig and MF Levy, "Parabolic equation modelling of the effects of multipath and ducting on radar systems," in *IEEE Proceedings F. Radar and Signal Process*. IET, 1991, vol. 138, pp. 153–162.

[3] Marvin L Wesely, "The combined effect of temperature and humidity fluctuations on refractive index," *Journal of Applied Meteorology*, vol. 15, no. 1, pp. 43–49, 1976.

[4] Amalia E Barrios, "Modeling surface layer turbulence effects at microwave frequencies," in *Radar Conference, 2008. RADAR'08. IEEE*. IEEE, 2008, pp. 1–6.

[5] P. Gerstoft, L.T. Rogers, J.L. Krolik, and W.S. Hodgkiss, "Inversion for refractivity parameters from radar sea clutter," *Radio science*, vol. 38, no. 3, 2003.

[6] Caglar Yardim, Peter Gerstoft, and William S Hodgkiss, "Statistical maritime radar duct estimation using hybrid genetic algorithm–markov chain monte carlo method," *Radio Science*, vol. 42, no. 3, pp. 1–15, 2007.

[7] C. Yardim, P. Gerstoft, and W.S. Hodgkiss, "Estimation of radio refractivity from radar clutter using Bayesian Monte Carlo analysis," *IEEE Trans. Antennas. Prop.*, vol. 54, no. 4, pp. 1318–1327, 2006.

[8] Caglar Yardim, Peter Gerstoft, and William S Hodgkiss, "Sensitivity analysis and performance estimation of refractivity from clutter techniques," *Radio Science*, vol. 44, no. 1, pp. 1058–1070, 2009.

[9] A. Karimian, C. Yardim, P. Gerstoft, W.S. Hodgkiss, and A.E. Barrios, "Refractivity estimation from sea clutter: An invited review," *Radio Sci.*, vol. 46, no. 06, pp. 1–16, 2011.

[10] Rémi Douvenot, Vincent Fabbro, Peter Gerstoft, Christophe Bourlier, and Joseph Saillard, "A duct mapping method using least squares support vector machines," *Radio Science*, vol. 43, no. 6, 2008.

[11] L Ted Rogers, "Demonstration of an efficient boundary layer parameterization for unbiased propagation estimation," *Radio Science*, vol. 33, no. 6, pp. 1599–1608, 1998.

[12] Amalia E Barrios, "Parabolic equation modeling in horizontally inhomogeneous environments," *IEEE Trans. Antennas Propagat*, vol. 40, no. 7, pp. 791–797, 1992.

[13] Mireille Levy, *Parabolic equation methods for electromagnetic wave propagation*, Number 45. Institution of Engineering and Technology, 2000.

[14] D.K. Wilson, J.G. Brasseur, and K.E. Gilbert, "Acoustic scattering and the spectrum of atmospheric turbulence," *J. Acoust. Soc. Am.*, vol. 105, no. 1, pp. 30–34, 1999.

[15] J.C. Wyngaard and M.A. LeMone, "Behavior of the refractive index structure parameter in the entraining convective boundary layer," *J. Atmos. Sci.*, vol. 37, no. 7, pp. 1573–1585, 1980.

[16] Andrey Nikolaevich Kolmogorov, "The local structure of turbulence in incompressible viscous fluid for very large reynolds numbers," in *Dokl. Akad. Nauk SSSR*, 1941, vol. 30, pp. 299–303.

[17] Stephen B Pope, *Turbulent Flows*, Cambridge University Press, 2000.

[18] M Chamecki and NL Dias, "The local isotropy hypothesis and the turbulent kinetic energy dissipation rate in the atmospheric surface layer," *Quarterly Journal of the Royal Meteorological Society*, vol. 130, no. 603, pp. 2733–2752, 2004.

[19] Donald B Percival, "Simulating gaussian random processes with specified spectra," *Computing Science and Statistics*, pp. 534–534, 1993.

[20] Kenneth E Gilbert, Xiao Di, Samir Khanna, Martin J Otte, and John C Wyngaard, "Electromagnetic wave propagation through simulated atmospheric refractivity fields," *Radio Science*, vol. 34, no. 6, pp. 1413–1435, 1999.

[21] Daniel Rouseff, "Simulated microwave propagation through tropospheric turbulence," *IEEE Trans. Antennas Propagat*, vol. 40, no. 9, pp. 1076–1083, 1992.

[22] Akira Ishimaru, *Wave propagation and scattering in random media*, vol. 2, Academic press New York, 1978.

[23] Valerian Ilitch Tatarskii, "The effects of the turbulent atmosphere on wave propagation," *Jerusalem: Israel Program for Scientific Translations, 1971*, vol. 1, 1971.

[24] Peter Gerstoft, Donald F Gingras, L Ted Rogers, and William S Hodgkiss, "Estimation of radio refractivity structure using matched-field array processing," *Antennas and Propagation, IEEE Transactions on*, vol. 48, no. 3, pp. 345–356, 2000.

[25] F.D. Tappert, "The parabolic approximation method," in *Wave propagation and underwater acoustics*, pp. 224–287. Springer, 1977.

[26] Rod Frehlich and Robert Sharman, "Estimates of turbulence from numerical weather prediction model output with applications to turbulence diagnosis and data assimilation," *Monthly Weather Review*, vol. 132, no. 10, pp. 2308–2324, 2004.

[27] Vincent Fabbro and Laurent Féral, "Comparison of 2d and 3d electromagnetic approaches to predict tropospheric turbulence effects in clear sky conditions," *IEEE Transactions on Antennas and Propagation,*, vol. 60, no. 9, pp. 4398–4407, 2012.

[28] Daniel Rouseff, "Simulating radar propagation through atmospheric turbulence using the tropospheric electromagnetic parabolic equation routine (temper)," Tech. Rep., DTIC Document, 1991.

[29] YS Wang, DR Miller, DE Anderson, RM Cionco, and JD Lin, "A spatial length scale analysis of turbulent temperature and velocity fluctuations within and above an orchard canopy," *Boundary-layer meteorology*, vol. 59, no. 1-2, pp. 125–139, 1992.

[30] LJ Peltier and JC Wyngaard, "Structure–function parameters in the convective boundary layer from large-eddy simulation," *Journal of the atmospheric sciences*, vol. 52, no. 21, pp. 3641–3660, 1995.

[31] D Dockery and James R Kuttler, "An improved impedance-boundary algorithm for fourier split-step solutions of the parabolic wave equation," *IEEE Transactions on Antennas and Propagation*, vol. 44, no. 12, pp. 1592–1599, 1996.

[32] Allan P Rosenberg, "A new rough surface parabolic equation program for computing low-frequency acoustic forward scattering from the ocean surface," *The Journal of the Acoustical Society of America*, vol. 105, no. 1, pp. 144–153, 1999.

[33] A Karimian, C Yardim, T Haack, P Gerstoft, W. S. Hodgkiss, and L. T. Rogers, "Towards assimilation of atmospheric surface layer using weather prediction and radar clutter observations," *J. Appl. Meteorol.*, pp. 2345—2355., 2012.

[34] Richard Paulus et al., "Vocar: An experiment in variability of coastal atmospheric refractivity," in *Data Analysis and Interpretation*. IEEE, 1994, vol. 1, pp. 386–388.

Chapter 3

Compressive MIMO Beamforming of Data Collected in a Refractive Environment

The phenomenon of ducting is caused by abnormal atmospheric refractivity patterns, and is known to allow electromagnetic (EM) waves to propagate over the horizon with unusually low propagation loss. It is unknown what effect ducting has on multiple input multiple output (MIMO) channels, particularly its effect on multipath propagation in MIMO channels. A high accuracy angle-of-arrival (AoA) and angle-of-departure (AoD) estimation technique for MIMO communications, which we will refer to as compressive MIMO beamforming, was tested on simulated data, then applied to experimental data taken from an over the horizon (OTH) MIMO testbed located in a known ducting hotspot in southern California. The multipath channel was estimated from the receiver data recorded over a period of 18 days, and an analysis was performed on the recorded data. The goal is to observe the evolution of the MIMO multipath channel as atmospheric ducts form and dissipate to gain some understanding of the behavior of channels in a refractive environment. This work is motivated by the idea that some multipath characteristics of MIMO channels within atmospheric ducts could yield important information about the duct.

3.1 Introduction

For long range wireless electromagnetic (EM) communication signals, the line of sight path between transmitter and receiver can be obscured by the curvature of the earth. Generally signal strength at the receiver fades quickly with range for over the horizon signals, but an exception can be made for marine environments experiencing atmospheric ducting [1]. Ducting causes trapping of EM waves propagating at low angles between the ocean's surface and the top of the duct [2]. Ducts are formed by certain atmospheric refractivity profiles, where refractivity is a measure of the deviation of an electromagnetic wave from a straight line path due to variation in air density as a function of height. In a ducting environment an EM wave can be guided over the horizon through a path that it would not otherwise travel [3]. This effect is known to decrease signal attenuation over long ranges, but may also cause multipath interference in the form of multipath fading [4].

In a ducting environment it is hypothesized that communication channels may have higher throughput [5], and may also take on unique properties based on the duct. To test this hypothesis, an experimental testbed was set up where a 4x4 multiple input multiple output (MIMO) communications array was placed on vertical masts 41 km apart in a ducting hotspot in southern California [1], see figure 5.1. Pilot signals from the transmitters were recorded by the receivers at regular intervals for 18 days. The goal of the experiment was to observe the change in the multipath environment for an over the horizon channel during ducting events. Ducting events were identified by significant increases in received power levels at the receiver array.

We are unaware of any other experiment to date having been performed for the purpose of relating the multipath characteristics of a MIMO channel to atmospheric refractivity. While the over the horizon MIMO channel data that was collected is unique, it is also limited in that it is representative of one static channel which may not be representative of all ducting channels. Our hope is that a better understanding of the impact of ducting on MIMO communications channels

will lead to more effective refractivity estimation techniques. For instance if the multipath channel takes on specific properties exclusively during ducting events, this information could be used to more accurately identify the presence and properties of a duct.

In this paper we use compressive MIMO beamforming to determine the angle-of-arrival (AoA) and angle-of-departure (AoD) of signals traveling through a channel. Compressive MIMO beamforming (detailed in section 3.3.2) is a precision beamforming technique utilizing compressed sensing, and is based on the assumption of signal sparsity [6], [7] in the transmit and receive angle domain. To obtain a best estimate of the MIMO channel matrix (see section 3.2), [8], [9], a set of optimal training sequences [10] (see section 3.5) were sent from the transmitter array. From the channel matrix a virtual array [11] is formed, to which compressive MIMO beamforming can be applied to obtain the transmit and receive angles of the signal.

The structure of the paper is as follows. In section 3.2 the signal model is explained and theoretical framework for channel estimation is laid out. Optimal channel estimation is essential to this work because knowledge of the MIMO channel is required for beamforming. Section 3.3 gives the theory behind compressive sensing and lays the framework for MIMO beamforming. Section 3.4 gives compressive MIMO beamforming error rates in two metrics for simulated signals of varying signal to noise ratio (SNR) and number of active signal paths. Section 3.5 describes the experimental testbed and details regarding the transmitted waveforms and their detections. Experimental data is processed and the resulting multipath channels and channel properties are analyzed in section 3.6.

3.2   Multipath Signal Model

3.2.1   MIMO Signal Model

MIMO systems are a well studied topic in antenna communications and offer several benefits over single input and output systems. A MIMO system is defined as an antenna setup

utilizing multiple transmitters and receivers, often positioned in an array. By increasing the number of transmitters and receivers the dimension of the channel matrix, whose elements represent the transfer function between each transmitter and receiver, is increased. Higher dimensional channel matrices can be exploited by spatially multiplexing multiple streams of information [12]. Having multiple receivers allows for spatial processing (more generally known as beamforming) to estimate the receive angle of arriving signals, while multiple transmitters allows for spatial processing for estimation of the transmit angle of arriving signals.

The position of transmitters and receivers in a MIMO system is flexible, though this paper will focus on transmit and receive elements positioned in uniform linear arrays (ULA). Consider N_T transmitters and N_R receivers with element spacing r and s, communicating over a single frequency. The set of transmitters send signals $\mathbf{x}_t \in \mathbb{C}^{N_T}$ at time sample time $t = 1 \ldots T$. Each of P paths have a unique AoD ϕ_p, AoA θ_p, and corresponding complex path gain.

Assuming a time invariant channel, the received signal at time sample t, $\mathbf{y}_t \in \mathbb{C}^{N_R}$ is

$$\mathbf{y}_t = \mathbf{H}\mathbf{x}_t + \mathbf{w}_t, \tag{3.1}$$

where $\mathbf{w}_t \in \mathbb{C}^{N_R}$ is a zero mean symmetric complex Gaussian noise vector at time t and $\mathbf{H} \in \mathbb{C}^{N_R \times N_T}$ is the channel matrix which can be further decomposed [6]

$$\mathbf{H} = \sum_{p=1}^{P} a_p \mathbf{a}_R(\theta_p) \mathbf{a}_T(\phi_p)^H, \tag{3.2}$$

where a_p is the complex gain of path p, $\mathbf{a}_R(\theta) \in \mathbb{C}^{N_R}$, and $\mathbf{a}_T(\phi) \in \mathbb{C}^{N_T}$ are the receive and transmit steering vectors for angles θ and ϕ, whose ith element is defined as $\mathbf{a}_{T,i}(\theta) = \exp[-j2\pi r \sin(\theta)i/\lambda]$ for $i = [0, \ldots, N_T - 1]$ and $\mathbf{a}_{R,i}(\theta) = \exp[-j2\pi s \sin(\theta)i/\lambda]$ for $i = [0, \ldots, N_R - 1]$ with $j = \sqrt{-1}$, s and r are transmitter and receiver array spacings in meters, and λ is the carrier wavelength in meters [13]. Eq (3.2) implicitly assumes that the received signals arrive as plane waves at the receiver.

The channel described by eq (3.1) and (3.2) can be equivalently viewed as the sum of channels from every possible signal path. Rather than express the channel in (3.2) as the sum of array responses from each of P paths, it can also be expressed as the sum of array responses from every possible path over the space of possible transmit and receive angles (θ, ϕ), only a few of which will be active (take non-zero values). Formally,

$$\mathbf{H} = \int_{\phi} \int_{\theta} \mathbf{H}^a(\theta, \phi) \mathbf{a}_R(\theta) \mathbf{a}_T(\phi)^H \, d\theta \, d\phi, \tag{3.3}$$

where $\mathbf{H}^a(\theta, \phi)$ is a function representing the path gain from transmit and receive angles θ and ϕ. Since we have made the assumption that $\mathbf{H}^a(\theta, \phi)$ is non-zero at only a few points, an approximate discretization can be made

$$\mathbf{H} \approx \sum_{i}^{Q_R} \sum_{j}^{Q_T} \mathbf{H}_{i,j}^a \mathbf{a}_R(\theta_i) \mathbf{a}_T^H(\phi_j), \tag{3.4}$$

where Q_R and Q_T are the number of points to which the transmit and receive angle space are quantized. The approximation of eq (3.4) replaces the continuous function $\mathbf{H}^a(\theta, \phi)$ with sparse matrix $\mathbf{H}^a \in \mathbb{C}^{Q_R \times Q_T}$, (having exactly P non-zero entries) which we will refer to as the angular domain channel matrix [14]. Plugging (3.4) into (3.1) we have

$$\mathbf{y}_t \approx \sum_{i}^{Q_R} \sum_{j}^{Q_T} \mathbf{H}_{i,j}^a \mathbf{a}_R(\theta_i) \mathbf{a}_T^H(\phi_j) \mathbf{x}_t + \mathbf{w}_t, \tag{3.5}$$

which is an alternative signal model utilizing sparsity. The focus of this paper is the estimation of $\mathbf{H}^a$. From known $\mathbf{x}_t$ and measurements of $\mathbf{y}_t$ we estimate $\mathbf{H}$, then using sparse processing detailed in section 3.3 an estimate of $\mathbf{H}^a$ is constructed from $\mathbf{H}$. Once recovered, we analyze the transmit and receive angles traveled by multipath signals propagating through ducting environments to determine any special properties they may have which could be used to characterize ducts.

The elements of the steering vectors $\mathbf{a}_R(\theta)$ and $\mathbf{a}_T(\phi)$ are unit magnitude complex values

representing the relative phase shift of the signals arriving or departing from one antenna with respect to a reference antenna. From their definitions, the phase shift between vector elements is dependent on carrier signal wavelength, arrival/departure angle, and inter element array spacing. Ideally inter element spacing should be one half the carrier signal wavelength, which results in maximum angular resolution of $\pm 90°$ and is known as critical spacing. Sparsely spaced array elements result in angle ambiguities caused by aliasing, while densely spaced arrays have smaller array aperture leading to lower angular resolution. For sparsely spaced arrays, $\theta_{max} = \sin^{-1}(\frac{\lambda}{2r})$ where θ_{max} is the maximum resolvable receive angle, r is the inter element spacing, and λ is the wavelength of the carrier signal in meters.

3.2.2 Channel Estimation

Compressive MIMO beamforming takes the estimated channel matrix $\mathbf{H}$ as input. The estimate, $\hat{\mathbf{H}}$ (where $\hat{}$ indicates an estimate) must be made from the known transmitted and measured received signals. In this section we derive criteria for the transmitted waveform such that the resulting channel estimate is optimal. Later in section 3.5 the waveform transmitted from the experimental testbed is described and can be shown to satisfy the criteria for optimal channel estimation.

Consider a matrix $\mathbf{X} \in \mathbb{C}^{N_T \times T}$ whose columns $\mathbf{x}_t$ represent the symbols sent from all transmitters at time $t = [1, ..., T]$ and matrix $\mathbf{Y} \in \mathbb{C}^{N_R \times T}$ whose columns $\mathbf{y}_t$ contain the received symbols at time $t = [1, ..., T]$. $\mathbf{Y}$ can be expressed as

$$\mathbf{Y} = \mathbf{HX} + \mathbf{W}, \tag{3.6}$$

where $\mathbf{W} \in \mathbb{C}^{N_R \times T}$ is complex Gaussian sensor noise distributed such that each column $\mathbf{w}_t \sim \mathcal{CN}(\mathbf{0}, \sigma^2 \mathbf{I}_T)$ for $t = [1, \ldots, T]$, where $\mathbf{I}_T$ is the identity matrix of dimension T. In this case the least squares (LS) channel estimator is [9]

$$\hat{\mathbf{H}} = \mathbf{Y}\mathbf{X}^{\dagger}, \tag{3.7}$$

where $\mathbf{X}^{\dagger} = \mathbf{X}^H(\mathbf{X}\mathbf{X}^H)^{-1}$ is the pseudoinverse. Training matrix $\mathbf{X}$ is constrained by the transmitted power as

$$\|\mathbf{X}\|_F^2 = \text{tr}(\mathbf{X}\mathbf{X}^H) = \mathcal{P}, \tag{3.8}$$

where $\text{tr}[.]$ is the trace operation and $\mathcal{P}$ is a known constant representing the total power transmitted and $\|.\|_F$ is the Frobenius norm. We wish to find a training matrix $\mathbf{X}$ which minimizes the channel estimation error subject to the power constraint (3.8). This is equivalent to solving the optimization problem

$$\min_{\mathbf{X}} \text{E}\left[\|\mathbf{H} - \hat{\mathbf{H}}\|_F^2\right] \qquad \text{s.t.} \quad \text{tr}(\mathbf{X}\mathbf{X}^H) = \mathcal{P}, \tag{3.9}$$

where $\text{E}[.]$ is the expected value. Combining (3.6) and (3.7) we see $\mathbf{H} - \hat{\mathbf{H}} = \mathbf{W}\mathbf{X}^{\dagger}$. Continuing from (3.9) we get the objective function

$$\begin{aligned} J &= \text{E}\left[\|\mathbf{H} - \hat{\mathbf{H}}\|_F^2\right] \\ &= \text{E}\left[\|\mathbf{W}\mathbf{X}^{\dagger}\|_F^2\right] \\ &= \sigma_n^2 N_R \text{tr}\left[\mathbf{X}^{\dagger H}\mathbf{X}^{\dagger}\right] \\ &= \sigma_n^2 N_R \text{tr}\left[(\mathbf{X}\mathbf{X}^H)^{-1}\right], \end{aligned} \tag{3.10}$$

where $\text{E}[\mathbf{W}^H\mathbf{W}] = \sigma_n^2 N_R \mathbf{I}$. Plugging (3.10) into (3.9), an equivalent equation is

$$\min_{\mathbf{X}} \text{tr}\left[(\mathbf{X}\mathbf{X}^H)^{-1}\right] \quad \text{s.t.} \quad \text{tr}\left[\mathbf{X}\mathbf{X}^H\right] = \mathcal{P}, \tag{3.11}$$

From here any training matrix satisfying
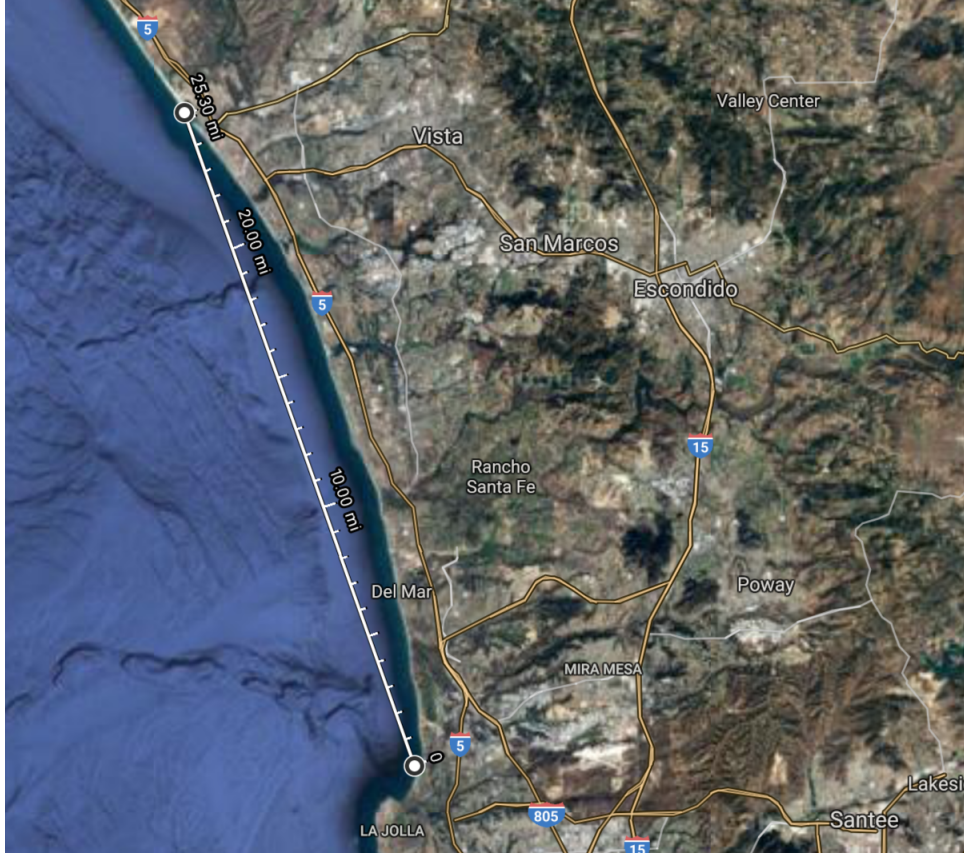
Figure 3.1: Shortest path between transmitter (bottom) and receiver (top) superimposed on satellite image of Southern California.

$$\mathbf{X}\mathbf{X}^H = \frac{\mathcal{P}}{N_T}\mathbf{I}, \tag{3.12}$$

is optimal for (3.11), [9]. The optimality criteria also simplifies the channel estimation equation. Plugging (3.12) into (3.7) we have

$$\hat{\mathbf{H}} = \left(\frac{N_T}{\mathcal{P}}\right)\mathbf{Y}\mathbf{X}^H. \tag{3.13}$$

All matrices with orthogonal rows with the same norm satisfy the optimality criteria of eq (3.12). The waveforms transmitted by the MIMO testbed described in section 3.5 satisfy (3.12).

3.3 Compressive MIMO Beamforming

3.3.1 Review of Compressive Sensing

Compressive Sensing (CS) is a relatively new field of signal processing wherein a measurement vector is reconstructed as a sparse linear combination of predetermined dictionary vectors. Consider the classical linear measurement model

$$\mathbf{r} = \Psi \mathbf{t} + \mathbf{w}, \tag{3.14}$$

where $\mathbf{w}$ is Gaussian noise and $\mathbf{r}$ is a known measurement composed of some linear combination of the columns of known dictionary matrix Ψ. The goal of CS is to reliably determine $\mathbf{t}$ from knowledge of $\mathbf{r}$ and Ψ given that $\mathbf{t}$ is sparse, (has few non-zero values) or approximately sparse (has entries that decay rapidly when reordered by magnitude).

The central tenet of CS is that if $\mathbf{t}$ is sparse then most of the salient information in $\mathbf{r}$ can be captured by a few dictionary vectors (for appropriately designed dictionaries). Additionally, recent theoretical results have established that $\mathbf{t}$ can be solved using tractable mixed norm optimization programs [15]-[16], efficient greedy algorithms, [17], fast iterative thresholding algorithms [18], or Bayesian probabilistic methods [19]. Proofs establishing the reliability of the mentioned reconstruction procedures depend on a certain property of the dictionary matrix Ψ, and the sparsity of $\mathbf{t}$. Specifically, the key property of Ψ for proving the optimality of reconstruction is the restricted isometry property (RIP) [20].

There are currently no known algorithms that check the RIP for a given matrix in polynomial time, though one of the reasons that has lead to the widespread use of CS in many fields is the discovery that certain probabilistic constructions of matrices satisfy the RIP with high probability [21]. In this paper we assume the RIP holds for the dictionary matrix defined in section 3.3.2, and test this theory with simulations performed in section 3.4.

Of the many CS reconstruction algorithms noted earlier, we use the LASSO [22] (which is sometimes also referred to as basis pursuit denoising [16]). The LASSO is a well studied method for solving compressive sensing problems which has good reconstruction error bounds [23] and is computationally attractive due to the many publicly available software packages for computing it. The LASSO in Lagrangian form is

$$\min_{\mathbf{t}} \|\mathbf{r} - \Psi\mathbf{t}\|_2^2 + \mu\|\mathbf{t}\|_1, \tag{3.15}$$

where μ is a positive regularization parameter satisfying $0 \leq \mu \leq 2\|\Psi^H\mathbf{r}\|_\infty$ [7]. In the next section we will show that the path angles traveled by a multipath MIMO signal can be solved using the LASSO.

3.3.2 MIMO Beamforming

From section 3.2.2 it is clear that an estimate of a channel $\mathbf{H}$ can be made from MIMO systems transmitting certain sequences. Additionally, from eq (3.2) we see that a MIMO channel can be written as the sum of a small number of paths, thus the channel is sparse in the dictionary formed from the array responses from each possible path angle. In general we will only have estimates of the channel, $\hat{\mathbf{H}}$ (from eq (3.13)), which are used to produce angular domain channel estimates, $\hat{\mathbf{H}}^a$.

Define $\mathbf{h} = \text{vec}(\mathbf{H})$ where $\text{vec}(.)$ stacks the columns of a matrix, and $\tilde{\mathbf{a}}(\theta_p, \phi_p) = \mathbf{a}_R(\theta_p) \otimes \mathbf{a}_T(\phi_p)$ where $\otimes$ is the Khatri-Rao product [24]. The dictionary $\mathbf{A}_D \in \mathbb{C}^{Q_R Q_T \times N_R N_T}$ of path angles is defined as

$$\mathbf{A}_D = \left[\tilde{\mathbf{a}}(\theta_1, \phi_1), \dots, \tilde{\mathbf{a}}(\theta_{Q_R}, \phi_{Q_T}) \right], \tag{3.16}$$

where Q_T and Q_R represent an arbitrary number of transmit and receive angles evenly spaced between (ϕ_{min}, ϕ_{max}) and $(\theta_{min}, \theta_{max})$. In practical terms, Q_T and Q_R are the number of

grid points which the transmit and receive angle space will be divided into. For unknown sparse vector $\mathbf{h}^a = \text{vec}(\mathbf{H}^a) \in \mathbb{C}^{Q_R Q_T}$,

$$\hat{\mathbf{h}} = \mathbf{A}_D \mathbf{h}^a + \eta, \tag{3.17}$$

where $\eta \in \mathbb{C}^{N_R N_T}$ is the noise due to approximation which is assumed to be from a Gaussian distribution.

Solving eq (3.15) with variables from eq (3.17), the LASSO objective function [25] produces a sparse estimate of the angular domain channel matrix in vector form.

$$\hat{\mathbf{h}}^a = \min_{\mathbf{h}^a} \|\hat{\mathbf{h}} - \mathbf{A}_D \mathbf{h}^a\|_2^2 + \mu \|\mathbf{h}^a\|_1. \tag{3.18}$$

In this paper we set μ to half its maximum value (see [7] for further discussion).

Once $\hat{\mathbf{h}}^a$ has been solved it is cast back into matrix form, $\hat{\mathbf{H}}^a = \text{vec}^{-1}(\hat{\mathbf{h}}^a)$ which was introduced in eq (3.4). Each element of the angular domain channel matrix is associated with an AoD and AoA through which the signal could have traveled. The magnitude of each element of $\mathbf{H}^a$ represents the path gain of the signal traveling through the path angle pair associated with that element.

3.4   Simulation

Compressive MIMO beamforming was simulated and tested against two other beamforming techniques; conventional beamforming (CBF) [26] and 2D MUSIC [27], both described in the appendix. CBF and MUSIC provide estimates of the angular domain power spectrum, which are compared to the estimate produced from compressive MIMO beamforming.

A simulated signal $\mathbf{y}_t \in \mathbb{C}^{N_R}$ was constructed according to eq (3.5), repeated here for convenience

$$\mathbf{y}_t = \sum_{j=1}^{Q_R} \sum_{i=1}^{Q_T} \mathbf{H}_{i,j}^a \mathbf{a}_R(\theta_j) \mathbf{a}_T^H(\phi_i) \mathbf{x}_t + \mathbf{w}_t = \tilde{\mathbf{y}}_t + \mathbf{w}_t, \tag{3.19}$$

where $t = [1, \ldots, T]$, $Q_T = Q_R = 30$ and $\mathbf{H}^a$ is a randomly generated sparse matrix whose non-zero elements are unit magnitude with phase drawn from a uniform distribution over the range $[0, 2\pi]$. The sparsity of $\mathbf{H}^a$ was controlled by parameter P ($P = 3$ in figure 3.2), and each $\mathbf{x}_t$ was a known realization from a complex normal distribution $\mathbf{x}_t \in \mathbb{C}^{N_T} \sim \mathcal{CN}(\mathbf{0}, \mathbf{I})$ (Gaussian sequences obey eq (3.12) with high probability) which was generated independently for each t. $\mathbf{y}_t$ was first generated from random but known realizations of $\mathbf{H}^a$ and $\mathbf{x}_t$, then complex Gaussian noise $\mathbf{w}_t \in \mathbb{C}^{N_R} \sim \mathcal{CN}(\mathbf{0}, \sigma^2 \mathbf{I})$ was added such that any desired SNR could be met, where

$$\text{SNR(dB)} = 10 \log \left(\frac{\|\mathbf{H}\mathbf{x}_t\|_2^2}{\|\mathbf{w_t}\|_2^2} \right) = 10 \log \left(\frac{\|\tilde{\mathbf{y}}_t\|_2^2}{\|\mathbf{w_t}\|_2^2} \right). \tag{3.20}$$

and $\|.\|_2^2$ is the squared ℓ_2 norm.

From $\mathbf{y}_t$ and $\mathbf{x}_t$, $\hat{\mathbf{H}}$ was estimated according to eq (3.13) with $\mathcal{P} = N_T T$. Given $\hat{\mathbf{H}}$, eq (3.18) was used to solve for $\hat{\mathbf{H}}^a$. Figure 3.2 shows plots of $|\mathbf{H}^a|^2$ alongside the angular power spectrum recovered from CBF, ($|\mathbf{H}_{\text{CBF}}^a|^2$ specified in eq (3.27) of the appendix) and MUSIC ($F(\theta, \phi)$ from eq (3.30) in the appendix) applied to the simulated noiseless data with $N_T = N_R = 16$ and $N_T = N_R = 4$.

Note that both CBF and MUSIC, are limited by the maximum rank of $\mathbf{H}$, which results in the blurred spectrum seen in figure 3.2. The maximum rank of $\mathbf{H}$ is determined by the number of transmitters and receivers in the MIMO system rank$(\mathbf{H}^a) \leq \min(N_T, N_R)$. Compressive MIMO beamforming is not limited in precision by the rank of $\mathbf{H}$, but rather by how many columns of dictionary $\mathbf{A}_D$ can be formed before the dictionary ceases to satisfy the RIP property. When $\mathbf{A}_D$ is populated by too many column vectors $\tilde{\mathbf{a}}(\theta, \phi)$ (which is equivalent to quantizing (θ, ϕ) space too finely) there will be high coherence between the columns of $\mathbf{A}_D$ to the point where the dictionary will cease to satisfy the RIP. It is infeasible to check that any given $\mathbf{A}_D$ satisfies the RIP because
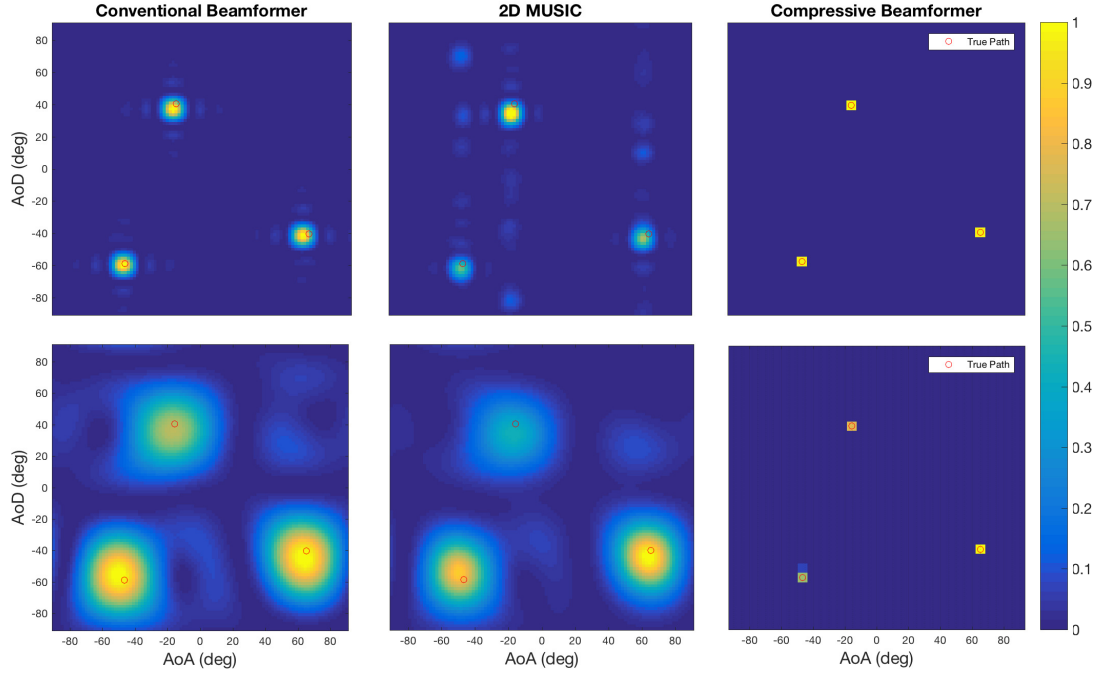
Figure 3.2: Angular power spectrum from various beamforming techniques performed on simulated noiseless signals with $T = 1000, P = 3, \mu = .5\mu_{max}$. (Top) $N_T = N_R = 16$. (Bot) $N_T = N_R = 4$. (Left) Conventional beamforming, (Middle) 2D MUSIC, (Right) Compressive MIMO beamforming with $Q_R = Q_T = 30$. Transmitter and receiver spacing each set to $\frac{\lambda}{2}$.

there is no known algorithm that works in polynomial time, however we assume that a dictionary formed from quantizing the angle space into $Q_R = Q_T = 30$ is acceptable because the simulation recovers simulated paths with satisfactory accuracy.

The performance of compressive MIMO beamforming is tested using two error metrics for channels of varying sparsity and SNR given $Q_R = Q_T = 30$. The first error metric, ε_A, represents angle error and is defined as the euclidean distance (in (θ, ϕ) space) between the P true path angle pairs of $\mathbf{H}^a$ and the best matching set of P path angle pairs from $\hat{\mathbf{H}}^a$.

$$\varepsilon_A = \frac{1}{P} \sum_{p=1}^{P} \sqrt{(\hat{\theta}_p - \theta_p)^2 + (\hat{\phi}_p - \phi_p)^2}, \tag{3.21}$$

where θ_p and ϕ_p are the receive and transmit angles from path p of $\mathbf{H}^a$, $\hat{\theta}_p$ and $\hat{\phi}_p$ are the receive and transmit angles from path p of $\hat{\mathbf{H}}^a$, and the units of ε_A are degrees. The best set of matching paths from $\hat{\mathbf{H}}^a$ was found as the set of paths producing the smallest ε_A using exhaustive search. It was found that the number of non-zero elements in $\hat{\mathbf{H}}^a$ was always equal to or greater than that of $\mathbf{H}^a$. Note that simulations were performed over an angle space ranging from $[-90°, 90°]$, so an average error of $18°$ represents a 10% error over the full space. In section 3.6 we will present findings over a much smaller angle space, for which we expect the same percentage error rather than absolute error.

The second error metric is ε_N, is normed error defined as $\varepsilon_N = \frac{1}{P}\|\mathbf{H}^a - \hat{\mathbf{H}}^a\|_F^2$. Normed error is simply a measure of the mean squared difference between the true and estimated angular domain channel matrices.

Each error metric was calculated for $N = 200$ Monte Carlo trials of simulated signals of varying SNR and sparsity, then plotted in figure 3.3. The random number generator seed was reset for each unique parameterization. We observe that both metrics show positive correlation between error and SNR. Angle error ε_A appears nearly constant for signals composed of $P > 1$, indicating that more paths does not lower the angular accuracy of the estimated paths. Normed

error curves indicate that the mismatch between true and reconstructed angular channel matrices is much greater for signals from multiple paths. Each curve appears to flatten for SNR above -15 dB. We conclude compressive MIMO beamforming will have sufficient accuracy for received signals whose SNR is above -15 dB.

3.5   Experimental Setup and Data

The coast of southern California is known as a hotspot for atmospheric ducts [1], which can act as leaky waveguides for EM waves. The goal of the experiment was to observe the impact of a ducting environment on a MIMO communications channel, particularly the change in multipath properties of the channel with time. No measurements of the atmospheric refractivity
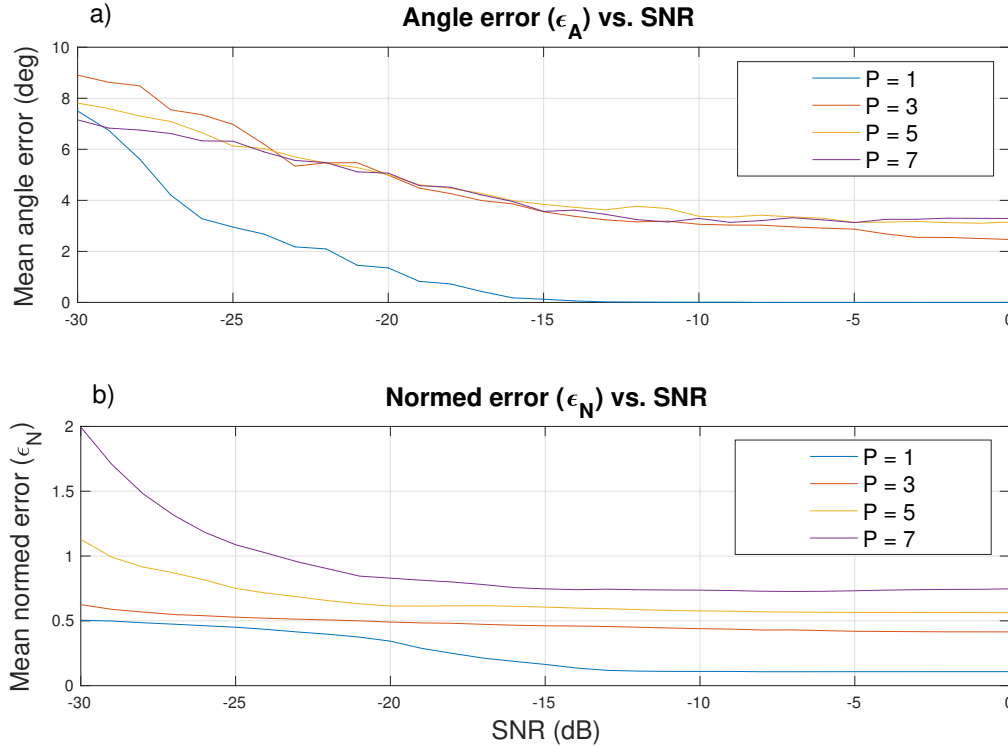
Figure 3.3: Average error of $N = 200$ Monte Carlo reconstructions of $\hat{\mathbf{H}}^a$ using compressive MIMO beamforming with $\mu = .5\mu_{max}$ on simulated signals of varying SNR and sparsity P. a) Angle error (ε_A), b) Normed error (ε_N).

profile were taken, so the observations at the receiver array are understood to reflect the typical characteristics of a refractive channel rather than being the result of any specific type of duct.

3.5.1 Transmitters and Receivers

Data was collected from vertically positioned ULAs of 4 transmitters and 4 receivers. The transmitter array was positioned at the end of Scripps Pier, 332 m from shore, with array spacing of 3.8 m while the receiver array was located 1000 m inland at Camp Pendleton with array spacing of 4 m. The transmitters will be referred to as T1-T4, where T1 is the topmost transmitter. Likewise, the receivers will be referred to as R1-R4 where R1 is the topmost receiver. From the array spacing the maximum resolvable angles were $\phi_{max} = 1.63°$ and $\theta_{max} = 1.55°$, which is within the normal range of expected AoA and AoD's for such long range over the horizon setups [5]. The topmost elements of the transmitter and receiver arrays were approximately 34 and 32 m above sea level respectively. The arrays were located 40.72 km apart, far enough that the line of sight path between all antennas was obstructed by the horizon. The elements of both arrays were pointed facing each other in azimuth, and with an elevation angle of $0°$.

A known, narrowband, length 2^{13} Zadoff-Chu (ZC) signal, $\mathbf{z}$, [10] was sent from each transmitter on carrier frequency 1.385 GHz. ZC signals are complex, constant magnitude, and satisfy the following property

$$\mathbf{z}^H(\mathbf{Pz}) = 0, \tag{3.22}$$

where $\mathbf{P}$ is any cyclic permutation of the identity matrix with $\mathbf{P} \neq \mathbf{I}$. Eq (3.22) should be interpreted to mean any ZC sequence is orthogonal to any circularly shifted version of itself. By sending identical ZC signals with unique circular shifts from each transmitter, a training matrix which satisfies (3.12) is formed. The transmitted waveforms from [T1,...,T4] were identical, circularly shifted ZC sequences, $\mathbf{X} \in \mathbb{C}^{N_T \times 2^{13}} = [\mathbf{z}_0, \mathbf{z}_{500}, \mathbf{z}_{1200}, \mathbf{z}_{2000}]^T$ where $\mathbf{z}_i$ is a ZC sequence

circularly shifted by i samples. Each snapshot is $8 \times 2^{13} = 2^{16}$ samples.

All receivers coherently recorded four snapshots of 2^{16} samples taken at sample rate 1.25 MHz every fifteen minutes. Figure 3.4 shows matched filter outputs between the transmitted ZC sequence and all receivers for a single snapshot. The matched filter output $\mathbf{m}_i$ of receiver i is defined as

$$\mathbf{m}_i[t] = \sum_{m=-\infty}^{\infty} \mathbf{y}_i[m]\mathbf{z}[t-m], \tag{3.23}$$

where $\mathbf{y}_i[t]$ represents index t of the measurement vector from receiver i and $\mathbf{z}$ is the unshifted ZC sequence transmitted by T1. Each peak in figure 3.4 confirms the arrival of a ZC sequence, the first peak being from T1, the second from T2, and so on. Because the four transmitters each sent repeating 2^{13} sample waveforms, the four arrival spikes in the matched filter are expected to repeat every 2^{13} samples (8 repetitions per snapshot). The magnitude of each spike roughly represents the strength of the path between each transmitter and receiver.

We note the arrival of the ZC sequence from T3 and T4 in figure 3.4 are significantly weaker than the others. We explore two possible explanations, first that both T3 and T4 are positioned at significantly lower elevations than T1 and T2, thus the horizon presents a greater obstacle. The decreased receive power may be the result of signal attenuation from propagating over the horizon, however this does not explain why the signal from T4 arrives stronger than that of T3. Second, multipath environments can cause fading [28], resulting in null zones where the signal and its reflections effectively cancel each other out. It is possible that the receiver array lies in a null zone for the signals from T3.

3.6   Results

Receiver noise variance was not recorded during the measurements. We assume each receiver was subject to the same noise level for the entire testing period, thus received power
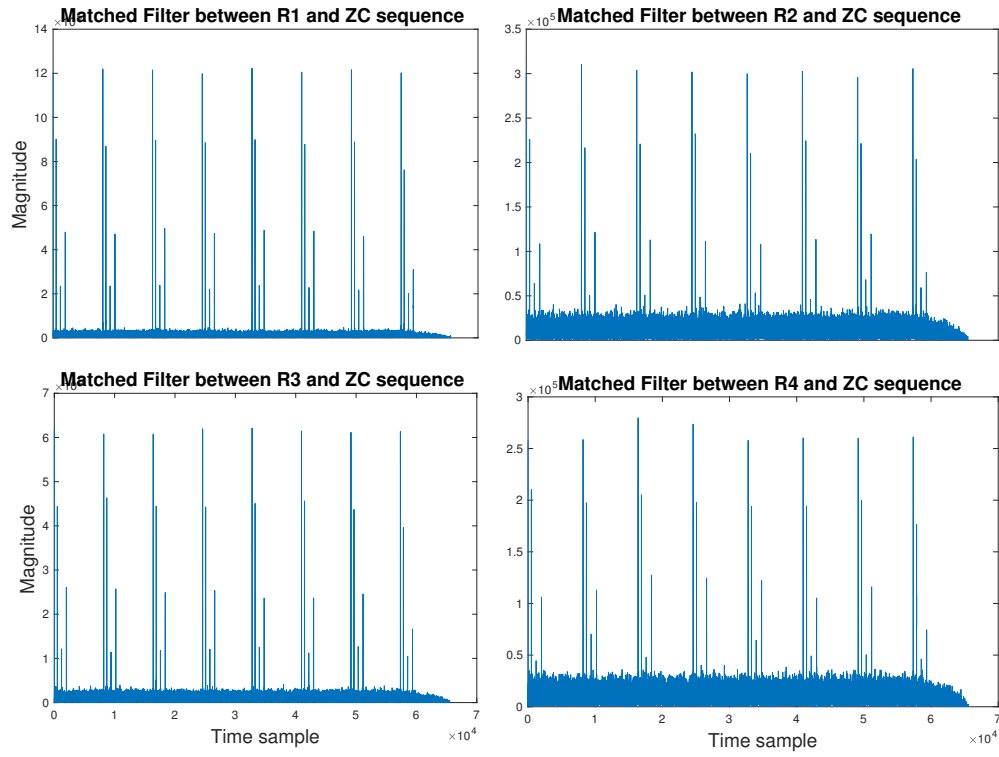
Figure 3.4: Single snapshot matched filter between each receiver and ZC sequence taken on January 24, 2016 at 00:00:18. Each spike represents the arrival of a length 2^{13} sample ZC signal from a transmitter.
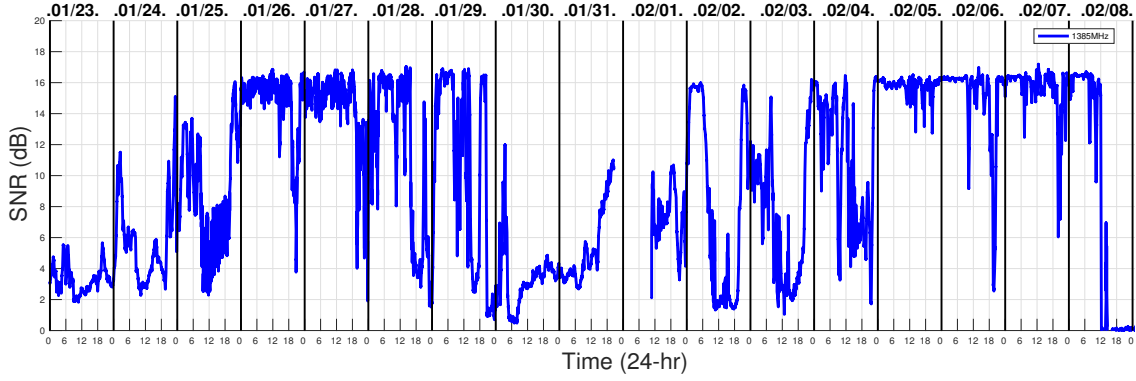
Figure 3.5: Average received power (dB) over the test period from Jan 23 - Feb 09, 2016.

represents some scaling of SNR. Average received power was calculated as $P_r = \frac{1}{N_R}\|\mathbf{Y}\|_F^2$ for each snapshot $\mathbf{Y} \in \mathbb{C}^{N_R \times 2^{16}}$. The average received power over the full 18 day test period between January 23 and February 09, 2016 is plotted in figure 3.5. Note that the array went down for 18 hours on January 31st, leading to a short gap in the data.

It is well documented that atmospheric ducts, particularly evaporation ducts, can increase the SNR of over the horizon EM signals [1], [5]. We assume that periods for which the received power is at a maximum are indicative of some form of ducting [29]. Using the periods between January 25-29 and Feb 5-8 as examples of ducting events, we analyze the impact of ducting on the reconstructed path angle pairs of $\hat{\mathbf{H}}^a$ from the experimental data.

All receiver returns were processed using compressive MIMO beamforming. The objective was to visualize the evolution of the multipath channel over time. The data was divided into two hour intervals, 32 snapshots per interval (4 snapshots per 15 minutes = 32 snapshots per two hours), and the estimate $\hat{\mathbf{H}}^a$ from each snapshot was normalized to limit local SNR fluctuations. All normalized estimates of $\hat{\mathbf{H}}^a$ within an interval were averaged to produce $\hat{\mathbf{H}}_{int}^a$, representing the fraction of path gain through each angle during the interval, normalized to account for power fluctuations between snapshots. Formally,

67

$$\hat{\mathbf{H}}^a_{int} = \frac{1}{N} \sum_{n=1}^{N} \frac{\hat{\mathbf{H}}^a_n}{\sum_{i,j} |\hat{\mathbf{H}}^a_{n,i,j}|}, \qquad (3.24)$$

where $\hat{\mathbf{H}}^a_{n,i,j}$ is the (i,j)th element of the estimated angular domain channel matrix from snapshot n, and N is the number of snapshots in the interval. Note that the elements of each $\hat{\mathbf{H}}^a_{int}$ sum to one. $\hat{\mathbf{H}}^a_{int}$ is plotted in figures 3.6-3.8 for all two hour intervals between January 24th and January 26th, 2016.

We observe from the received power measurements of figure 3.5 that an atmospheric duct existed on January 26th. Figures 3.6-3.8 show the evolution of the multipath channel from January 24th through January 26. On January 24th the channel appears stable. There is little fluctuation in received power (mostly occurring between midnight and 6 AM) and two dominant path angle pairs are present at each interval. On January 25th, the received power measurements from figure 3.5 indicate the possible formation of a weak duct between midnight and 10 AM, and a strong duct after 6 PM. Active path angle pairs from January 25th presented in figure 3.7 do not show significant variation from those of January 24th. Again two dominant path angle pairs are present in the majority of the data.

Received power on January 26th (see figure 3.5) indicate the presence of a duct. Figure 3.8 shows that the multipath channel varied rapidly during daylight hours, but was stable and indistinguishable from a non-ducting channel during nighttime. The impact of ducting appears to be a lack of stability in the active path angle pairs, particularly in daylight hours. Figure 3.9 shows $\hat{\mathbf{H}}^a_{int}$ over much longer intervals of low and high measurements of received power. During low received power measurements of active path angle pairs are distributed tightly about specific receive angles, while high received power measurements lead to more unpredictable path angle pairs. It is possible that during periods of high receive power non-linearities in the receiver hardware caused inaccuracies in the data and is responsible for the increased variability of active path angle pairs during ducting, but this does not explain why these path angle pairs appear to
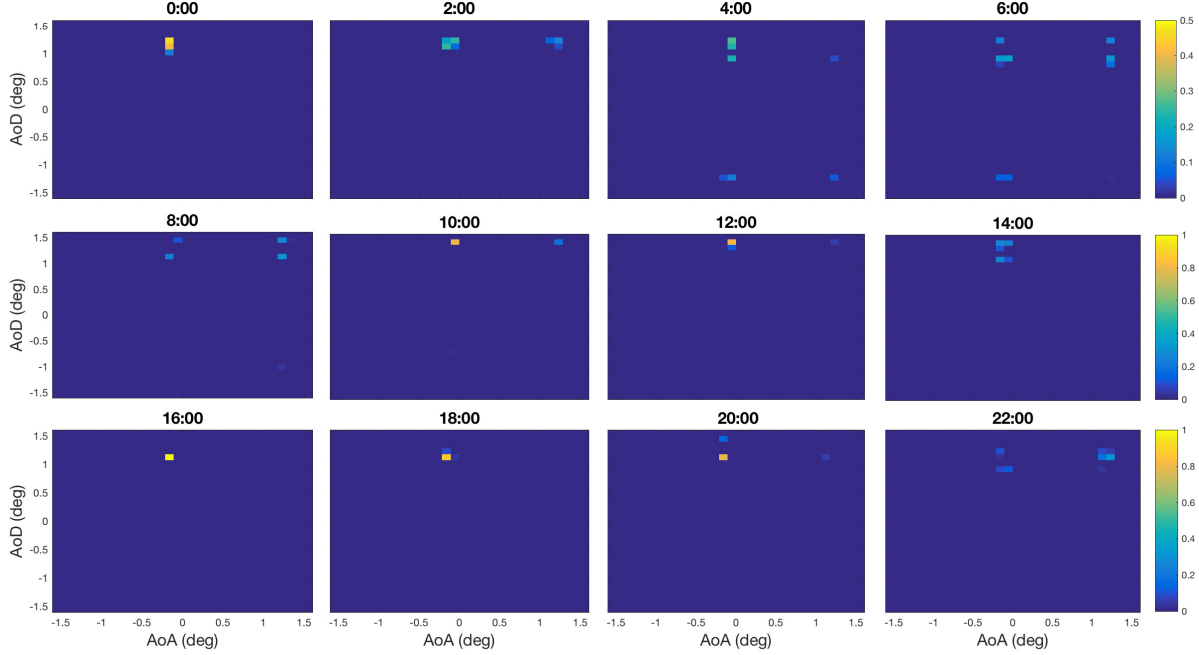
Figure 3.6: Averaged normalized path gain $\hat{\mathbf{H}}^a_{int}$ (from eq (3.24)) over 2 hour (32 snapshot) intervals vs. AoA and AoD taken on January 24, 2016.

fluctuate only during daylight hours in figure 3.8.

3.7   Conclusion

Compressive MIMO beamforming was simulated and applied to data recorded from a MIMO system. Simulations showed that compressive MIMO beamforming is capable of accurately identifying multipath signals with higher resolution than conventional beamforming and the 2D MUSIC algorithm. A MIMO array was set up in a ducting hotspot along the coast of southern California for the purpose of monitoring the evolution of its multipath channel over time. Matched filter processing of the received data confirmed the arrival of signals from the transmitters. An optimal estimate of the channel was made four times every fifteen minutes. From each channel measurement an angular domain channel matrix was calculated using compressive MIMO beamforming. The evolution of active path angle pairs from the angular domain channel matrix were examined over the measurement period.
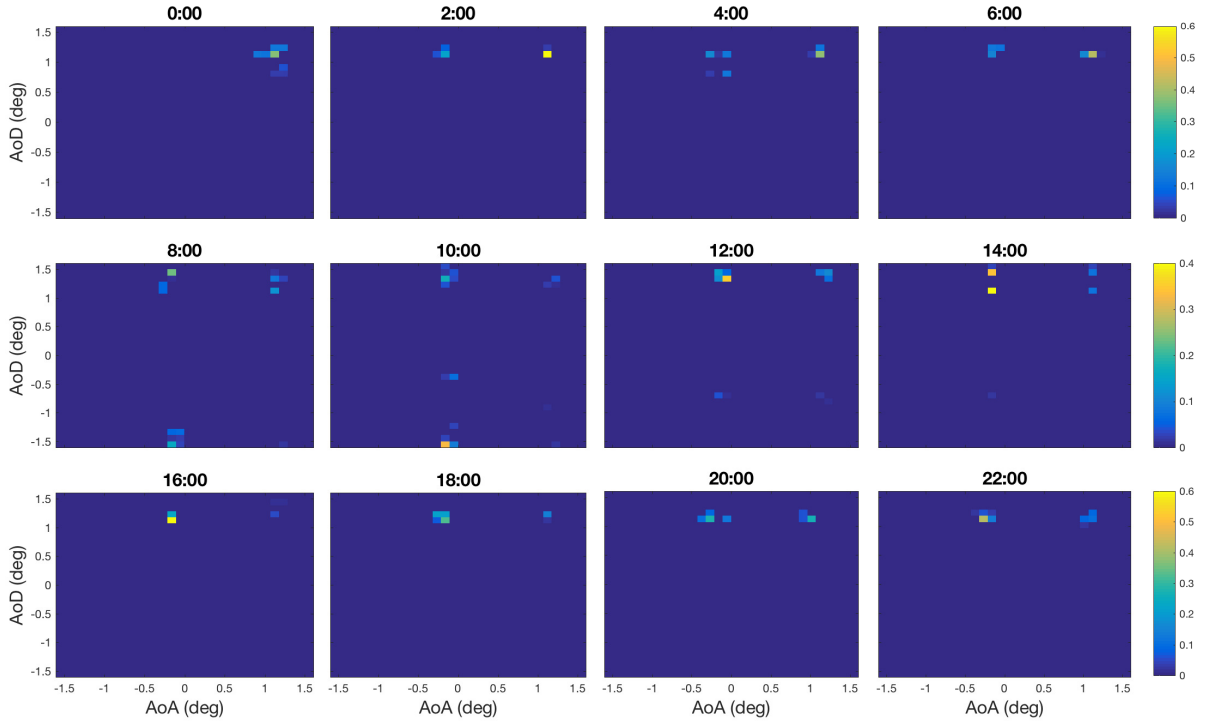
Figure 3.7: Averaged normalized path gain $\hat{\mathbf{H}}_{int}^{a}$ (from eq (3.24)) over 2 hour (32 snapshot) intervals vs. AoA and AoD taken on January 25, 2016.
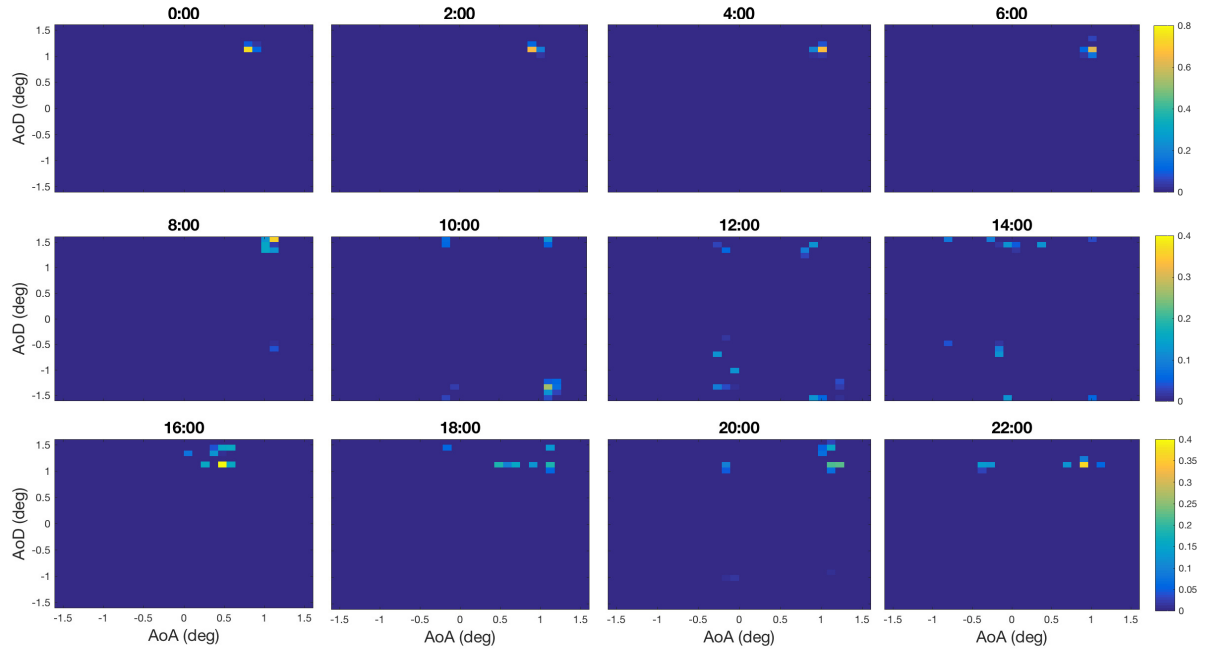
Figure 3.8: Averaged normalized path gain $\hat{\mathbf{H}}_{int}^{a}$ (from eq (3.24)) over 2 hour (32 snapshot) intervals vs. AoA and AoD taken on January 26, 2016.

70
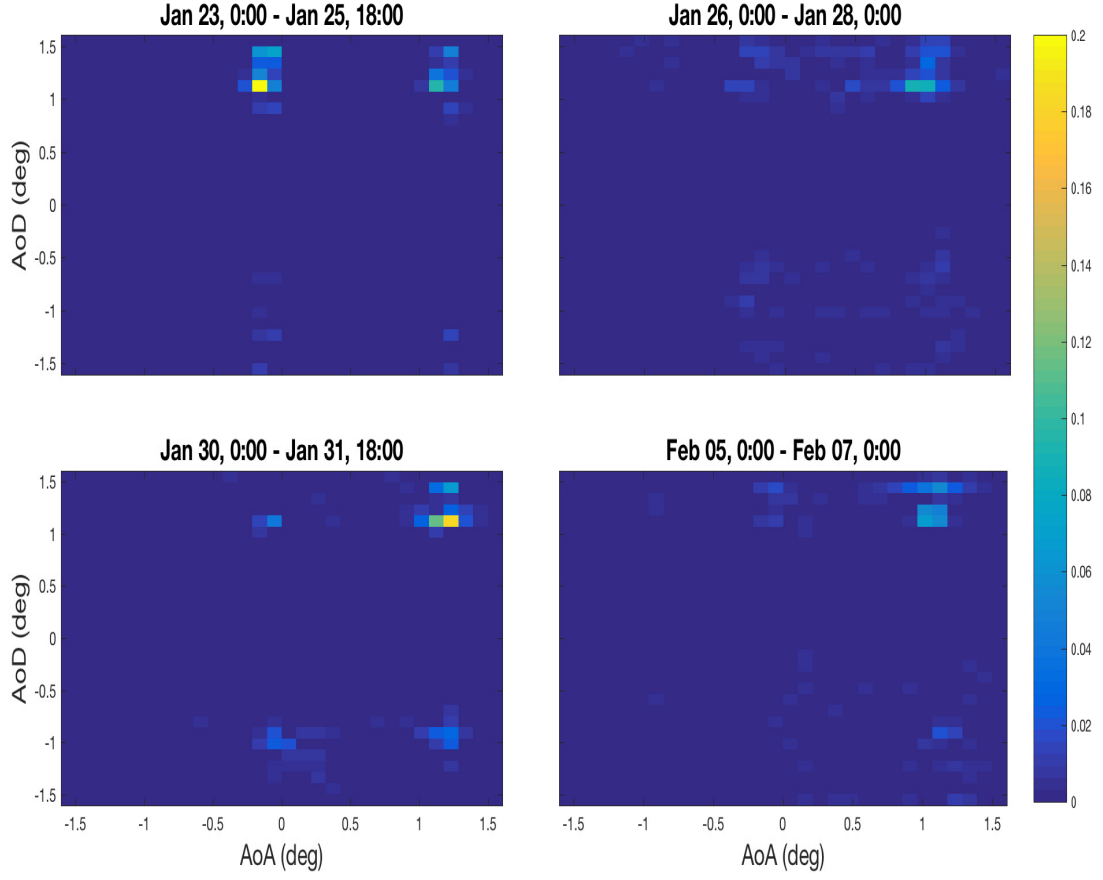
Figure 3.9: Averaged normalized path gain $\hat{\mathbf{H}}_{int}^{a}$ (from eq (3.24)) over long intervals of high and low received power.

The received power from the channel was used to determine the presence of ducting with periods of high received power assumed to indicate ducting and low received power to indicate a standard atmosphere. Two ducting events lasting multiple days were observed over the measurement period. The MIMO paths did not appear strongly related to received power or predictive of ducting. The active path angle pairs observed during ducting events were found to come from a wider range of path angles. Path angle pairs traveled by communications signals during ducting events were found to sometimes change quickly and unpredictably compared to those observed when no ducts were present.

No conclusive evidence was found that active path angle abnormalities from received MIMO communications signals can be used to predict ducting. The data, however, is only representative of one nearshore channel between points in southern California, and results may differ for channels in alternate locations. More data collection is required before conclusions can be drawn about the relation between ducting and the shape of a MIMO multipath channel. We suggest that refractivity profiles be taken alongside MIMO data in future related work so that the precise shape of the duct can be compared with the active path angle pairs of the MIMO signal.

3.8   Appendix

3.8.1   2D Conventional Beamforming

Like compressive MIMO beamforming, conventional beamforming (CBF) takes in a channel estimate $\hat{\mathbf{H}}$ and outputs an estimate of the angular domain channel matrix $\mathbf{H}^a_{CBF}$. From (3.2), a channel matrix $\mathbf{H}$ is the sum of P rank 1 matrices, each representing a path from transmitter to receiver. With this understanding we define dictionaries [6]

$$\mathbf{S}_R \in \mathbb{C}^{N_R \times Q_R} = \left[\mathbf{a}_R(-\theta_{min}), \ldots, \mathbf{a}_R(\theta_{max}) \right], \tag{3.25}$$

$$\mathbf{S}_T \in \mathbb{C}^{N_T \times Q_T} = \left[\mathbf{a}_T(-\phi_{min}), \ldots, \mathbf{a}_T(\phi_{max})\right], \tag{3.26}$$

where Q_R and Q_T are the number of bins into which the transmit and receive angle space is divided. The dictionaries in (3.25) and (4.20) have columns representing the array responses from signals arriving and departing from different angles. Larger Q_R and Q_T result in dictionaries that more finely divide the angular spectrum.

The angular domain representation of a channel $\mathbf{H}$ for conventional beamforming [6] is defined as

$$\mathbf{H}^a_{CBF} = \mathbf{S}^H_R \mathbf{H} \mathbf{S}_T. \tag{3.27}$$

Unlike compressive MIMO beamforming, the formulation of $\mathbf{H}^a_{CBF}$ in eq (3.27) does not assume sparsity in $\mathbf{H}^a_{CBF}$, so the CBF estimate of $\mathbf{H}^a$ is inherently different from that of compressive MIMO beamforming.

3.8.2 2D MUSIC

The 2D MUSIC algorithm [30], is a variation of the popular MUSIC subspace method [27]. Increased resolution is achieved by separating the signal and noise subspaces of the channel matrix through eigen-decomposition. The idea is that contributions to the channel $\mathbf{H}$ from noise are contained in the smallest eigenvalues of the channel covariance matrix, and by removing such eigenvalues, a de-noised version of the channel is created.

The channel covariance is

$$\mathbf{R} = E[\mathbf{h}\mathbf{h}^H], \tag{3.28}$$

where $\mathbf{h} = \text{vec}(\mathbf{H})$, which has eigen-decomposition

$$\mathbf{R} = \mathbf{U}_S \Lambda_S \mathbf{U}_S^H + \mathbf{U}_N \Lambda_N \mathbf{U}_N^H. \tag{3.29}$$

Here $\mathbf{U}_S$ and $\mathbf{U}_N$ are the matrices whose columns contain the eigenvectors of the signal and noise subspaces, and Λ_S, Λ_N are diagonal matrices whose elements are the corresponding eigenvalues. If the signal primarily travels through n paths, the dimension of the signal subspace is n. Under this assumption $\mathbf{U}_S$ will contain the n eigenvectors corresponding to the n largest eigenvalues. The spectrum function for 2D MUSIC is given as [11]

$$F(\theta, \phi) = \frac{1}{\tilde{\mathbf{a}}^H(\theta, \phi) \mathbf{U}_N \mathbf{U}_N^H \tilde{\mathbf{a}}(\theta, \phi)}. \tag{3.30}$$

$F(\theta, \phi)$ is a continuous function which represents the relative strength of the signal traveling through angles (θ, ϕ), similar to estimates of $\mathbf{H}^a$ from CBF and compressive MIMO beamforming. An example of $F(\theta, \phi)$ is shown in figure 3.2.

3.9   Acknowledgments

The text of Chapter Three is in full a reprint of the material as it appears in Mark Wagner, Santosh Nannuru, and Peter Gerstoft, "Compressive MIMO Beamforming of Data Collected in a Refractive Environment," *Radio Science* 52.12 (2017): 1458-1471.

Bibliography

[1] T. Haack and S.D. Burk, "Summertime marine refractivity conditions along coastal california," *J. App. Meteoro.*, vol. 40, no. 4, pp. 673–687, 2001.

[2] KH Craig and MF Levy, "Parabolic equation modelling of the effects of multipath and ducting on radar systems," in *IEEE Proceedings F. Radar and Signal Process*. IET, 1991, vol. 138, pp. 153–162.

[3] M. Wagner, P. Gerstoft, and T. Rogers, "Estimating refractivity from propagation loss in turbulent media," *Radio Sci.*, vol. 51, no. 12, pp. 1876–1894, 2016.

[4] I.J. Timmins and S. O'Young, "Marine communications channel modeling using the finite-difference time domain method," *IEEE Transactions on vehicular technology*, vol. 58, no. 6, pp. 2626–2637, 2008.

[5] P. Gerstoft, L.T. Rogers, J.L. Krolik, and W.S. Hodgkiss, "Inversion for refractivity parameters from radar sea clutter," *Radio science*, vol. 38, no. 3, 2003.

[6] D. Tse and P. Viswanath, *Fundamentals of wireless communication*, Cambridge university press, 2005.

[7] C.F. Mecklenbräuker, P. Gerstoft, and E. Zöchmann, "c–lasso and its dual for sparse signal estimation from array data," *Signal Processing*, vol. 130, pp. 204–216, 2017.

[8] H.M. Wang, X.Q. Gao, B. Jiang, X.H. You, and W. Hong, "Efficient mimo channel estimation using complementary sequences," *Iet Communications*, vol. 1, no. 5, pp. 962–969, 2007.

[9] M. Biguesh and A.B. Gershman, "Training-based mimo channel estimation: a study of estimator tradeoffs and optimal training signals," *IEEE transactions on signal processing*, vol. 54, no. 3, pp. 884–893, 2006.

[10] D. Chu, "Polyphase codes with good periodic correlation properties (corresp.)," *IEEE Transactions on information theory*, vol. 18, no. 4, pp. 531–532, 1972.

[11] W.Q. Wang, "Virtual antenna array analysis for mimo synthetic aperture radars," *International Journal of Antennas and Propagation*, vol. 2012, 2012.

[12] H. Bolcskei, D. Gesbert, and A.J. Paulraj, "On the capacity of ofdm-based spatial multiplexing systems," *IEEE Transactions on communications*, vol. 50, no. 2, pp. 225–234, 2002.

[13] M. Pesavento, C.F. Mecklenbräuker, and J.F. Böhme, "Multidimensional rank reduction estimator for parametric mimo channel models," *EURASIP Journal on Advances in Signal Processing*, vol. 2004, no. 9, pp. 839148, 2004.

[14] P.W. Chan, D. Lee, F. Tam, I. Chih-Lin, R. Cheng, and V. Lau, "Angular-domain channel model and channel estimation for mimo system," in *IEEE GLOBECOM 2008-2008 IEEE Global Telecommunications Conference*. IEEE, 2008, pp. 1–5.

[15] R. Tibshirani, "Regression shrinkage and selection via the LASSO," *J. Royal Stat. Soc. B.*, pp. 267–288, 1996.

[16] S.S. Chen, D.L. Donoho, and M.A. Saunders, "Atomic decomposition by basis pursuit," *SIAM review*, vol. 43, no. 1, pp. 129–159, 2001.

[17] S.G. Mallat and Z. Zhang, "Matching pursuits with time-frequency dictionaries," *IEEE Trans. Sig. Proc.*, vol. 41, no. 12, pp. 3397–3415, 1993.

[18] I. Daubechies, M. Defrise, and C. De Mol, "An iterative thresholding algorithm for linear inverse problems with a sparsity constraint," *Communications on Pure and Applied Mathematics: A Journal Issued by the Courant Institute of Mathematical Sciences*, vol. 57, no. 11, pp. 1413–1457, 2004.

[19] M.E. Tipping, "Sparse bayesian learning and the relevance vector machine," *Journal of machine learning research*, vol. 1, no. Jun, pp. 211–244, 2001.

[20] E.J. Candes, "The restricted isometry property and its implications for compressed sensing," *Comptes rendus mathematique*, vol. 346, no. 9-10, pp. 589–592, 2008.

[21] M. Rudelson and R. Vershynin, "On sparse reconstruction from fourier and gaussian measurements," *Communications on Pure and Applied Mathematics: A Journal Issued by the Courant Institute of Mathematical Sciences*, vol. 61, no. 8, pp. 1025–1045, 2008.

[22] Robert Tibshirani, Michael Saunders, Saharon Rosset, Ji Zhu, and Keith Knight, "Sparsity and smoothness via the fused lasso," *Journal of the Royal Statistical Society: Series B (Statistical Methodology)*, vol. 67, no. 1, pp. 91–108, 2005.

[23] P.J. Bickel, Y. Ritov, and A.B. Tsybakov, "Simultaneous analysis of lasso and dantzig selector," *The Annals of Statistics*, vol. 37, no. 4, pp. 1705–1732, 2009.

[24] C. Steffens, Y. Yang, and M. Pesavento, "Multidimensional sparse recovery for mimo channel parameter estimation," in *2016 24th European Signal Processing Conference (EUSIPCO)*. IEEE, 2016, pp. 66–70.

[25] D.L. Donoho, "Compressed sensing," *IEEE Transactions on information theory*, vol. 52, no. 4, pp. 1289–1306, 2006.

[26] M.S. Bartlett, "Smoothing periodograms from time series with continuous spectra," *Nature*, vol. 161, no. 4096, pp. 686–687, 1948.

[27] R. Schmidt, "Multiple emitter location and signal parameter estimation," *IEEE Trans. Antennas. Prop.*, vol. 34, no. 3, pp. 276–280, 1986.

[28] G.J. Foschini and M.J. Gans, "On limits of wireless communications in a fading environment when using multiple antennas," *Wireless personal communications*, vol. 6, no. 3, pp. 311–335, 1998.

[29] S. Vasudevan, R.H. Anderson, S. Kraut, P. Gerstoft, L.T. Rogers, and J.L. Krolik, "Recursive bayesian electromagnetic refractivity estimation from radar sea clutter," *Radio Science*, vol. 42, no. 02, pp. 1–19, 2007.

[30] X. Zhang, L. Xu, L. Xu, and D. Xu, "Direction of departure (dod) and direction of arrival (doa) estimation in mimo radar with reduced-dimension music," *IEEE communications letters*, vol. 14, no. 12, pp. 1161–1163, 2010.

Chapter 4

Gridless DOA Estimation and Root-MUSIC for Non-Uniform Arrays

The problem of gridless direction of arrival (DOA) estimation is addressed in the non-uniform array (NUA) case. Traditionally, gridless DOA estimation and root-MUSIC are only applicable for measurements from a uniform linear array (ULA). This is because the sample covariance matrix of ULA measurements has Toeplitz structure, and both algorithms are based on the Vandermonde decomposition of a Toeplitz matrix. The Vandermonde decomposition breaks a Toeplitz matrix into its harmonic components, from which the DOAs are estimated. First, we present the 'irregular' Toeplitz matrix and irregular Vandermonde decomposition (IVD), which generalizes the Vandermonde decomposition to apply to a more general set of matrices. It is shown that the IVD is related to the MUSIC and root-MUSIC algorithms. Next, gridless DOA is generalized to the NUA case using IVD. The resulting non-convex optimization problem is solved using alternating projections (AP). A numerical analysis is performed on the AP based solution which shows that the generalization to NUAs has similar performance to traditional gridless DOA.

4.1 Introduction

Estimating the direction of arrival (DOA) of one or more signals arriving at an array of sensors is an important topic in array signal processing and has a wide range of applications in radar, sonar, wireless communications, etc. Recently, the focus of DOA estimation has turned from classical subspace based DOA algorithms including MUSIC, root-MUSIC, and ESPRIT [1, 2, 3, 4] to newer compressive sensing based methods such as compressive DOA [5, 6, 7]. Compressive methods have the advantage that they are high resolution (resolve nearby DOAs), and require only a single measurement snapshot.

Early compressive DOA techniques approximated the measurements as a linear combination of a few array patterns from DOAs picked out of a grid of possible DOAs. However, this technique suffers from errors due to grid mismatch because true DOAs are not on a grid [8]. As a response came the family of off-grid, or *gridless* methods, which exploit sparsity in the *atomic norm* of the measurements [9, 10, 11, 12]. The atomic norm is the minimum number of "atoms" from a manifold required to reconstruct a vector, thus gridless DOA is the continuous analog to gridded compressive DOA.

Gridless DOA is an application of the continuous compressed sensing (CCS) spectral estimation problem, which was introduced in [9]. There have been many adaptations of CCS to related problems [13, 14], however, the atomic norm minimization formulation of gridless DOA for a line array is the focus of this work [15, 16]. There are other similar algorithms such as the enhanced matrix completion (EMaC) method [17] and gridless SPICE [11] whose formulations are similar to gridless DOA. We refer the reader to [18] for a comprehensive review of CCS for DOA.

CCS involves solving a semi-definite programming problem (SDP) whose objective is to find the lowest rank Toeplitz matrix which can explain the measurements. The frequencies composing the signal can be recovered through Vandermonde decomposition of the optimal

Toeplitz matrix [19]. This decomposition is known to be unique when the Toeplitz matrix is rank deficient [4]. In the context of DOA estimation, the parameters of the Vandermonde matrices, known as harmonics, indicate the DOAs. The weakness of gridless methods is that they are limited to regularly sampled measurements that can only be taken from a uniform linear array (ULA).

There have been some recent efforts towards extending gridless DOA to NUAs [20, 21, 22, 23]. Many of these are based on array interpolation, where the manifold of a NUA is interpolated back to that of a ULA. This idea traces back to "Fourier domain root-MUSIC" [24], which was used to extend the root-MUSIC algorithm to NUAs. There are many other interpolation based techniques for adapting older DOA algorithms to NUAs [25, 26, 27, 28, 29, 30, 31]. A drawback of these techniques is that the interpolation is inaccurate for the whole array field of view, and must be performed over many sectors of the array manifold.

This paper generalizes gridless DOA and root-MUSIC to NUAs by working directly on the NUA measurements (no interpolation). This is achieved through the *irregular Toeplitz* and *irregular Vandermonde* matrices. The word 'irregular' refers to the irregular sampling of the wave field by a NUA. The irregular Toeplitz matrix can be decomposed into irregular Vandermonde components, similar to Toeplitz and Vandermonde matrices. This allows for both root-MUSIC and gridless DOA to be extended to NUAs. The DOAs are recovered through irregular Vandermonde decomposition (IVD) of the irregular Toeplitz matrix.

The proposed extension of gridless DOA to NUAs is a rank minimization problem, which is non-convex [32]. A non-convex optimization problem is typically substituted for its convex relaxation and solved using a general solver [33], such as the alternating directions method of multipliers (ADMM) [34]. However, the proposed extension to NUAs cannot be easily cast to its convex relaxation. Instead, the proposed solution is based on the alternating projections (AP) algorithm [35, pg. 606], which finds a point of intersection between two or more sets by iteratively projecting an initial estimate between the sets.

The AP algorithm has been previously used to solve CCS problems [36], and implementation of AP to gridless DOA for NUAs is formulated by projecting onto the irregular Toeplitz set. The use of AP for solving similar non-convex optimization problems gives promising results [36, 37, 38]. A comparison of AP based gridless DOA against several competing algorithms, including ADMM, reveals the AP solution has similar or superior performance. An analysis is provided of the algorithm's performance in challenging scenarios such as when the measurements are corrupted with noise or the DOAs are closely spaced.

The paper is structured as follows: Sec. 4.2 contains an overview of gridless DOA and relevant concepts such as the Vandermonde decomposition and root-MUSIC algorithm. In Sec. 4.3, the IVD is introduced, which allows any positive semi-definite (PSD) matrix to be decomposed into harmonics sampled at known irregular intervals (array sensor locations). The IVD allows for non-Toeplitz matrices to be decomposed into their harmonic components. The DOAs are given by the harmonics. In Sec. 4.4, a modification of the gridless DOA problem is presented such that it can be applied to NUAs. A solution to the reformulated gridless DOA problem based on the AP algorithm is proposed. In Sec. 4.5, the proposed algorithm is tested on simulated measurements from both ULAs and NUAs. The results are for DOA estimation, but are also applicable to the broader CCS problem to irregularly sampled signals.

In the remainder of this chapter, lowercase bold letters represent vectors and uppercase bold letters represent matrices. Below is a short list of notation that will be used.

- $^\mathsf{T}$ Vector or matrix transpose.
- * Complex conjugate.
- $^\mathsf{H}$ Vector or matrix conjugate transpose.
- † Moore-Penrose pseudo-inverse.
- $\angle$ Phase angle.
- $\perp$ Orthogonal.

- $\succeq$ Positive semi-definite.
- $\|.\|_2$ Two norm.
- $\|.\|_F$ Frobenious norm.
- $\mathbb{E}$ Expected value.
- Tr   Matrix trace.
- $\text{diag}(\mathbf{X})$ Diagonal elements of matrix $\mathbf{X}$.
- $\text{diag}(\mathbf{x})$ Diagonal matrix with elements $\mathbf{x}$.
- $\text{span}(\mathbf{X})$ columnspace of matrix $\mathbf{X}$.
- $\mathbf{I}$ Identity matrix.
- $\mathbf{1}$ Ones matrix.
- $\mathbf{0}$ Zeros matrix.
- $\mathbf{x}^y$ Element-wise exponentiation.
- $\mathcal{U}(a,b)$ Uniform distribution from a to b.

4.2   Background: DOA Estimation for ULAs

4.2.1   Model Framework

Consider an array of M sensors receiving uncorrelated signals from K narrowband sources located in the far field of the array. Signals from each source arrive from angles $\theta = [\theta_1 \ldots \theta_K]^\mathsf{T}$, which are given in radians. The sources are assumed to be in the same plane as the array, and the sensors are positioned at points on a line given by $\mathbf{r} = [r_1 \ldots r_M]^\mathsf{T}$, where each value r_i denotes the distance of sensor i from an arbitrary origin point in units of half-wavelengths. By using half-wavelengths as the primary unit of distance, many of the equations surrounding DOA estimation are simplified. If each sensor records L snapshots of data, the measured signal can be

modeled as

$$\mathbf{Y} = \mathbf{Z} + \mathbf{N},$$

$$\mathbf{Z} = \mathbf{A}_s(\mathbf{r}, \theta)\mathbf{X},$$

(4.1)

where $\mathbf{Y} \in \mathbb{C}^{M \times L}$ are the recorded measurements, $\mathbf{X} = [\mathbf{x}_1 \ldots \mathbf{x}_K]^\mathsf{T} \in \mathbb{C}^{K \times L}$ contains the signals from each of K sources, Gaussian uncorrelated measurement noise is contained in $\mathbf{N} \in \mathbb{C}^{M \times L}$, and

$$\mathbf{A}_s(\mathbf{r}, \theta) = [\mathbf{a}(\mathbf{r}, \theta_1) \ldots \mathbf{a}(\mathbf{r}, \theta_K)],$$

(4.2)

$$\mathbf{a}(\mathbf{r}, \theta) = [e^{-j\pi r_1 \sin \theta} \ldots e^{-j\pi r_M \sin \theta}]^\mathsf{T},$$

(4.3)

is the array steering matrix whose columns model the phase pattern across the array from a signal arriving at angle θ. The column vectors are known as *array steering vectors* and are defined over $\theta \in [-\frac{\pi}{2}, \frac{\pi}{2})$. The goal is to recover θ given only knowledge of the sensor positions $\mathbf{r}$ and measurements $\mathbf{Y}$.

4.2.2 Vandermonde and Toeplitz Matrices

A Vandermonde matrix $\mathbb{C}^{M \times K}$ is defined as

$$\mathbf{V}(z) = [z^0 \, z^1 \ldots z^{(M-1)}]^\mathsf{T},$$

$$= [\mathbf{v}(z_1) \ldots \mathbf{v}(z_K)],$$

(4.4)

where $z = [z_1 \ldots z_K]^\mathsf{T}$ fully parameterizes the Vandermonde matrix [39, p. 409]. A single column of the Vandermonde matrix is defined as $\mathbf{v}(z) = [1 \, z^1 \ldots z^{M-1}]^\mathsf{T}$.

The array steering matrix of a ULA will have Vandermonde structure. Sensor positions of

a ULA are described as

$$\mathbf{r}_{\text{ULA}} = \alpha[0 \ 1 \ \dots \ M-1]^{\mathsf{T}} + \beta, \tag{4.5}$$

where α is an arbitrary scaling parameter and β is an arbitrary shifting parameter. In this case the θ parameters of (4.2) are related to the z parameters of (4.4) by

$$z_k = e^{-j\pi(\alpha+\beta)\sin(\theta_k)}, \tag{4.6}$$

$$\theta_k = -\sin^{-1}\left(\frac{\angle z_k}{(\alpha+\beta)\pi}\right). \tag{4.7}$$

The values of $\mathbf{r}_{\text{ULA}}$ manifest as scaled and shifted integers. The classical choice of parameters has $(\alpha, \beta) = (1, 0)$, and corresponds to a ULA with half-wavelength sensor spacing.

It is well known that any Toeplitz matrix, $\mathcal{T}$, can be decomposed into Vandermonde components,

$$\mathcal{T} = \mathbf{V}(z)\mathbf{D}\mathbf{V}(z)^{\mathsf{H}}, \tag{4.8}$$

where $\mathbf{D} \in \mathbb{R}^{K \times K}$ is diagonal with positive entries, the z parameters have unit magnitude, and $\mathcal{T}$ is a Hermitian symmetric Toeplitz matrix defined as

$$\mathcal{T}(\mathbf{u}) = \begin{pmatrix} u_1 & u_2^* & \cdots & u_M^* \\ u_2 & u_1 & \cdots & u_{M-1}^* \\ \vdots & \vdots & \ddots & \vdots \\ u_M & u_{M-1} & \cdots & u_1 \end{pmatrix}. \tag{4.9}$$

The first column, $\mathbf{u}$, of $\mathcal{T}$ fully parameterizes the matrix. The decomposition of (4.8) is unique when the Toeplitz matrix is not full rank [19]. The set of Toeplitz matrices will be denoted by the calligraphic letter $\mathcal{T}$.

The decomposition (4.8) will here be referred to as Vandermonde decomposition.
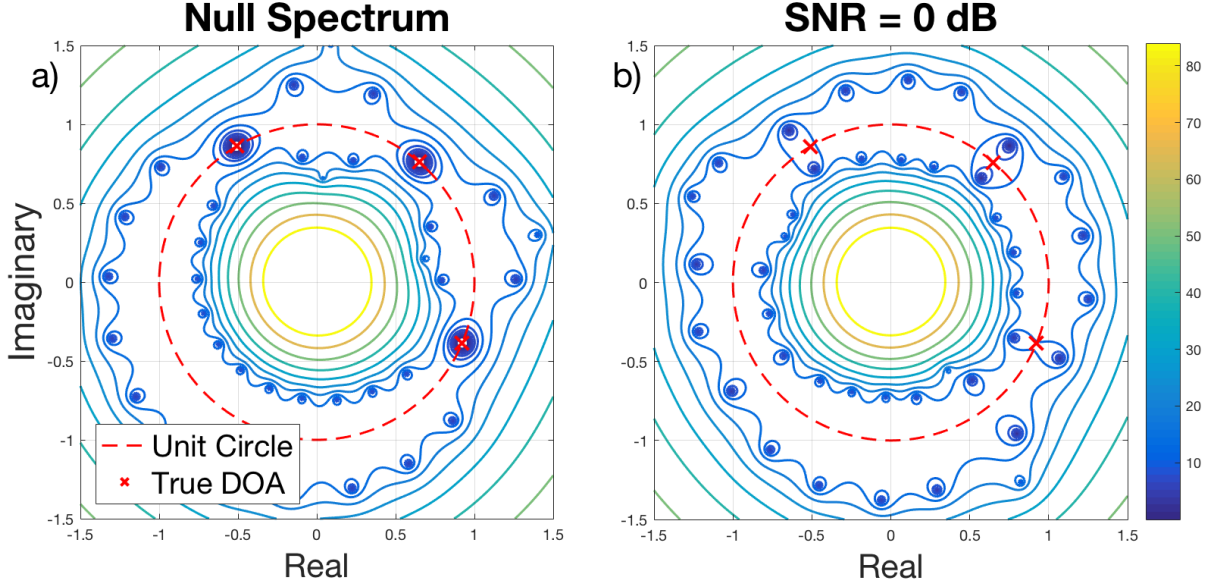
Figure 4.1: Null spectrum, (4.15), for half-wavelength spaced ULA measurements generated according to (4.1) using $M = 21$, $K = 3$, $L = 10$. DOAs located at $\theta = [-7.2, 15.9, 42.1]°$ (red x). a) Null spectrum contour of noiseless measurements. Red dashed line marks the complex unit circle. b) Same as a) with added noise such that $\|\mathbf{Z}\|_F = \|\mathbf{N}\|_F$, see (4.1).

4.2.3   Root-MUSIC and Vandermonde Decoposition

Root-MUSIC is a subspace based DOA algorithm [1, 2]. The algorithm consists of forming a polynomial from the sample covariance matrix of ULA measurements. The complex roots of the polynomial, z, are used to estimate the DOAs through (4.7). Without noise, the sample covariance matrix is Toeplitz and the polynomial roots are the z parameters of its Vandermonde decomposition (4.8). Root-MUSIC is valid only for measurements taken at a ULA.

The sample covariance matrix, $\mathbf{R}_{yy}$, is

$$\mathbf{R}_{yy} = \frac{1}{L}\mathbf{Y}\mathbf{Y}^{\mathsf{H}}, \quad \mathbb{E}[\mathbf{R}_{yy}] = \left(\mathbf{A}_s\Sigma_X\mathbf{A}_s^{\mathsf{H}} + \Sigma_N\right),$$

$$\Sigma_X = \frac{1}{L}\mathbb{E}\left[\mathbf{X}\mathbf{X}^{\mathsf{H}}\right], \quad \Sigma_N = \frac{1}{L}\mathbb{E}\left[\mathbf{N}\mathbf{N}^{\mathsf{H}}\right] = \sigma_N^2\mathbf{I},$$

(4.10)

where Σ_N is the expected noise covariance matrix, which becomes $\sigma_N^2\mathbf{I}$ for uncorrelated noise with variance σ_N^2.

If the measurements are noiseless, then $\text{span}(\mathbf{R}_{yy}) = \text{span}(\mathbf{A}_s)$. In this case, the columnspace and left nullspace of $\mathbf{R}_{yy}$ are known as the *signal and noise subspaces* respectively. When noise is present in the measurements an estimated basis to both spaces is found from the eigendecomposition of $\mathbf{R}_{yy}$,

$$\mathbf{R}_{yy} = \mathbf{U}_S \Lambda_S \mathbf{U}_S^H + \mathbf{U}_N \Lambda_N \mathbf{U}_N^H, \tag{4.11}$$

where $\Lambda_S \in \mathbb{R}^{K \times K}$ is diagonal with the K largest eigenvalues of $\mathbf{R}_{yy}$, $\mathbf{U}_S \in \mathbb{C}^{M \times K}$ is a matrix whose columns are the corresponding eigenvectors, and $\Lambda_N \in \mathbb{R}^{(M-K) \times (M-K)}$ and $\mathbf{U}_N \in \mathbb{C}^{M \times (M-K)}$ are matrices containing the remaining noise eigenvalues and eigenvectors. The matrices $\mathbf{U}_S$ and $\mathbf{U}_N$ are estimated bases to the signal and noise subspaces respectively. It must be noted that the signal and noise subspaces can only be estimated when $L \geq K$, because at least K snapshots are required to build a rank K approximation of $\mathbf{R}_{yy}$.

For noise free measurements, $\mathbf{U}_N$ will be composed of eigenvectors whose corresponding eigenvalues are 0. In this case $\mathbf{U}_N$ exactly spans the left nullspace of $\mathbf{A}_s$ and

$$\mathbf{U}_N \perp \mathbf{A}_s \implies \mathbf{U}_N^H \mathbf{A}_s = \mathbf{0}, \tag{4.12}$$

When noise is present, the eigenvectors composing $\mathbf{U}_N$ will have non-zero corresponding eigenvalues and $\mathbf{U}_N$ will be an approximation of the noise subspace.

Because the array is assumed uniform and linear, any array steering vector can be substituted with a column from a Vandermonde matrix. From (4.12), the *null spectrum* is formed [4, p.1159]

$$\begin{aligned} D(z) &= \|\mathbf{U}_N^H \mathbf{a}(\theta)\|_2^2 = \mathbf{a}(\theta)^H \mathbf{U}_N \mathbf{U}_N^H \mathbf{a}(\theta), \\ &= \mathbf{v}(\frac{1}{z})^T \mathbf{U}_N \mathbf{U}_N^H \mathbf{v}(z), \end{aligned} \tag{4.13}$$

for $|z| = 1$. If we define the matrix

$$\mathbf{G} = \mathbf{U}_N \mathbf{U}_N^H, \tag{4.14}$$

for $\mathbf{G} \in \mathbb{C}^{M \times M}$, then the null spectrum can be expanded into a polynomial in z,

$$d_i = \sum_{m_1, m_2}^{M} \mathbf{G}_{m_1, m_2}, \quad (m_1 - m_2) = i,$$

(4.15)

$$D(z) = d_{-(M-1)} z^{-(M-1)} + \cdots + d_{M-1} z^{M-1},$$

where d_i are the sums along the diagonals of $\mathbf{G}$. Some properties of $D(z)$, $z \in \mathbb{C}$, are as follows:

i. $d_i = d_{-i}^*$, because $\mathbf{G}$ is Hermitian by construction.

ii. As a result of (4.12), K root pairs appear near the unit circle (noise present), or on the unit circle (noise free) [2].

iii. If one root exists at $\tilde{z}$, another root will exist at $\frac{1}{\tilde{z}^*}$ because $D(z) = D(\frac{1}{z^*})$.

For root-MUSIC, the K roots inside the unit circle with largest magnitude, $|z|$, are taken as DOA estimates using the mapping of (4.7) [4]. These roots produce highly reliable estimates of the DOAs. When noise is present in the measurements, the accuracy of the DOA estimates is related to how well the true noise subspace was approximated by $\mathbf{U}_N$.

Note that $D(z)$ was derived only for z on the unit circle, but its roots located off the unit circle are used as DOA estimates. There is no physically meaningful reason behind this decision. Rather, it should be viewed as a useful mathematical trick. The polynomial expansion of $D(z)$ is especially useful because its roots can be calculated efficiently.

Figure 4.1 depicts an example null spectrum from half-wavelength spaced ULA measurements, which highlights points ii and iii. Even when the measurements are severely corrupted by noise, the null spectrum can be used to obtain good estimates of the DOA locations.

When $\mathbf{R}_{yy}$ is noise free, it is rank K and takes Toeplitz structure. Additionally, K (double) roots appear on the unit circle of its null spectrum. Those roots are the elements, z, of the Vandermonde decomposition of $\mathbf{R}_{yy}$, see (4.8). Thus the procedure of root-MUSIC finds the

z parameters of a Vandermonde decomposition. Because root-MUSIC works for covariance matrices corrupted by noise, it can be viewed as a method for approximating the z parameters of a 'noisy' Toeplitz matrix.

4.2.4 Gridless DOA for Uniform Linear Arrays

In gridless DOA estimation, the DOAs composing $\mathbf{Z}$, (4.1), are found by minimizing the atomic ℓ_0 norm of atoms defined by the manifold of the array steering matrix [18].

The noiseless signal contained in $\mathbf{Z}$ can be re-written as

$$\mathbf{Z} = \sum_{k=1}^{K} \mathbf{a}(\mathbf{r},\theta_k)\mathbf{x}_k^{\mathsf{H}} = \sum_{k=1}^{K} c_k \mathbf{a}(\mathbf{r},\theta_k)\mathbf{b}_k^{\mathsf{H}} \tag{4.16}$$

where $c_k = \|\mathbf{x}\|_2 > 0$, $\mathbf{b}_k = c_k^{-1}\mathbf{x}_k$, thus $\|\mathbf{b}_k\|_2 = 1$. We define the atomic set as

$$\mathcal{A} = \{\mathbf{a}(\mathbf{r},\theta_k,\mathbf{b}_k) = \mathbf{a}(\mathbf{r},\theta_k)\mathbf{b}_k^{\mathsf{H}}\}, \tag{4.17}$$

which can be thought of as the set of rank 1 matrices of constrained norm that can be constructed from the manifold $\mathbf{a}(\mathbf{r},\theta)$ over all values of θ. Expressing $\mathbf{Z}$ as a linear combination of K atoms in $\mathcal{A}$ brings us to the definition of the atomic ℓ_0 norm formulation of $\mathbf{Z}$,

$$\|\mathbf{Z}\|_{\mathcal{A},0} = \inf_{c_k,\theta_k,\mathbf{b}_k} \left\{ K : \mathbf{Z} = \sum_{k=1}^{K} c_k \mathbf{a}(\mathbf{r},\theta_k)\mathbf{b}_k^{\mathsf{H}} \right\}. \tag{4.18}$$

Gridless DOA is concerned with finding a solution to (4.18). Towards this goal, consider the matrix

$$\mathbf{S} = \sum_{k=1}^{K} c_k^2 \begin{bmatrix} \mathbf{a}(\mathbf{r},\theta_k) \\ \mathbf{b}_k \end{bmatrix} \begin{bmatrix} \mathbf{a}(\mathbf{r},\theta_k) \\ \mathbf{b}_k \end{bmatrix}^{\mathsf{H}} = \begin{bmatrix} \mathbf{T} & \mathbf{Z} \\ \mathbf{Z}^{\mathsf{H}} & \mathbf{Q} \end{bmatrix}, \tag{4.19}$$

where

$$\mathbf{T} = \mathbf{A}_s(\mathbf{r}, \theta)\mathbf{D}\mathbf{A}_s(\mathbf{r}, \theta)^{\mathsf{H}}, \tag{4.20}$$

$$\mathbf{Q} = \mathbf{X}^{\mathsf{H}}\mathbf{X}, \tag{4.21}$$

and $\mathbf{D} \in \mathbb{R}^{K \times K}$ is diagonal with elements c_k^2. By definition $\mathbf{S}$ is a positive semi-definite (PSD) matrix.

In the ULA case the array steering matrix is Vandermonde and $\mathbf{T} \in \mathcal{T}$. Theorem 6.2 of [18] tells us that the atomic ℓ_0 norm of (4.18) in the ULA case will be the optimal solution of the following rank constrained optimization problem,

$$\underset{\mathbf{T} \in \mathcal{T}, \mathbf{Q}}{\text{minimize}} \quad \text{rank}(\mathbf{T}), \quad \text{subject to} \quad \mathbf{S} \succeq 0. \tag{4.22}$$

Once the optimal $\mathbf{T}$ is found, the DOAs θ_k for $k = 1, \dots, K$ can be recovered through Vandermonde decomposition (or root-MUSIC) of $\mathbf{T}$. Thus (5.13) can be viewed as a means of estimating the full rank covariance matrix of a single measurement snapshot. This is possible because the covariance matrix has low rank Toeplitz structure.

State-of-the-art optimization solvers are only suitable for convex problems. In practice, the non-convex optimization problem of (5.13) is substituted for its convex relaxation [18],

$$\underset{\mathbf{T} \in \mathcal{T}, \mathbf{Q}}{\text{minimize}} \quad \text{Tr}(\mathbf{T}) + \text{Tr}(\mathbf{Q}), \quad \text{subject to} \quad \mathbf{S} \succeq 0. \tag{4.23}$$

When the matrix rank is substituted for the matrix trace the optimization of (5.13) is in the form of a semi-definite program (SDP), to which there are many available solvers [33]. The derivation of the popular alternating directions method of multipliers (ADMM) algorithm [34] to solve (5.15) is provided in App. 4.7.

4.3 Extension to Non-Uniform Array Geometries

We introduce a generalization of the Vandermonde matrix, which we call the *irregular Vandermonde matrix*. In the same way a Toeplitz matrix is constructed from Vandermonde components, we define an *irregular Toeplitz matrix* constructed from irregular Vandermonde components. It is then shown that irregular Toeplitz matrices can be decomposed back to their irregular Vandermonde components.

We deem this decomposition the *irregular Vandermonde decomposition* (IVD) because it can be interpreted as the Vandermonde decomposition of an irregularly sampled signal (i.e. the positions of the sensors act as sample locations of a spectrally sparse signal whose frequencies are related to the DOAs). Furthermore, the array steering matrix of a NUA has irregular Vandermonde structure. We propose an 'irregular' root-MUSIC algorithm, which is related to the IVD in the same way root-MUSIC is related to the Vandermonde decomposition.

The IVD is derived by carrying out the steps of the Vandermonde decomposition on the irregular Vandermonde matrix. Under this framework, the null spectrum no longer has polynomial structure and cannot be easily rooted. Regardless, the roots of interest are the $2K$ root pairs which lie on or near the unit circle. A simple method to recover the relevant information from these roots is presented, which does not resort to computationally expensive numerical methods.

The key difference between the Vandermonde decomposition and the IVD is an additional vector parameter involved in the IVD which specifies the sensor positions. For any vector of sensor positions there is a set of matrices akin to the Toeplitz set containing all matrices that can be decomposed exactly by the IVD. This set is used in Sec. 4.4 to extend gridless DOA to NUA measurements.

4.3.1 Irregular Vandermonde and Toeplitz Matrices

Consider an irregular Vandermonde matrix $\mathbb{C}^{M \times K}$ defined as [40],

$$\mathbf{W}(\gamma, z) = [z^{\gamma_1} \ldots z^{\gamma_M}]^\mathsf{T},$$
$$= [\mathbf{w}(\gamma, z_1) \ldots \mathbf{w}(\gamma, z_K)], \tag{4.24}$$

where γ_i is the ith element of a vector $\gamma \in \mathbb{R}^M$ and $z \in \mathbb{C}^K$, and $\mathbf{w}(\gamma, z) = [z^{\gamma_1} \ldots z^{\gamma_M}]^\mathsf{T}$.

In the context of DOA estimation, $\mathbf{A}_s(\mathbf{r}, \theta) = \mathbf{W}(\gamma, z)$, using the mapping

$$\gamma = \mathbf{r}, \quad z_k = e^{-j\pi \sin \theta_k}, \quad \theta_k = -\sin^{-1}\left(\frac{\angle z_k}{\pi}\right). \tag{4.25}$$

Notice that this is a generalization of the mapping presented in (4.5–4.7).

Following (4.8), we construct an irregular Toeplitz matrix from irregular Vandermonde matrices in the same way a Toeplitz matrix is constructed from Vandermonde matrices. Define $\mathcal{T}_\gamma$ as the irregular Toeplitz set for parameter vector γ,

$$\mathcal{T}_\gamma = \{\mathbf{T} : \mathbf{T} = \mathbf{W}(\gamma, z)\mathbf{D}\mathbf{W}(\gamma, z)^\mathsf{H}, |z| = 1\}, \tag{4.26}$$

where $\mathbf{D} \in \mathbb{R}^{K \times K}$ is a diagonal matrix with elements c_k^2. Each unique parameter vector, γ, is associated with an irregular Toeplitz set, $\mathcal{T}_\gamma$. The Toeplitz set is reached by any parameter vector corresponding to a ULA, $\gamma = \alpha[0, \ldots, M-1]^\mathsf{T} + \beta$.

The expected sample covariance matrix for NUA measurements with sensor positions $\mathbf{r} = \gamma$ is a diagonally loaded member of $\mathcal{T}_\gamma$,

$$\mathbb{E}[\mathbf{R}_{yy}] = \mathbf{A}_s(\mathbf{r}, \theta)\Sigma_X \mathbf{A}_s(\mathbf{r}, \theta)^\mathsf{H} + \Sigma_N$$
$$= \mathbf{W}(\gamma, z)\Sigma_X \mathbf{W}(\gamma, z)^\mathsf{H} + \sigma_N^2 \mathbf{I}. \tag{4.27}$$
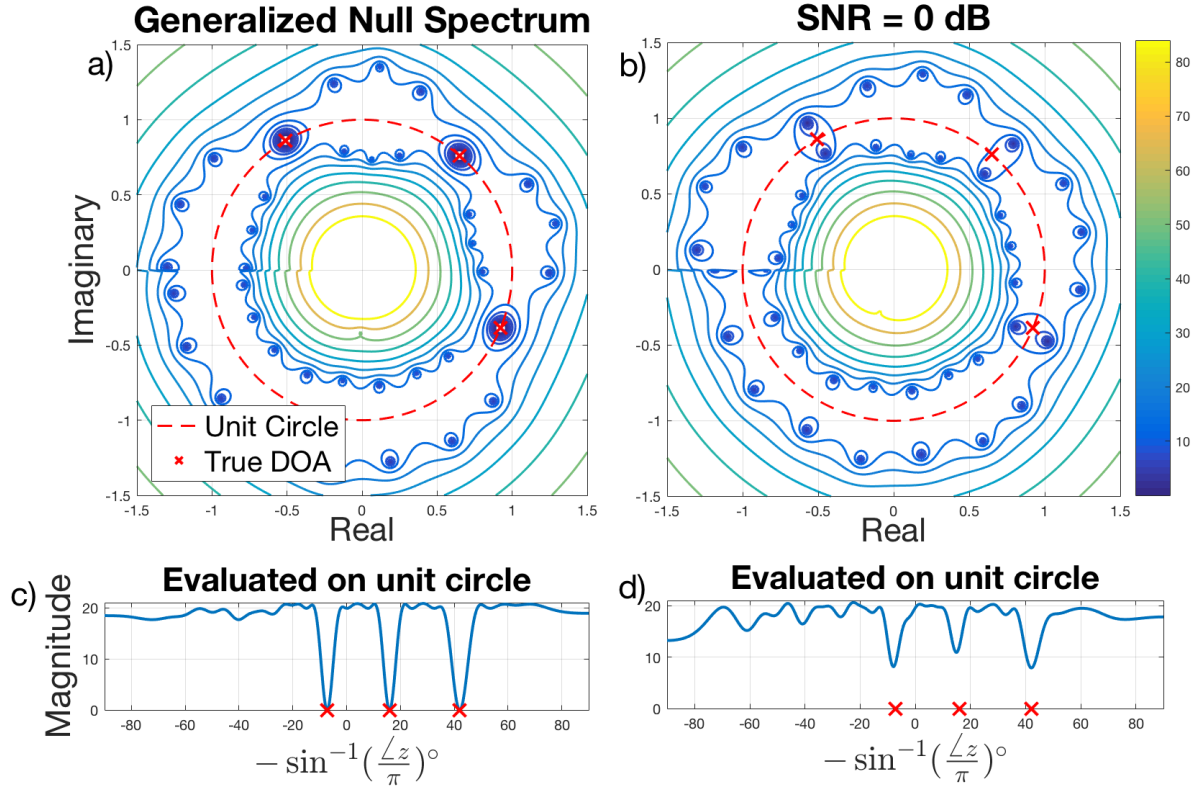
Figure 4.2: Irregular null spectrum, (4.29), for NUA measurements generated according to (4.1) using $M = 21$, $K = 3$, $L = 10$. DOAs located at $\theta = [-7.24, 15.96, 42.07]°$ (red x). a) Irregular null spectrum contour of noiseless measurements. Red dashed line marks the complex unit circle. b) Same as a) with added noise such that $\|\mathbf{Z}\|_F = \|\mathbf{N}\|_F$, see (4.1). c) Evaluation of a) on unit circle. d) Evaluation of b) on unit circle.

for Σ_X and Σ_N in (4.10). When the measurements are noiseless $\Sigma_N = \mathbf{0}$ and $\mathbf{R}_{yy} \in \mathcal{T}_{\boldsymbol{\gamma}}$.

4.3.2 Irregular Root-MUSIC and Vandermonde Decomposition

Consider the sample covariance matrix, $\mathbf{T} \in \mathbb{C}^{M \times M}$, from a NUA constructed as in (4.27). Following (4.13), the null spectrum of $\mathbf{T}$ is

$$\begin{aligned}
\tilde{D}(z) &= \|\mathbf{U}_N^{\mathsf{H}} \mathbf{a}(\mathbf{r}, \theta)\|_2^2 = \mathbf{a}(\mathbf{r}, \theta)^{\mathsf{H}} \mathbf{U}_N \mathbf{U}_N^{\mathsf{H}} \mathbf{a}(\mathbf{r}, \theta) \\
&= \mathbf{w}(\gamma, \frac{1}{z})^{\mathsf{T}} \mathbf{G} \mathbf{w}(\gamma, z),
\end{aligned}$$

(4.28)

for $\mathbf{r} = \gamma$ and $\mathbf{G}$ in (4.14). Because (4.28) is constructed from irregular Vandermonde matrices, we refer to it as the *irregular null spectrum*. The expansion of $\tilde{D}(z)$ is

$$\tilde{D}(z) = \sum_{m=1}^{M} \sum_{n=1}^{M} g_{m,n} z^{\gamma_m - \gamma_n}, \tag{4.29}$$

where $g_{m,n}$ is element (m,n) of $\mathbf{G}$. We treat the domain of $\tilde{D}(z)$ as though it were the set of complex numbers, despite deriving $\tilde{D}(z)$ only for z on the unit circle.

Figure 4.2 depicts an example irregular null spectrum, $\tilde{D}(z)$, from NUA measurements. The behavior of the irregular null spectrum is similar to that of the null spectrum from a half-wavelength spaced ULA in Fig. 4.1. Note that the irregular null spectrum has a discontinuity at $\angle z = \pi$, because for nearly all array geometries $\tilde{D}(z)|_{\angle z = \pi_+} \neq \tilde{D}(z)|_{\angle z = \pi_-}$.

To understand why this is true, consider that $\angle z = \pi_\pm$ corresponds to DOAs $\theta = \pm\frac{\pi}{2}$, (4.25). The discontinuity is due to the inequality of the NUA array manifold at the extreme values of θ. The half-wavelength spaced ULA is one of several exceptional array geometries which produce the same array pattern across the array for signals arriving at $\pm 90°$,

$$e^{-j\pi(r+\beta)\sin(\frac{\pi}{2})} = e^{-j\pi(r+\beta)\sin(-\frac{\pi}{2})}, \quad r \in \mathbb{Z}. \tag{4.30}$$

Properties i-iii from Sec. 4.2.3 hold for the irregular null spectrum, (the equivalent property i for the irregular null spectrum is $g_{m,n} = g_{n,m}^*$). Unlike (4.15), the irregular null spectrum no longer expands to a polynomial that can be easily rooted. Instead, the expansion of (4.29) is a non-linear equation for which there is no known closed form solution to obtain its roots.

We exploit the following two facts about $\tilde{D}(z)$:

1. The roots of interest are those that appear on or near the unit circle, as seen by (4.12).

2. Only the phase angle of the roots of interest are used to generate DOA estimates.

Thus the local minimums of $\tilde{D}(z)$ evaluated on the unit circle give DOA estimates with similar

accuracy as those given by the actual roots. $\tilde{D}(z)$ evaluated on the unit circle is the inverse of the MUSIC spectrum [41].

The arguments, z, producing the K smallest local minima of $\tilde{D}(z)$ are taken as the DOA estimates using (4.25). Because each root of $\tilde{D}(z)$ has a root pair on the same radial line (i.e. $\angle \tilde{z} = \angle \frac{1}{\tilde{z}^*}$), a saddle point is expected to lie on or near this radial line. These saddle points manifest as local minima of $\tilde{D}(z)$ evaluated over $|z| = 1$, and provide good estimates of the DOAs. An example is provided in Fig. 4.2.

When $\mathbf{T} \in \mathcal{T}_{\boldsymbol{\gamma}}$, all roots of interest are guaranteed to appear on the unit circle because $\mathbf{G} \perp \mathbf{W}(\gamma, z)$. Evaluating $\tilde{D}(z)$ on the unit circle yields all root locations, z, which perfectly reconstructs $\mathbf{W}(\gamma, z)$ from (4.26). The signal powers, $\mathbf{c} = [c_1^2 \ \dots \ c_K^2]^\mathsf{T}$ are found from,

$$\mathbf{c} = \text{diag}\left(\mathbf{W}^\dagger \mathbf{T}(\mathbf{W}^\dagger)^\mathsf{H}\right),$$

$$\mathbf{W}^\dagger = (\mathbf{W}^\mathsf{H}\mathbf{W})^{-1}\mathbf{W}^\mathsf{H},$$

(4.31)

where $\mathbf{D} = \text{diag}(\mathbf{c})$, and $\mathbf{W}(\gamma, z)$ has been shortened to $\mathbf{W}$. By this procedure it is possible to decompose an irregular Toeplitz matrix to irregular Vandermonde components. Pseudocode for the IVD algorithm is given in Sec. 4.3.4.

4.3.3 Irregular Toeplitz Structure

This section provides insight into the specific structure shared by all members of $\mathcal{T}_{\boldsymbol{\gamma}}$, similar to Toeplitz matrices. Consider a noiseless sample covariance matrix, this time constructed as an irregular Toeplitz matrix,

$$\mathbf{R}_{zz} = \mathbf{A}_s(\mathbf{r}, \theta)\Sigma_X \mathbf{A}_s(\mathbf{r}, \theta)^\mathsf{H} = \mathbf{W}(\gamma, z)\mathbf{D}\mathbf{W}(\gamma, z)^\mathsf{H},$$

(4.32)

where $\Sigma_X = \mathbf{D} = \mathrm{diag}(\mathbf{c})$, and (γ, z) is related to $(\mathbf{r}, \theta)$ by (4.25). Each element of $\mathbf{R}_{zz}$ can be written as,

$$(\mathbf{R}_{zz})_{m,n} = \sum_{k=1}^{K} c_k^2 z_k^{(\gamma_m - \gamma_n)}. \tag{4.33}$$

In the ULA case, $\gamma = \alpha[0, 1, \ldots, (M-1)]^T + \beta$, and it can be seen that $\gamma_m - \gamma_n$ will take the same value across each diagonal, producing the Toeplitz structure. In the NUA case element (m, n) of $\mathbf{R}_{zz}$ is the sum of K complex exponential functions sampled at element (m, n) of the Euclidean distance matrix of γ [35].

It can be shown that the irregular Toeplitz set for any γ is convex. Consider two matrices in $\mathcal{T}_{\gamma}$ composed from irregular Vandermonde matrices with parameters z_1 and z_2,

$$\mathbf{T}_1 = \mathbf{W}(\gamma, z_1)\mathbf{D}_1\mathbf{W}(\gamma, z_1)^H, \tag{4.34}$$

$$\mathbf{T}_2 = \mathbf{W}(\gamma, z_2)\mathbf{D}_2\mathbf{W}(\gamma, z_2)^H. \tag{4.35}$$

Then their convex combination is

$$\begin{aligned}
\lambda\mathbf{T}_1 + (1-\lambda)\mathbf{T}_2 = \\
\mathbf{W}\left(\gamma, [z_1\, z_2]\right)\begin{bmatrix} \lambda\mathbf{D}_1 & 0 \\ 0 & (1-\lambda)\mathbf{D}_2 \end{bmatrix}\mathbf{W}\left(\gamma, [z_1\, z_2]\right)^H,
\end{aligned} \tag{4.36}$$

for $0 \leq \lambda \leq 1$. The right hand side of (4.36) is a member of $\mathcal{T}_{\gamma}$ composed of irregular Vandermonde matrices with parameters $[z_1\, z_2]$.

4.3.4 IVD and Irregular Root-MUSIC

The IVD presents a computationally efficient extension of root-MUSIC to NUA measurements. We present pseudocode for the algorithms here.

The IVD takes as input the sensor positions, γ, the dimension of the noise subspace, K, and

---
Algorithm 1 : $(z, \mathbf{c}) = \texttt{IVD}(\mathbf{T}, \gamma, K)$

Require: $\mathbf{T} \in \mathbb{C}^{M \times M}, \ \gamma \in \mathbb{R}^M, \ K \in \mathbb{Z}$
  $[\mathbf{U}, \Sigma, \mathbf{V}] = \texttt{svd}(\mathbf{T})$
  $\mathbf{U}_N = \mathbf{U}(:, K+1:M)$
  $z = \texttt{find}(\texttt{argmin}(\tilde{D}(z)), |z| = 1), \ \ \text{see (4.29) and (4.42)}$
  $\mathbf{c} = \texttt{diag}\left(\mathbf{W}(\gamma, z)^\dagger \mathbf{T} (\mathbf{W}(\gamma, z)^\dagger)^\mathsf{H} \right)$

Algorithm 2 : $\hat{\theta} = \texttt{IrregularRootMusic}(\mathbf{Y}, \gamma, K)$

Require: $\mathbf{Y} \in \mathbb{C}^{M \times L}, \ \gamma \in \mathbb{R}^M, \ K \in \mathbb{Z}, \ L \geq K$
  $\mathbf{T} = \frac{1}{L} \mathbf{Y} \mathbf{Y}^\mathsf{H}$
  $(z, \mathbf{c}) = \texttt{IVD}(\mathbf{T}, \gamma, K)$
  $\hat{\theta} = -\texttt{asin}(\texttt{angle}(z)/\pi)$
---

the matrix to be decomposed, $\mathbf{T}$. The outputs are the harmonics, z, and the diagonal matrix, $\mathbf{D}$. If $\mathbf{T}$ is a sample covariance matrix, then the harmonics are related to the DOAs by (4.25). In Algorithm 1, $\texttt{svd}()$ is the singular value decomposition of a matrix and $\texttt{find}(\texttt{argmin}(\tilde{D}(z)), |z| = 1)$ outputs the values of z producing the K smallest local minima of $\tilde{D}(z)$ on the unit circle. For simulations in Sec. 4.5, a gridded search over $10M$ evenly spaced points on the unit circle was used to find intervals containing minima, then the estimated minima locations were iteratively refined using a golden section search algorithm [42].

The IVD allows for the extension of root-MUSIC to array measurements taken at a non-uniform array. We deem this *irregular root-MUSIC*, which is presented in Algorithm 2. Irregular root-MUSIC takes the measurements, $\mathbf{Y}$, as inputs and outputs the DOAs. The number of measurement snapshots must be at least as large as the number of DOAs present ($L \geq K$) or it will be impossible to accurately estimate the noise subspace and the resulting DOA estimates will be incorrect. The sensor positions, γ, input to Algorithm 2 are in units of half-wavelengths.

4.4 Gridless DOA for Non-Uniform Arrays

The irregular Toeplitz set enables gridless DOA to be generalized to the NUA case. In this section we modify the optimization for gridless DOA to extend its use to measurements from NUAs, then propose an alternating projections (AP) based algorithm for solving said optimization. The AP solution is based on similar AP based algorithms that were recently examined in the context of CCS [36, 37, 38].

4.4.1 Extension to Non-Uniform Arrays

To extend gridless DOA to NUAs, the optimization of (5.13) is modified such that the optimal matrix belongs to $\mathcal{T}_{\boldsymbol{\gamma}}$ for $\gamma = \mathbf{r}$,

$$\underset{\mathbf{T} \in \mathcal{T}_{\boldsymbol{\gamma}}, \mathbf{Q}}{\text{minimize}} \quad \text{rank}\big(\mathbf{T}\big), \quad \text{subject to } \mathbf{S} \succeq 0. \tag{4.37}$$

The optimization of (4.37) can be further simplified if we define the rank constrained irregular Toeplitz set as

$$\mathcal{T}_{\boldsymbol{\gamma}}^{K} = \{\mathbf{T} : \mathbf{T} \in \mathcal{T}_{\boldsymbol{\gamma}}, \text{ rank}(\mathbf{T}) \leq K\}. \tag{4.38}$$

This is the set of rank K matrices that are members of $\mathcal{T}_{\boldsymbol{\gamma}}$. The NUA gridless DOA problem then simplifies to,

$$\underset{\mathbf{T} \in \mathcal{T}_{\boldsymbol{\gamma}}^{K}, \mathbf{Q}}{\text{minimize}} \quad \|\mathbf{S}\|_F \quad \text{subject to } \mathbf{S} \succeq 0. \tag{4.39}$$

Once the optimal $\mathbf{T}$ is known, the IVD (Algorithm 1) can be applied to recover the DOAs and source powers.

4.4.2 Important Projections NUA Gridless DOA

Before it is possible to formulate the optimization of (4.39) using AP, we define some important projections.

Projection to the Toeplitz Set

For ULA measurements, the projection onto $\mathcal{T}_{\boldsymbol{\gamma}}^K$ can be replaced by a projection onto $\mathcal{T}$. The projection of a matrix, $\mathbf{T} \in \mathbb{C}^{M \times M}$, to the Toeplitz set is [43],

$$P_{\mathcal{T}}(\mathbf{T}) = \mathcal{T}(\mathbf{u})$$

$$u_i = \frac{1}{2(M-i)} \sum_{j=1}^{(M-i)} \mathbf{T}_{j,j+i-1} + \mathbf{T}^*_{j+i-1,j}. \tag{4.40}$$

In words, the Toeplitz projection, $P_{\mathcal{T}}(\mathbf{T})$, is achieved by replacing the elements along each diagonal with their mean.

Projection to the Irregular Toeplitz Set

Recall the definition of $\mathcal{T}_{\boldsymbol{\gamma}}^K$ from (4.38). Consider a matrix $\mathbf{T} \notin \mathcal{T}_{\boldsymbol{\gamma}}^K$. The goal is to project $\mathbf{T}$ onto $\mathcal{T}_{\boldsymbol{\gamma}}^K$,

$$P_{\mathcal{T}_{\boldsymbol{\gamma}}^K}(\mathbf{T}) = \mathbf{W}(\gamma, \tilde{z})\mathbf{D}\mathbf{W}(\gamma, \tilde{z})^{\mathsf{H}}, \tag{4.41}$$

for some set of parameters $\tilde{z} \in \mathbb{C}^K$. A projection onto $\mathcal{T}_{\boldsymbol{\gamma}}^K$ can be achieved by constructing an irregular Toeplitz matrix using approximate parameters $\tilde{z}$ retrieved from the local minima of the irregular null spectrum evaluated on the unit circle,

$$\tilde{z} = \arg \min_{|z|=1}^{k} \tilde{D}(z), \quad k = 1, \ldots, K, \tag{4.42}$$

where $\arg\min_z^k$ denotes the argument, z, which produces the kth smallest local minima.

Algorithm 3 : $\tilde{\mathbf{T}} = \mathrm{P}_{\mathcal{T}_{\gamma}}(\mathbf{T}, \gamma, K)$

Require: $\mathbf{T} \in \mathbb{C}^{M \times M}$, $\gamma \in \mathbb{R}^{M}$, $K \in \mathbb{Z}$, $M \geq K \geq 1$
$\quad (z, \mathbf{c}) = \mathtt{IVD}(\mathbf{T}, \gamma, K)$
$\quad \tilde{\mathbf{T}} = \mathbf{W}(\gamma, z) \mathrm{diag}(\mathbf{c}) \mathbf{W}(\gamma, z)^{\mathsf{H}}$

Because $\mathbf{T} \notin \mathcal{T}_{\gamma}$, the roots of its null spectrum are not on the unit circle. Instead, approximate z parameters are estimated from the irregular null spectrum. Once $\tilde{z}$ is known, the corresponding $\mathbf{D}$ matrix containing the signal powers is estimated (4.31). Pseudocode for projection onto $\mathcal{T}_{\gamma}^{K}$ is given in Algorithm 3. The algorithm involves computing the IVD for a given matrix and reconstructing the matrix from the IVD outputs. The structure of $\tilde{\mathbf{T}}$ makes clear that $\tilde{\mathbf{T}} \in \mathcal{T}_{\gamma}^{K}$.

Projection to the Positive Semi-Definite Cone

The set of PSD matrices is

$$\mathcal{S}_{\succeq 0} = \{\mathbf{M} \in \mathbb{C}^{N \times N} : \lambda_{i} \in \mathbb{R}, \ \lambda_{i} \geq 0, \quad \forall i\}, \tag{4.43}$$

where λ_{i} is the ith eigenvalue of $\mathbf{M}$, with corresponding eigen vector $\mathbf{e}_{i}$. The projection onto $\mathcal{S}_{\succeq 0}$ is [44]

$$P_{\mathcal{S}_{\succeq 0}}(\mathbf{M}) = \sum_{i=1}^{N} \max(0, \lambda_{i}) \mathbf{e}_{i} \mathbf{e}_{i}^{\mathsf{H}}. \tag{4.44}$$

The set $\mathcal{S}_{\succeq 0}$ forms a cone and is convex [34].

4.4.3 Alternating Projections for NUA Gridless DOA

The AP algorithm is an optimization scheme which has found notable success when applied to the structured low rank matrix completion problem [36, 45, 46, 37]. The basic concept of AP is that a solution located at the intersection of two or more sets can be found by iteratively projecting an estimate between the sets. The algorithm is guaranteed to converge when all sets

are convex, but convergence is not guaranteed when one or more sets is non-convex (i.e. the rank constrained set) [47]. AP can be used to solve (4.39).

Define the set

$$
\mathcal{S}_{(\mathcal{T}_\gamma^K, \mathbf{Y})} = \left\{ \mathbf{M} : \mathbf{M} = \begin{bmatrix} \mathbf{T} & \mathbf{Y} \\ \mathbf{Y}^\mathsf{H} & \mathbf{Q} \end{bmatrix}, \mathbf{T} \in \mathcal{T}_\gamma^K \right\}, \tag{4.45}
$$

where γ, $\mathbf{Y} \in \mathbb{C}^{M \times L}$, and K are known and $\mathbf{Q} \in \mathbb{C}^{L \times L}$ is a free matrix. Here γ is the array element position vector, and $\mathbf{Y}$ is the measurement matrix. The projection onto $\mathcal{S}_{(\mathcal{T}_\gamma^K, \mathbf{Y})}$ is performed as

$$
\mathbf{M} = \begin{bmatrix} \mathbf{B} & \mathbf{C} \\ \mathbf{D} & \mathbf{Q} \end{bmatrix},
$$

$$
P_{\mathcal{S}_{(\mathcal{T}_\gamma^K, \mathbf{Y})}}(\mathbf{M}) = \begin{bmatrix} P_{\mathcal{T}_\gamma^K}(\mathbf{B}) & \mathbf{Y} \\ \mathbf{Y}^\mathsf{H} & \mathbf{Q} \end{bmatrix}. \tag{4.46}
$$

In words, the projection is achieved by replacing the top left submatrix of $\mathbf{M}$ with its projection to $\mathcal{T}_\gamma^K$ (Algorithm 3), and replacing the corner submatrices with $\mathbf{Y}$ and $\mathbf{Y}^\mathsf{H}$.

The AP algorithm for solving (4.39) is achieved by projecting an initial estimate between $\mathcal{S}_{\succeq 0}$ and $\mathcal{S}_{(\mathcal{T}_\gamma^K, \mathbf{Y})}$,

$$
\begin{aligned}
\mathbf{H}^{(i+1)} &= P_{\mathcal{S}_{\succeq 0}}(\mathbf{L}^{(i)}), \\
\mathbf{L}^{(i+1)} &= P_{\mathcal{S}_{(\mathcal{T}_\gamma^K, \mathbf{Y})}}(\mathbf{H}^{(i+1)}),
\end{aligned} \tag{4.47}
$$

for arbitrary initial estimate $\mathbf{L}^{(0)} \in \mathbb{C}^{(M+L) \times (M+L)}$. Upon convergence, the IVD of the $M \times M$ upper right submatrix of $\mathbf{S}$ retrieves the DOAs. Pseudocode for AP based gridless DOA algorithm is given in Algorithm 4. We deem this algorithm, "*AP gridless*".

AP gridless requires prior knowledge of K. There have been many works on source
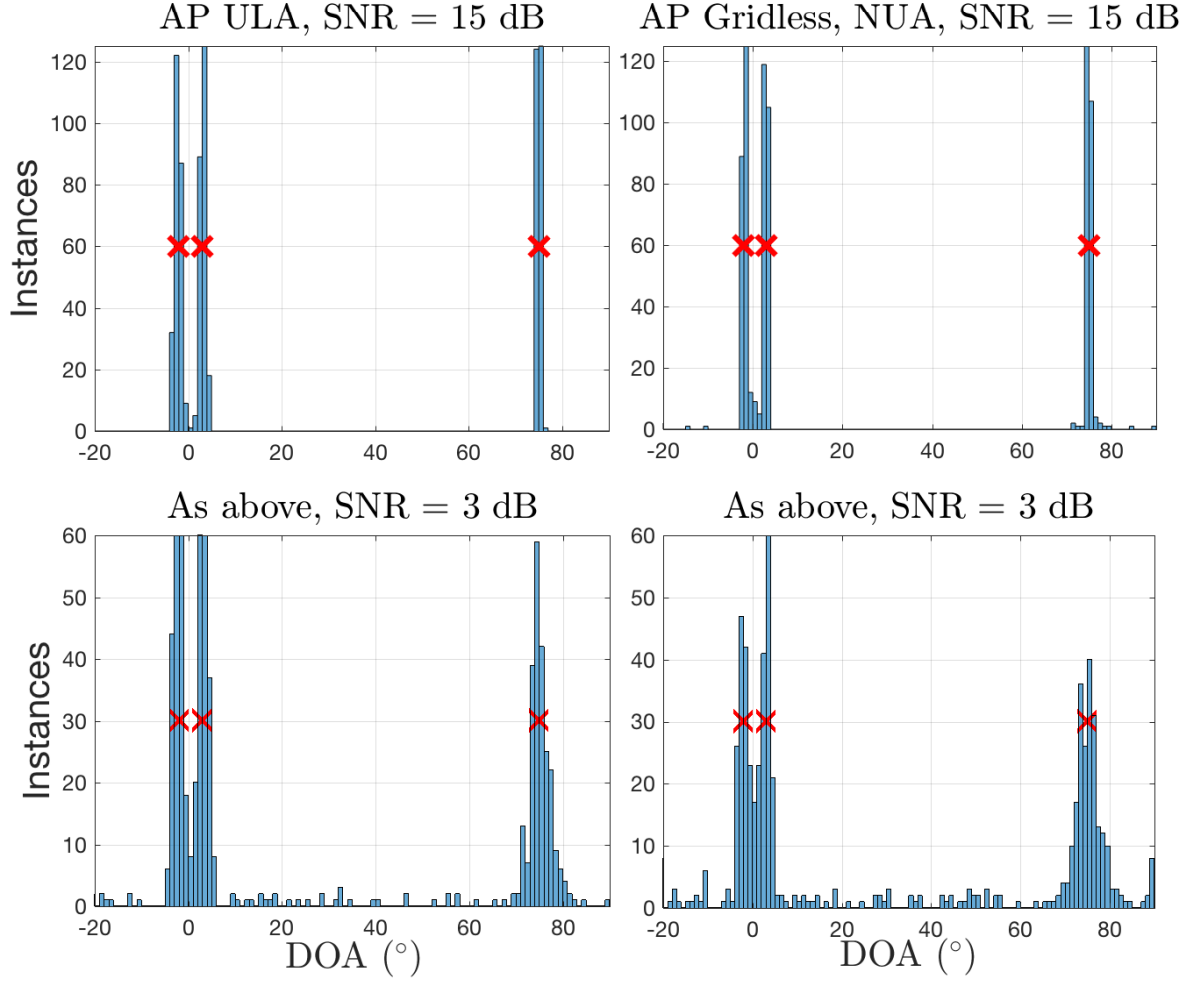
Figure 4.3: Histogram of recovered DOAs for AP ULA (Algorithm 5) and AP gridless (Algorithm 4), $M = 20$, $L = 1$, $\sigma_s = 5$, $\theta = [-2, 3, 75]°$ (red x). 250 trials per histogram. Left- AP ULA. Right- AP Gridless (NUA).

number estimation [48, 49] which can be used to estimate K. Alternatively, AP gridless can be applied for a range of K, and the sparsest solution which adequately reconstructs the measurements can be taken as optimal.

The algorithm is called "*AP ULA*" when the irregular Toeplitz projection, $P_{\mathcal{T}_\gamma^K}$ (Algorithm 3), is replaced with a Toeplitz projection, $P_{\mathcal{T}}$ (4.40). AP ULA can only be used for measurements from a ULA, and is given in Algorithm 5.

Algorithm 4 : $\hat{\theta} = \texttt{AP\_Gridless}(\mathbf{Y}, \gamma, K)$

  $[M, L] = \texttt{size}(\mathbf{Y})$

Require: $\gamma \in \mathbb{R}^M, K \in \mathbb{Z}, 0 < K < M$

  $\mathbf{L}^{(0)} = [\mathbf{0}, \mathbf{Y}; \mathbf{Y}^\mathsf{H}, \mathbf{I}]$

  for $i = 1 : \texttt{max\_iterations}$ **do**

    $\mathbf{H}^{(i)} = P_{\mathcal{S}_{\succeq 0}}(\mathbf{L}^{(i-1)})$

    $\mathbf{T} = \mathbf{H}^{(i)}(1 : M, 1 : M)$

    $\mathbf{Q} = \mathbf{H}^{(i)}(M + 1 : \texttt{end}, M + 1 : \texttt{end})$

    $\mathbf{L}^{(i)} = [\mathrm{P}_{\mathcal{T}_\gamma}(\mathbf{T}, \gamma, K), \mathbf{Y}; \mathbf{Y}^\mathsf{H}, \mathbf{Q}]$

    if $\|\mathbf{L}^{(i)} - \mathbf{L}^{(i-1)}\|_F \leq \texttt{1e} - 7$ **then**

      `break`

    end if

  end for

  $\mathbf{T} = \mathbf{L}(1 : M, 1 : M)$

  $[z, \sim] = \texttt{IVD}(\mathbf{T}, \gamma, K)$

  $\hat{\theta} = -\texttt{asin}(\texttt{angle}(z)/\pi)$

4.4.4   Initialization and Convergence

The AP algorithm is guaranteed to converge at a linear rate when applied between two closed convex sets [50], however the set of matrices with rank $\leq K$ is non-convex, (rather, it is quasi-convex [35]). It is not known if AP will converge when applied between a convex set and the rank constrained set. By construction, $\mathcal{T}_\gamma^K$ is the intersection between $\mathcal{T}_\gamma$ and the rank constrained set, thus it is also non-convex and convergence remains an open question.

Progress towards a convergence proof was achieved in [51, Theorem 3.2] and can be summarized as it applies to (4.47) as follows:

Theorem: *Let* $\mathbf{L}^{(i)}, \mathbf{H}^{(i)}$ *be generated according to (4.47), and* $\mathbf{L}^{(0)} \in \mathcal{S}_{(\mathcal{T}_\gamma^K, \mathbf{Y})}$ *then*

1. Either $\|\mathbf{L}^{(i)} - \mathbf{H}^{(i)}\|_F^2 \to \infty$ as $i \to \infty$ or $\|\mathbf{L}^{(i)} - \mathbf{H}^{(i)}\|_F^2$ converges to 0.

2. If $\mathbf{L}^{(0)}$ is sufficiently close to the global minimizer of (4.39), $\mathbf{L}^{(0)}$ converges to the global minimum.

Note that Theorem 1 does not guarantee the point of convergence will be the global

---

Algorithm 5 : $\hat{\theta} = \texttt{AP\_ULA}(\mathbf{Y}, \gamma, K)$

$[M, L] = \texttt{size}(\mathbf{Y})$
Require: $\gamma \in \mathbb{R}^M, K \in \mathbb{Z}, 0 < K < M$
  $\mathbf{L}^{(0)} = [\mathbf{0}, \mathbf{Y}; \mathbf{Y}^H, \mathbf{I}]$
  for $i = 1 : \texttt{max\_iterations}$ **do**
    $\mathbf{H}^{(i)} = P_{\mathcal{S}_{\geq 0}}(\mathbf{L}^{(i-1)})$
    $\mathbf{T} = \mathbf{H}^{(i)}(1 : M, 1 : M)$
    $\mathbf{Q} = \mathbf{H}^{(i)}(M+1 : \texttt{end}, M+1 : \texttt{end})$
    $\mathbf{L}^{(i)} = [P_{\mathcal{T}}(\mathbf{T}), \mathbf{Y}; \mathbf{Y}^H, \mathbf{Q}]$
    if $\|\mathbf{L}^{(i)} - \mathbf{L}^{(i-1)}\|_F \leq \texttt{1e}-7$ **then**
      `break`
    end if
  end for
  $\mathbf{T} = \mathbf{L}(1 : M, 1 : M)$
  $[z, \sim] = \texttt{IVD}(\mathbf{T}, \gamma, K)$
  $\hat{\theta} = -\texttt{asin}(\texttt{angle}(z)/\pi)$

---

minimizer unless the initialization point is sufficiently nearby the optimal solution. In general, it can only be assumed the convergence point will be a local minimum of the optimization function.

All simulations in Sec. 4.5 were performed using the initialization,

$$\mathbf{L}^{(0)} = \begin{bmatrix} \mathbf{0} & \mathbf{Y} \\ \mathbf{Y}^H & \mathbf{I} \end{bmatrix}, \tag{4.48}$$

which was always observed to converge to a critical point rather than diverging. Because it remains unknown if the initialization point will bring the algorithm to a local or global minimum, all further analysis on the accuracy of AP for gridless DOA is left to numerical simulation performed in Sec. 4.5.

4.5 Simulation

AP gridless (4.47) (Algorithm 4), and AP ULA (4.40) (Algorithm 5) were applied to solve the gridless DOA problem (4.39) for simulated measurements modeled by (4.1). For each

simulation, K randomly generated DOAs were chosen such that the minimum angular separation was $\frac{1}{M}$ for DOAs randomly drawn between $[0, 1)$ and scaled to $[-90°, 90°)$. Signals contained in the K rows of $\mathbf{X}$ were generated as complex values with uniformly distributed phase. The signal from each DOA was given random amplitude σ_s^x, $x \in \mathcal{U}(0, 1)$ to model sources with different powers. Noise, $\mathbf{N}$, was drawn from a complex Gaussian distribution with mean zero and variance $\mathbf{I}$, then scaled to fit the desired signal to noise ratio (SNR) determined by

$$\text{SNR} = 10\log_{10}\left(\frac{\|\mathbf{Z}\|_F^2}{\|\mathbf{N}\|_F^2}\right). \tag{4.49}$$

Array measurements were simulated using an array of M sensors distributed as both a ULA and NUA. The NUA geometry was generated by adding random offsets drawn from a uniform distribution between $[-.5, .5)$ (in units of half-wavelengths) to each sensor position. No restriction was placed on how nearby two NUA elements could be.

All simulations were performed for ULA and NUA. In the ULA case, AP gridless and AP ULA were both applied. It was assumed K was known for each simulation. AP gridless and AP ULA were considered converged when $\|\mathbf{L}^{(i)} - \mathbf{L}^{(i-1)}\|_F \leq 10^{-7}$, or terminated after $10K$ iterations.

The accuracy of the solution was gauged by the root mean square error (RMSE) between true, θ_k, and recovered, $\hat{\theta}_k$, DOAs defined as

$$\text{RMSE} = \sqrt{\mathbb{E}\left[\frac{1}{K}\sum_{k=1}^{K}(\theta_k - \hat{\theta}_k)^2\right]}. \tag{4.50}$$

A maximum MSE threshold of $10°$ was used to provide an even error penalty for simulations resulting in incorrect DOA estimates.

Sparse Bayesian learning (SBL) [52, 53, 54, 55, 56], and least absolute shrinkage and selector operator (LASSO) [57, 58, 5, 7] methods were given a dictionary of the array manifold

with 1° separation between entries (180 total). The LASSO tuning parameter was selected such that the solution was K sparse (which requires knowledge of $\|\mathbf{N}\|_F$ [59]). The ADMM algorithm was applied to ULA measurements using parameters $\tau = .01$, and $\rho = 1$ (see App. 4.7).

Example results from AP ULA and AP gridless are detailed in Fig. 4.3. The AP ULA algorithm never misclassifies a DOA when the measurement SNR is high (Fig. 4.3, top left), and lowering the measurement SNR results in few misclassifications (Fig. 4.3, bottom left). In contrast, there are some NUA geometries which cause AP gridless to misclassify a DOA, even for high SNR (Fig. 4.3, top right). The rate of misclassification for the low SNR NUA case is slightly higher than that of the ULA case (Fig. 4.3, bottom right).

Gridless DOA excels over gridded methods in the high SNR, low snapshot case. This is due to quantization error from grid mismatch limiting the maximum accuracy of gridded techniques. Figure 4.4 compares gridless and gridded algorithms for high SNR, single snapshot measurements when all algorithms are run to convergence. The best achievable accuracy for a gridded technique using 1° DOA separation is RMSE = .25°. In the ULA case (Fig. 4.4, top), all gridless techniques achieve accuracy proportional to SNR. ADMM is not as precise due to limitations in parameter tuning. In the NUA case (Fig. 4.4, bottom) AP gridless maintains excellent performance.

The performance of each algorithm in lower SNR scenarios is detailed in Fig. 4.5. In the ULA case, AP gridless and AP ULA achieve similar performance to ADMM, particularly in the single snapshot case (Fig. 4.5, top left), indicating that convex relaxation is unnecessary to solve rank minimization problems. AP gridless and AP ULA perform slightly worse than ADMM for low SNR multi-snapshot measurements (Fig. 4.5, bottom left), suggesting that ADMM is more robust to noise. AP gridless is superior to gridded techniques for NUA measurements (Fig. 4.5, top and bottom right), except in low SNR scenarios where LASSO can attain similar performance. Irregular root MUSIC (Algorithm 2) attains near identical performance to AP gridless in the multiple snapshot NUA case (Fig. 4.5, bottom right), for less computational cost.

Performance of the algorithms versus array elements, M, is given in Fig. 4.6. AP Gridless and ADMM are superior in the ULA case (Fig. 4.6, top left), as gridded methods are limited in accuracy by grid resolution. For NUAs, AP gridless and irregular root-MUSIC are superior for the same reason. Root-MUSIC and irregular root-MUSIC attain equal performance to AP gridless and ADMM in the multi-snapshot case (Fig. 4.6, bottom left and right) for lower computational complexity. This is also shown by Fig. 4.7, which compares each method vs. number of snapshots, L. Once the number of snapshots is greater than the number of sources ($L \geq K$), there is no benefit to choosing a gridless technique because root-MUSIC and irregular root-MUSIC attain the same performance as gridless methods for reduced computational cost.

To get an indication of the high resolution capability of each algorithm, Fig. 4.8 compares AP gridless and AP ULA to conventional beamforming (CBF) and root-MUSIC for noiseless measurements with 2 DOAs at $\pm\theta°$. For the single snapshot case (Fig. 4.8, top), AP gridless has difficulty resolving nearby DOAs while ADMM and AP ULA have outstanding performance. The difference is that ADMM and AP ULA use projection to $\mathcal{T}$ in place of projection to $\mathcal{T}_{\boldsymbol{\gamma}}^K$.

$P_{\mathcal{T}_{\boldsymbol{\gamma}}^K}$ (4.41), (Algorithm 3) is fundamentally different than $P_{\mathcal{T}}$ (4.40). $P_{\mathcal{T}}$ outputs the nearest Toeplitz matrix in Frobenius norm to its input (orthogonal projection), which is generally a full rank Toeplitz matrix. In contrast, $P_{\mathcal{T}_{\boldsymbol{\gamma}}^K}$ outputs a rank K matrix which is not necessarily the orthogonal projection to $\mathcal{T}_{\boldsymbol{\gamma}}^K$. This is because $P_{\mathcal{T}_{\boldsymbol{\gamma}}^K}$ is estimated by reconstructing an irregular Toeplitz matrix using z parameters given by the local minima of $\tilde{D}(z)|_{|z|=1}$, rather than the phase angle of the roots of $\tilde{D}(z)$. Roots of $\tilde{D}(z)$ which are nearby in phase angle sometimes do not produce unique local minima of $\tilde{D}(z)|_{|z|=1}$, resulting in suboptimal z parameter estimates. This is only an issue when the DOAs are poorly separated and the measurements do not give a precise estimate of the noise subspace ($L < K$).

The same problem exists in the multiple snapshot ($L \geq K$) coherent sources case (Fig. 4.8, middle). Because the sources are coherent, the noise subspace still cannot be well estimated and AP gridless fails to resolve nearby DOAs until they are sufficiently separated.

When the sources are made incoherent (Fig. 4.8, bottom), the noise subspace can be estimated precisely, and AP gridless, root-MUSIC, and irregular root-MUSIC are exact. In contrast, ADMM and AP ULA are not as precise because $P_{\mathcal{T}}$ does not project to a specifically rank K solution, resulting in 'noisy' DOA estimates.

The computational bottleneck of AP gridless is the projection to the irregular Toeplitz set, $P_{\mathcal{T}_{\boldsymbol{\gamma}}^{K}}$, where a spectral search over $\tilde{D}(z)|_{|z|=1}$ is executed. In contrast, the AP ULA and ADMM algorithms use the relatively efficient projection to the Toeplitz set, $P_{\mathcal{T}}$ (4.40), and are limited by the eigen-decomposition of the $\mathbf{S}$ matrix in its projection to the positive semi-definite cone, $P_{S \succeq 0}$. Both algorithms are relatively fast, having runtime under one second on a regular CPU for problems with $(M + L) < 100$.

4.6 Conclusion

The problem of gridless direction of arrival (DOA) estimation for non-uniform array (NUA) geometries was considered. Towards this goal, the irregular Vandermonde decomposition (IVD) was introduced, which is a generalization of the Vandermonde decomposition for irregularly sampled signals, such as those sampled from a NUA. From the perspective of the IVD, any covariance matrix can be seen as an irregular Toeplitz matrix, and can be decomposed back into its irregular Vandermonde components. The decomposition can be used to extend gridless DOA to NUAs, as well as extending the larger continuous compressed sensing (CCS) problem to irregularly sampled signals. The decomposition also extends root-MUSIC to NUAs.

An intuitive non-convex method of solving gridless DOA for NUAs based on the alternative projections (AP) algorithm was proposed. The proposed algorithm was named AP gridless. Simulation on uniform linear array (ULA) measurements found AP gridless attains similar performance to its convex counterpart, ADMM. For NUAs, ADMM cannot be generalized, and only AP gridless applies. AP gridless was found to be robust to noise, high resolution, and

has superior performance compared to grid based techniques for high SNR.

4.7   Appendix: ADMM for gridless DOA

Here the alternating directions method of multipliers (ADMM) formulation of gridless DOA is detailed as it applies to multiple snapshot ULA measurements. A review of ADMM is given in [60]. Other sources which provide details on ADMM specifically for gridless DOA are [18, 61, 62, 63, 22].

Start with the rank minimization problem of (5.13). Because the the rank constraint is non-convex the problem must be cast to its convex relaxation before ADMM is applicable,

$$
\begin{aligned}
\min_{\mathbf{Q},\mathbf{S},\hat{\mathbf{Y}},\mathbf{u}} \quad & \frac{1}{2}\|\hat{\mathbf{Y}}-\mathbf{Y}\|_2^2 + \frac{\tau}{2}\Big(\mathrm{Tr}(\mathbf{Q})+\mathrm{Tr}(\mathcal{T}(\mathbf{u}))\Big) \\
\text{subject to} \quad & \mathbf{S}=\begin{bmatrix} \mathcal{T}(\mathbf{u}) & \hat{\mathbf{Y}} \\ \hat{\mathbf{Y}}^{\mathsf{H}} & \mathbf{Q} \end{bmatrix}, \quad \mathbf{S}\succeq 0,
\end{aligned}
\tag{A- 4.1}
$$

where $\mathbf{Y}\in\mathbb{C}^{M\times L}$ is the measurement matrix, $\mathcal{T}(\mathbf{u})\in\mathbb{C}^{M\times M}$ is the Toeplitz matrix whose first column is $\mathbf{u}$, $\mathbf{Q}\in\mathbb{C}^{L\times L}$, and τ is a user defined parameter.

Next, the augmented Lagrangian is formed by collecting the constraints into the optimization function [61, 62],

$$
\mathcal{L}_{\rho}(\mathbf{Q},\mathbf{S},\hat{\mathbf{Y}},\Lambda,\mathbf{u}) = \frac{1}{2}\|\hat{\mathbf{Y}}-\mathbf{Y}\|_2^2 + \frac{\tau}{2}\Big(\mathrm{Tr}(\mathbf{Q})+\mathrm{Tr}(\mathcal{T}(\mathbf{u}))\Big) +
$$
$$
\Big\langle \Lambda, \mathbf{S}-\begin{bmatrix} \mathcal{T}(\mathbf{u}) & \hat{\mathbf{Y}} \\ \hat{\mathbf{Y}}^{\mathsf{H}} & \mathbf{Q} \end{bmatrix}\Big\rangle + \frac{\rho}{2}\Big\|\mathbf{S}-\begin{bmatrix} \mathcal{T}(\mathbf{u}) & \hat{\mathbf{Y}} \\ \hat{\mathbf{Y}}^{\mathsf{H}} & \mathbf{Q} \end{bmatrix}\Big\|_F^2, \quad \text{(A- 4.2)}
$$

where ρ is a user defined parameter and $\langle .,. \rangle$ is the matrix inner product, and Λ is the Lagrange multiplier variable. ADMM is performed by iteratively optimizing (A- 4.2) over each variable

independent of the the other variables. The update steps at iteration i are [61, 62],

$$(\mathbf{Q}^{(i+1)}, \mathbf{u}^{(i+1)}, \hat{\mathbf{Y}}^{(i+1)}) \leftarrow \arg \min_{\mathbf{Q}, \hat{\mathbf{Y}}, \mathbf{u}} \mathcal{L}_\rho(\mathbf{Q}, \mathbf{S}^{(i)}, \hat{\mathbf{Y}}, \Lambda^{(i)}, \mathbf{u}), \qquad \text{(A- 4.3)}$$

$$\mathbf{S}^{(i+1)} \leftarrow \arg \min_{\mathbf{S} \succeq 0} \mathcal{L}_\rho(\mathbf{Q}^{(i+1)}, \mathbf{S}, \hat{\mathbf{Y}}^{(i+1)}, \Lambda^{(i)}, \mathbf{u}^{(i+1)}), \qquad \text{(A- 4.4)}$$

$$\Lambda^{(i+1)} \leftarrow \Lambda^{(i)} + \rho \left(\mathbf{S}^{(i+1)} - \begin{bmatrix} \mathcal{T}(\mathbf{u}^{(i+1)}) & \hat{\mathbf{Y}}^{(i+1)} \\ \hat{\mathbf{Y}}^{(i+1)\mathsf{H}} & \mathbf{Q}^{(i+1)} \end{bmatrix} \right). \qquad \text{(A- 4.5)}$$

The update steps for $\mathbf{Q}$, $\mathbf{u}$, and $\hat{\mathbf{Y}}$ are computable in closed form. First define the partitions

$$\mathbf{S}^{(i)} = \begin{bmatrix} \mathbf{S}_{\mathcal{T}} & \mathbf{S}_{\mathbf{Y}} \\ \mathbf{S}_{\mathbf{Y}^{\mathsf{H}}} & \mathbf{S}_{\mathbf{Q}} \end{bmatrix} \quad \text{and} \quad \Lambda^{(i)} = \begin{bmatrix} \Lambda_{\mathcal{T}} & \Lambda_{\mathbf{Y}} \\ \Lambda_{\mathbf{Y}^{\mathsf{H}}} & \Lambda_{\mathbf{Q}} \end{bmatrix}, \qquad \text{(A- 4.6)}$$

where the dimensions of each partition are the dimensions of $\mathcal{T}$, $\mathbf{Y}$, and $\mathbf{Q}$. The update steps are [61, 62],

$$\mathbf{Q}^{(i+1)} = \frac{1}{2}\mathbf{S}_{\mathbf{Q}}^{(i)} + \frac{1}{2}(\mathbf{S}_{\mathbf{Q}}^{(i)})^{\mathsf{H}} + \frac{1}{\rho}\left(\Lambda_{\mathbf{Q}}^{(i)} - \frac{\tau}{2}\mathbf{I}\right), \qquad \text{(A- 4.7)}$$

$$\mathbf{u}^{(i+1)} = \mathcal{T}^{-1}\left(\mathbf{S}_{\mathcal{T}}^{(i)} + \frac{1}{\rho}\Lambda_{\mathcal{T}}^{(i)}\right) - \frac{\tau}{2\rho}\mathbf{e}_1, \qquad \text{(A- 4.8)}$$

$$\hat{\mathbf{Y}}^{(i+1)} = \frac{1}{2\rho + 1}\left(\mathbf{Y} + \rho\mathbf{S}_{\mathbf{Y}}^{(i)} + \rho\mathbf{S}_{\mathbf{Y}^{\mathsf{H}}}^{(i)} + 2\Lambda_{\mathbf{Y}}^{(i)}\right), \qquad \text{(A- 4.9)}$$

where $\mathcal{T}^{-1}$ is a function giving the first column of the nearest Toeplitz matrix to its input (4.40), and $\mathbf{e}_1$ is the canonical basis vector in M dimensional space, $[1\,0 \ldots 0]^{\mathsf{T}}$.

Finally, the $\mathbf{S}$ update is a projection onto the positive semidefinite cone (4.44),

$$\mathbf{S}^{(i+1)} = P_{S \succeq 0}\left(\mathbf{S}^{(i)} - \begin{bmatrix} \mathcal{T}(\mathbf{u}^{(i+1)}) & \hat{\mathbf{Y}}^{(i+1)} \\ \hat{\mathbf{Y}}^{(i+1)\mathsf{H}} & \mathbf{Q}^{(i+1)} \end{bmatrix} + \frac{1}{\rho}\Lambda^{(i)} \right). \qquad \text{(A- 4.10)}$$

ADMM is known to converge at a linear rate for convex problems [60].

4.8   Acknowledgments
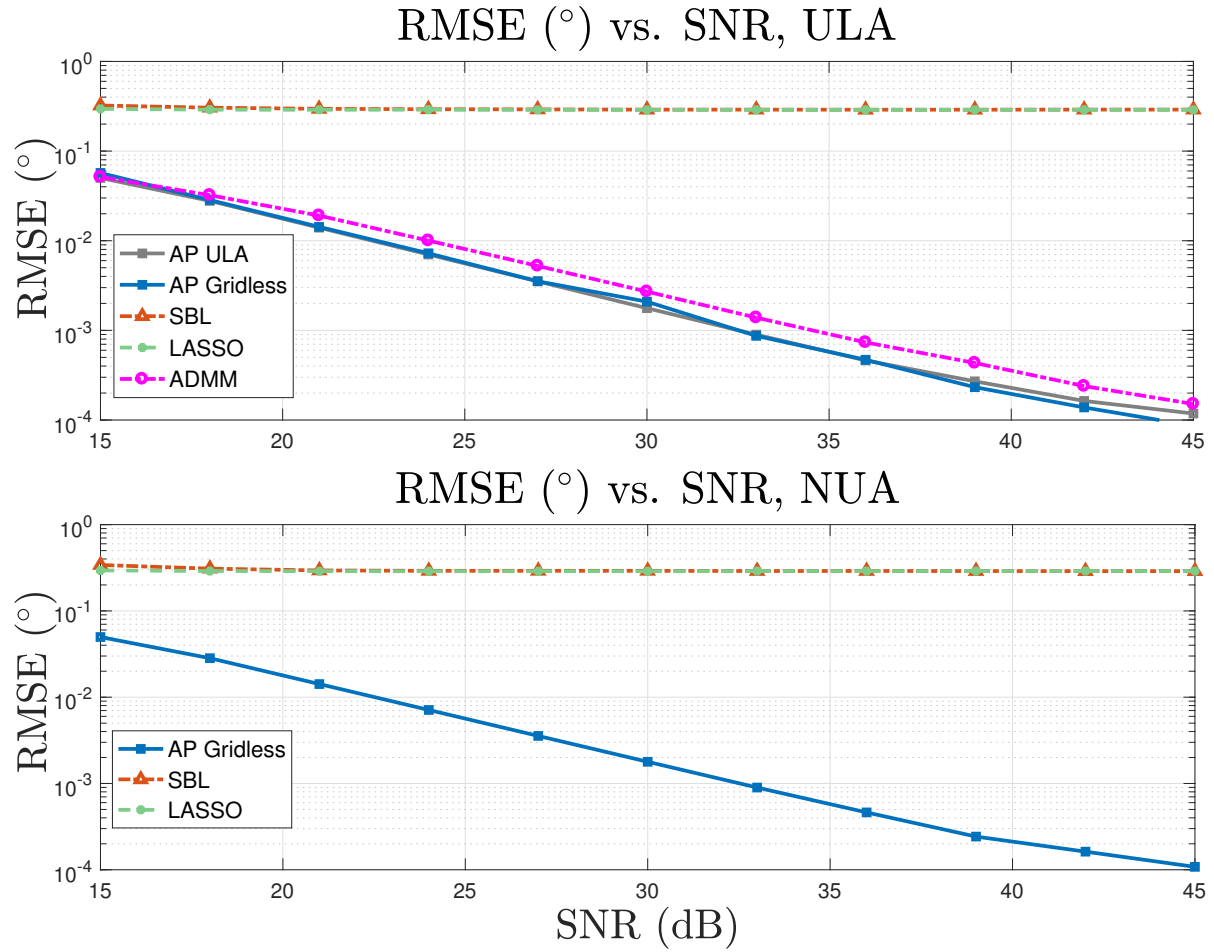
Figure 4.4: RMSE vs. SNR on high SNR single snapshot measurements using AP Gridless (Algorithm 4), AP ULA (Algorithm 5), ADMM (App. 4.7, $\tau = 10^{-5}$), SBL, and LASSO. $M = 20, K = 3, L = 1, \sigma_s = 5$. Each point represents average over 250 trials. All algorithms run to convergence.
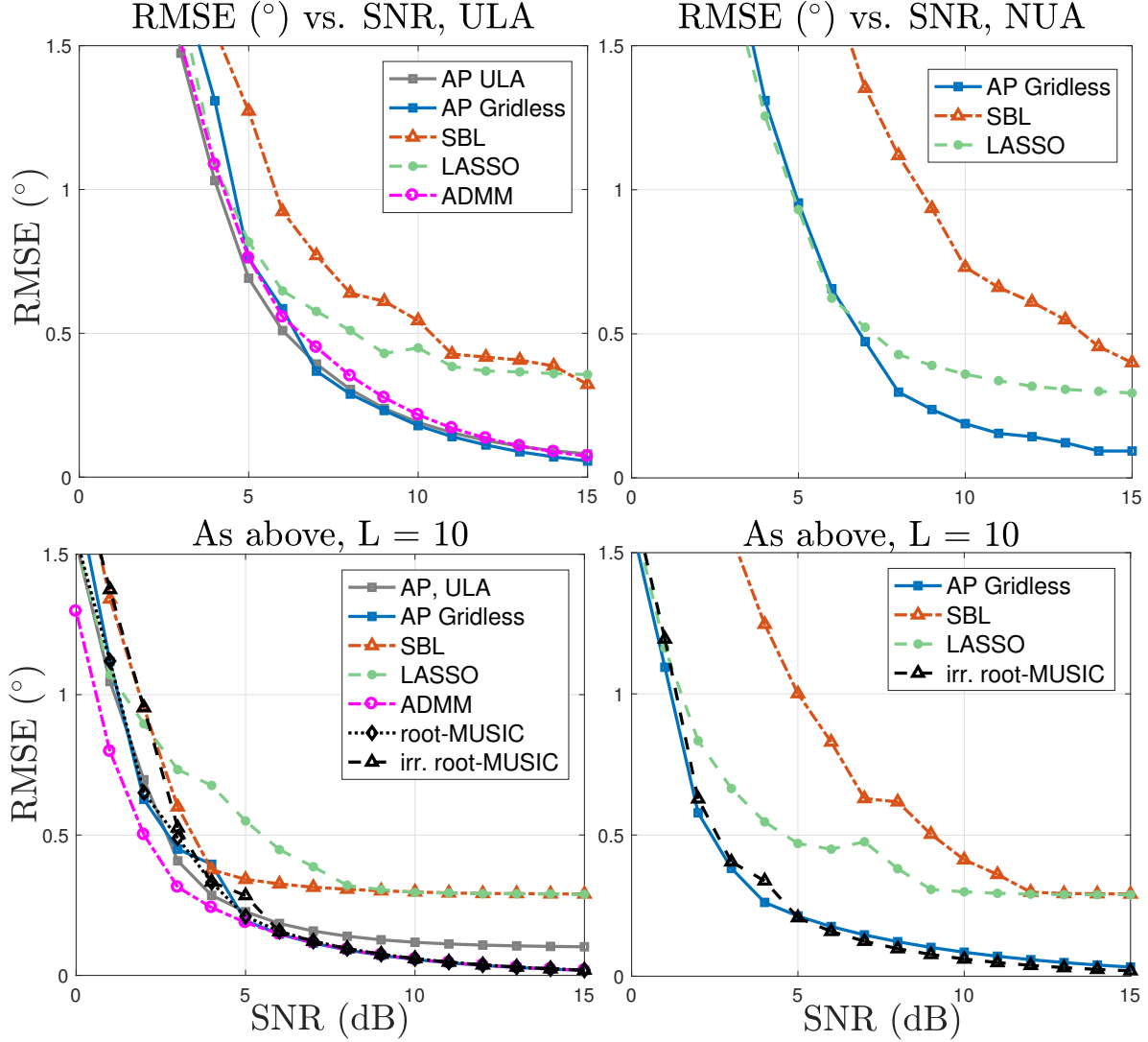
Figure 4.5: RMSE vs. SNR for AP gridless (Algorithm 4), AP ULA (Algorithm 5), ADMM (App. 4.7), SBL, LASSO, root-MUSIC, and irregular root-MUSIC (Algorithm 2), $M = 20$, $K = 3$, $\sigma_s = 5$. Each point represents 250 trials. Top left- ULA measurements, $L = 1$. Top right- NUA measurements, $L = 1$. Bottom left- ULA measurements, $L = 10$. Bottom right- NUA measurements, $L = 10$.
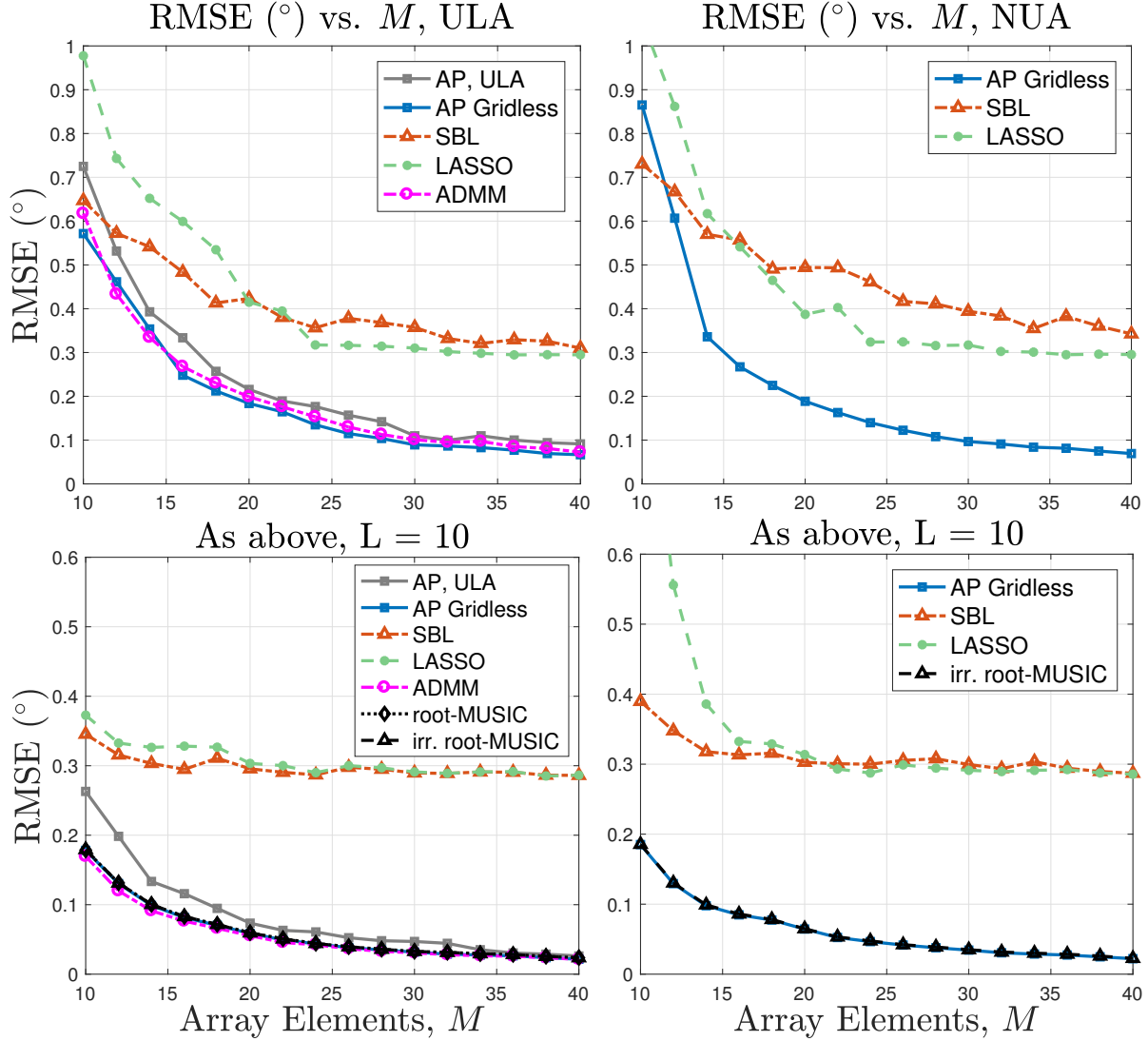
Figure 4.6: RMSE vs. M for AP gridless (Algorithm 4), AP ULA (Algorithm 5), ADMM 4.7, SBL, LASSO, root-MUSIC, and irregular root-MUSIC (Algorithm 2), SNR = 10 dB, $K = 3$, $\sigma_s = 5$. Each point represents 250 trials. Top left- ULA measurements, $L = 1$. Top right- NUA measurements, $L = 1$. Bottom left- ULA measurements, $L = 10$. Bottom right- NUA measurements, $L = 10$.
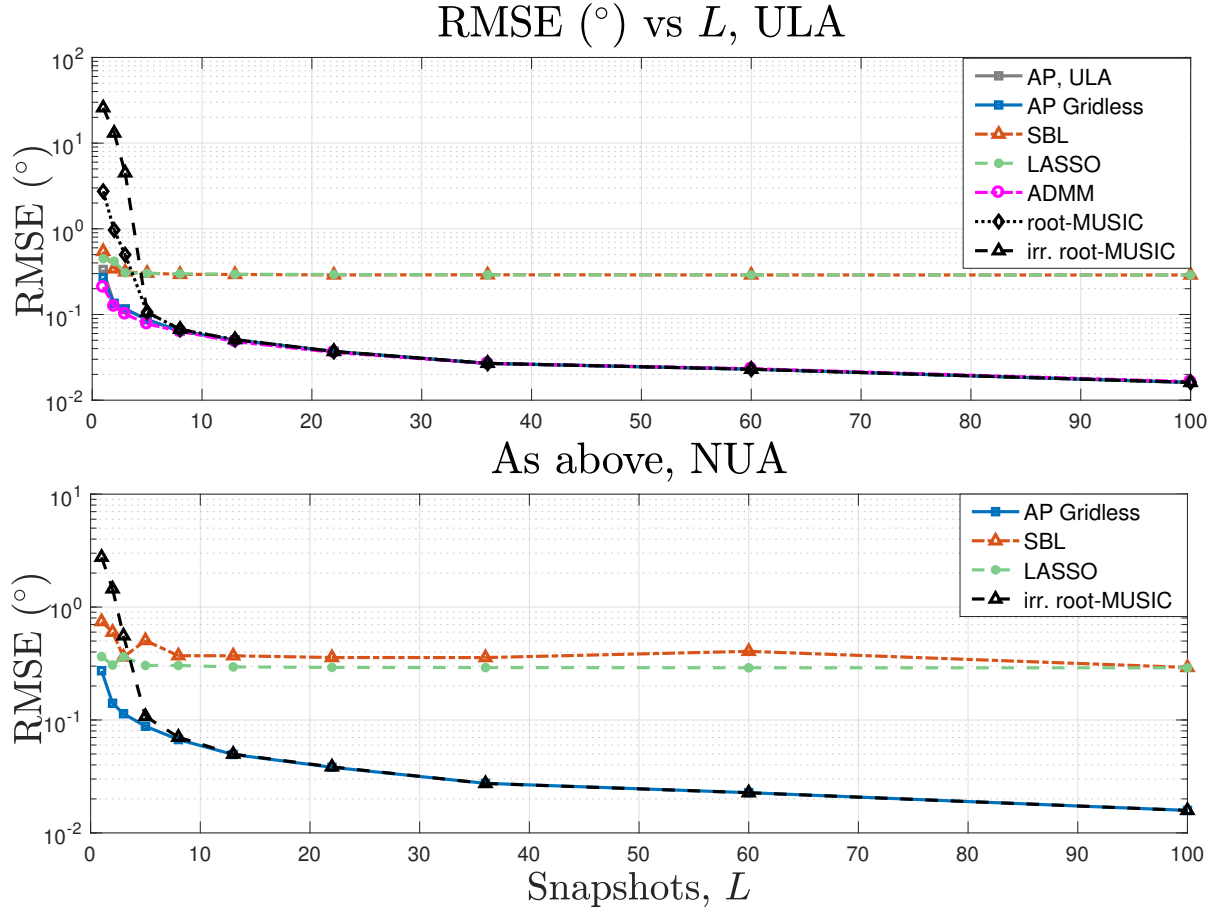
Figure 4.7: RMSE vs. L for AP gridless (Algorithm 4), AP ULA (Algorithm 5), ADMM (App. 4.7), SBL, LASSO, root-MUSIC, and irregular root-MUSIC (Algorithm 2), $M = 20$, $K = 3$, $\sigma_s = 5$, SNR = 10 dB. Each point represents 250 trials. Top- ULA measurements. Bottom-NUA measurements.
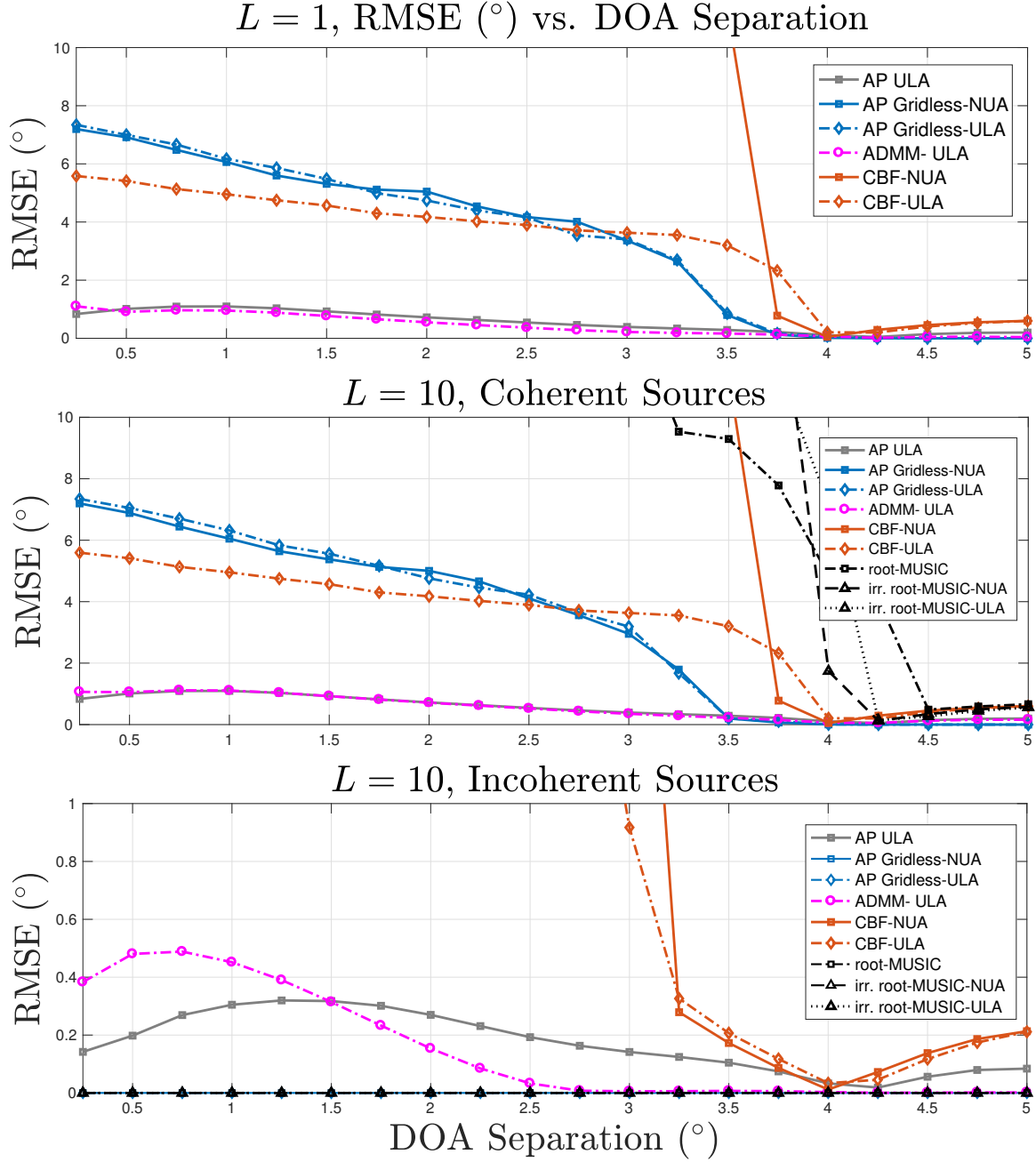
Figure 4.8: RMSE vs. DOA separation of conventional (Bartlett) beamformer (CBF), AP gridless (Algorithm 4), AP ULA (Algorithm 5), ADMM (App. 4.7), root-MUSIC, and irregular root-MUSIC (Algorithm 2) on noiseless simulated ULA and NUA measurements using $K = 2$ equal amplitude sources at $\pm\theta°$, $M = 20$. No maximum MSE penalty, each point represents 250 trials. Top- $L = 1$. Middle- $L = 10$, coherent sources. Bottom- $L = 10$, incoherent sources.

Bibliography

[1] A. Barabell, "Improving the resolution performance of eigenstructure-based direction-finding algorithms," in *ICASSP'83. IEEE Inter. Conf. Acoustics, Speech, and Sig. Proc.* Citeseer, 1983, vol. 8, pp. 336–339.

[2] B.D. Rao and K.V. Hari, "Performance analysis of root-MUSIC," *IEEE Trans. Acoust., Speech, Signal Process.*, vol. 37, no. 12, pp. 1939–1949, 1989.

[3] M. Pesavento, A.B. Gershman, and M. Haardt, "Unitary root-music with a real-valued eigendecomposition: A theoretical and experimental performance study," *IEEE Trans. Sig. Proc.*, vol. 48, no. 5, pp. 1306–1314, 2000.

[4] H.L. Van Trees, *Optimum array processing: Part IV of detection, estimation, and modulation theory*, John Wiley & Sons, 2004.

[5] A. Xenaki, P. Gerstoft, and K. Mosegaard, "Compressive beamforming," *J. Acoust. Soc. Am.*, vol. 136, no. 1, pp. 260–271, 2014.

[6] A. Xenaki and P. Gerstoft, "Grid-free compressive beamforming," *J. Acoust. Soc. Am.*, vol. 137, no. 4, pp. 1923–1935, 2015.

[7] P. Gerstoft, A. Xenaki, and C.F. Mecklenbräuker, "Multiple and single snapshot compressive beamforming," *J. Acoust. Soc. Am.*, vol. 138, no. 4, pp. 2003–2014, 2015.

[8] Y. Chi, L.L. Scharf, A. Pezeshki, and A.R. Calderbank, "Sensitivity to basis mismatch in compressed sensing," *IEEE Trans. Signal. Process.*, vol. 59, no. 5, pp. 2182–2195, 2011.

[9] G. Tang, B.N. Bhaskar, P. Shah, and B. Recht, "Compressed sensing off the grid," *IEEE Trans. Inf. Theory*, vol. 59, no. 11, pp. 7465–7490, 2013.

[10] E.J. Candès and C. Fernandez-Granda, "Towards a mathematical theory of super-resolution," *Commun. Pure Appl. Math.*, vol. 67, no. 6, pp. 906–956, 2014.

[11] Z. Yang and L. Xie, "On gridless sparse methods for line spectral estimation from complete and incomplete data," *IEEE Trans. Signal Process.*, vol. 63, no. 12, pp. 3139–3153, 2015.

[12] Y. Park, P. Gerstoft, and W. Seong, "Grid-free compressive mode extraction," *J. Acoust. Soc. Am.*, vol. 145, no. 3, pp. 1427–1442, 2019.

[13] M. Fazel, T.K. Pong, D. Sun, and P. Tseng, "Hankel matrix rank minimization with applications to system identification and realization," *SIAM J. Matrix Anal. and App.*, vol. 34, no. 3, pp. 946–977, 2013.

[14] Y. Chi and Y. Chen, "Compressive two-dimensional harmonic retrieval via atomic norm minimization," *IEEE Trans. Signal Process.*, vol. 63, no. 4, pp. 1030–1042, 2014.

[15] Z. Yang and L. Xie, "Exact joint sparse frequency recovery via optimization methods," *IEEE Trans. Sig. Proc.*, vol. 64, no. 19, pp. 5145–5157, 2016.

[16] Z. Yang and L. Xie, "Enhancing sparsity and resolution via reweighted atomic norm minimization," *IEEE Transactions on Signal Processing*, vol. 64, no. 4, pp. 995–1006, 2015.

[17] Y. Chen and Y. Chi, "Robust spectral compressed sensing via structured matrix completion," *IEEE Trans. Inf. Theory*, vol. 60, no. 10, pp. 6576–6601, 2014.

[18] Z. Yang, J. Li, P. Stoica, and L. Xie, "Chapter 11 - sparse methods for direction-of-arrival estimation," in *Academic Press Library in Signal Processing, Volume 7*, R. Chellappa and S. Theodoridis, Eds., pp. 509 – 581. Academic Press, 2018.

[19] V.F. Pisarenko, "The retrieval of harmonics from a covariance function," *Geophys. J. Int.*, vol. 33, no. 3, pp. 347–366, 1973.

[20] Z. Yang, L. Xie, and P. Stoica, "Vandermonde decomposition of multilevel toeplitz matrices with application to multidimensional super-resolution," *IEEE Trans. on Info. Theory*, vol. 62, no. 6, pp. 3685–3701, 2016.

[21] S. Semper, F. Roemer, T. Hotz, and G. Del Galdo, "Grid-free direction-of-arrival estimation with compressed sensing and arbitrary antenna arrays," in *IEEE ICASSP 2018*. IEEE, 2018, pp. 3251–3255.

[22] S. Semper and F. Römer, "ADMM for ND line spectral estimation using grid-free compressive sensing from multiple measurements with applications to DOA estimation," in *ICASSP*. IEEE, 2019, pp. 4130–4134.

[23] A.G. Raj and J.H. McClellan, "Super-resolution DOA estimation for arbitrary array geometries using a single noisy snapshot," in *ICASSP*. IEEE, 2019, pp. 4145–4149.

[24] M. Rubsamen and A.B. Gershman, "Direction-of-arrival estimation for nonuniform sensor arrays: from manifold separation to fourier domain music methods," *IEEE Trans. Signal Process.*, vol. 57, no. 2, pp. 588–599, 2008.

[25] B. Friedlander and A.J. Weiss, "Direction finding using spatial smoothing with interpolated arrays," *IEEE Trans. on Aero. and Electric. Systems*, vol. 28, no. 2, pp. 574–587, 1992.

[26] B. Friedlander, "The root-MUSIC algorithm for direction finding with interpolated arrays," *Sig. Process.*, vol. 30, no. 1, pp. 15–29, 1993.

[27] M.A. Doran, E. Doron, and A.J. Weiss, "Coherent wide-band processing for arbitrary array geometry," *IEEE Trans. Signal Process.*, vol. 41, no. 1, pp. 414, 1993.

[28] A.J. Weiss, B. Friedlander, and P. Stoica, "Direction-of-arrival estimation using mode with interpolated arrays," *IEEE Trans. Signal Process.*, vol. 43, no. 1, pp. 296–300, 1995.

[29] Alex B. Gershman and J.F. Bohme, "A note on most favorable array geometries for DOA estimation and array interpolation," *IEEE Sig. Process. Letters*, vol. 4, no. 8, pp. 232–235, 1997.

[30] P. Hyberg, M. Jansson, and B. Ottersten, "Array interpolation and bias reduction," *IEEE Trans. Signal Process.*, vol. 52, no. 10, pp. 2711–2720, 2004.

[31] F. Belloni, A. Richter, and V. Koivunen, "DoA estimation via manifold separation for arbitrary array structures," *IEEE Trans. Signal Process.*, vol. 55, no. 10, pp. 4800–4810, 2007.

[32] Y. Chi, Y.M. Lu, and Y. Chen, "Nonconvex optimization meets low-rank matrix factorization: An overview," *IEEE Trans. Signal Process.*, vol. 67, no. 20, pp. 5239–5269, 2019.

[33] M. Grant, S. Boyd, and Y. Ye, "CVX: Matlab software for disciplined convex programming," 2008.

[34] S. Boyd and L. Vandenberghe, *Convex optimization*, Cambridge University Press, 2004.

[35] J. Dattorro, *Convex optimization and Euclidean distance geometry*, Meboo Publish, 2010.

[36] L. Condat and A. Hirabayashi, "Cadzow denoising upgraded: A new projection method for the recovery of dirac pulses from noisy linear measurements," *Sampling Theory in Signal and Image Processing*, vol. 14, no. 1, pp. 17–47, 2015.

[37] M. Cho, J.F. Cai, S. Liu, Y.C. Eldar, and W. Xu, "Fast alternating projected gradient descent algorithms for recovering spectrally sparse signals," in *ICASSP*. IEEE, 2016, pp. 4638–4642.

[38] S. Liu, *Projected Wirtinger gradient descent for spectral compressed sensing*, Ph.D. thesis, University of Iowa, 2017.

[39] T.K. Moon and W.C. Stirling, *Mathematical methods and algorithms for signal processing*, vol. 1, Prentice hall Upper Saddle River, NJ, 2000.

[40] J. Demmel and P. Koev, "The accurate and efficient solution of a totally positive generalized Vandermonde linear system," *SIAM J. Matrix Anal. and App.*, vol. 27, no. 1, pp. 142–152, 2005.

[41] R. Schmidt, "Multiple emitter location and signal parameter estimation," *IEEE Trans. Antennas. Prop.*, vol. 34, no. 3, pp. 276–280, 1986.

[42] G.E. Forsythe, M.A. Malcolm, and C.B. Moler, *Computer methods for mathematical computations*, vol. 259, Prentice-Hall Englewood Cliffs, NJ, 1977.

[43] M.G. Eberle and M.C. Maciel, "Finding the closest Toeplitz matrix," *J. Comp. & Applied Mathe.*, vol. 22, no. 1, pp. 1–18, 2003.

[44] S. Boyd and J. Dattorro, "Alternating projections," *EE392, Stanford University*, 2003.

[45] T. Cai and A. Zhang, "ROP: Matrix recovery via rank-one projections," *Ann. Stat.*, vol. 43, no. 1, pp. 102–138, 2015.

[46] E.J. Candes, X. Li, and M. Soltanolkotabi, "Phase retrieval via Wirtinger flow: Theory and algorithms," *IEEE Transactions on Information Theory*, vol. 61, no. 4, pp. 1985–2007, 2015.

[47] M.T. Chu, R.E. Funderlic, and R.J. Plemmons, "Structured low rank approximation," *Linear Algebra Appl.*, vol. 366, pp. 157–172, 2003.

[48] S. Aouada, A.M. Zoubir, and C.M. See, "A comparative study on source number detection," in *Sig. Proc. App., 2003. Proceedings. Seventh International Symposium on*. IEEE, 2003, vol. 1, pp. 173–176.

[49] K. Han and A. Nehorai, "Improved source number detection and direction estimation with nested arrays and ULAs using jackknifing," *IEEE Trans. Sig. Proc.*, vol. 61, no. 23, pp. 6118–6128, 2013.

[50] H.H. Bauschke and J.M. Borwein, "On the convergence of von-Neumann's alternating projection algorithm for two sets," *Set-Valued Analysis*, vol. 1, no. 2, pp. 185–212, 1993.

[51] H. Attouch, J. Bolte, P. Redont, and A. Soubeyran, "Proximal alternating minimization and projection methods for nonconvex problems: An approach based on the Kurdyka–Lojasiewicz inequality," *Math. Oper. Res.*, vol. 35, no. 2, pp. 438–457, 2010.

[52] D.P. Wipf and B.D. Rao, "Sparse Bayesian learning for basis selection," *IEEE Trans. Signal Process.*, vol. 52, no. 8, pp. 2153–2164, 2004.

[53] Z. Yang, L. Xie, and C. Zhang, "Off-grid direction of arrival estimation using sparse Bayesian inference," *IEEE Trans. Sig. Proc.*, vol. 61, no. 1, pp. 38–43, 2012.

[54] P. Gerstoft, C.F. Mecklenbräuker, A. Xenaki, and S. Nannuru, "Multisnapshot sparse Bayesian learning for DOA," *IEEE Sig. Process. Letters*, vol. 23, no. 10, pp. 1469–1473, 2016.

[55] K.L. Gemba, S. Nannuru, P. Gerstoft, and W.S. Hodgkiss, "Multi-frequency sparse Bayesian learning for robust matched field processing," *J. Acoust. Soc. Am.*, vol. 141, no. 5, pp. 3411–3420, 2017.

[56] K.L. Gemba, S. Nannuru, and P. Gerstoft, "Robust ocean acoustic localization with sparse Bayesian learning," *IEEE J. Sel. Topics Signal Process.*, vol. 13, no. 1, pp. 49–60, 2019.

[57] R. Tibshirani, "Regression shrinkage and selection via the LASSO," *J. Royal Stat. Soc. B.*, pp. 267–288, 1996.

[58] G.F. Edelmann and C.F. Gaumond, "Beamforming using compressive sensing," *J. Acoust. Soc. Am.*, vol. 130, no. 4, pp. 232–237, 2011.

[59] D. Malioutov, M. Cetin, and A.S. Willsky, "A sparse signal reconstruction perspective for source localization with sensor arrays," *IEEE Trans. Signal Process.*, vol. 53, no. 8, pp. 3010–3022, 2005.

[60] S. Boyd, N. Parikh, E. Chu, B. Peleato, J. Eckstein, et al., "Distributed optimization and statistical learning via the alternating direction method of multipliers," *Found. Trends. Mach. Learning*, vol. 3, no. 1, pp. 1–122, 2011.

[61] B.N. Bhaskar, G. Tang, and B. Recht, "Atomic norm denoising with applications to line spectral estimation," *arXiv preprint arXiv:1204.0562*, 2012.

[62] Y. Li and Y. Chi, "Off-the-grid line spectrum denoising and estimation with multiple measurement vectors," *arXiv preprint arXiv:1408.2242*, 2014.

[63] Y. Yang, Z. Chu, and G. Ping, "Two-dimensional multiple-snapshot grid-free compressive beamforming using alternating direction method of multipliers," *Shock and Vibration*, pp. 524–540, 2020.

Chapter 5

Phase Coherent Electromagnetic Measurements in a Refractive Environment

Phase coherent measurements of the pilot tone from a digital television (DTV) station were taken at a 24 element vertical array located 168 km from the transmitter. Measurements were recorded over a period of 15 days in a region known for lower tropospheric ducting, a phenomenon in which abnormal atmospheric refractivity patterns allow for the exceptionally long range propagation of electromagnetic (EM) radiation. The DTV station was positioned over the horizon relative the receiver array such that line of sight was obstructed, thus significant diffraction loss was expected. Direction of arrival (DOA) estimation was performed on the measurements. The focus of the study was to record long term array measurements of a signal propagating through a refractive channel to investigate whether array specific quantities such as array signal to noise ratio (ASNR) or DOA could be used to enhance estimates of atmospheric refractivity. An analysis is performed on the collected data and it is shown that ASNR in particular exhibits strong correlation with atmospheric parameters related to refractivity.

5.1 Introduction

It is well known that radio waves propagating through Earth's troposphere can experience significant variation in field strength due to weather related factors. Foremost of these factors is the refractive index of the Earth's lower troposphere. A strong negative gradient of the refractive index can cause EM waves to experience a phenomenon known as 'ducting', or 'trapping', which has the result of bending the wave over Earth's horizon to produce signal strengths as much as tens of dB above what is otherwise expected, even at distances very far from the point of transmission [1].

The refractive index of the troposphere is primarily determined by three factors; water vapor pressure, temperature, and atmospheric pressure. The dominant factor is water vapor pressure, which causes atmospheric processes involving hydrolapse (rapid change in moisture with height) to result in the likely formation of a duct. This is nearly always true over the ocean [2], and produces a particular type of duct low to the ocean surface known as the evaporation duct, which can reach tens of meters in height. These are typically observed in coastal regions, and are particularly common over the Southern coast of California [3].

The adverse effects of ducting on radar measurements has been the driving force for many studies on radio wave propagation through refractive environments. Many of these studies are narrowly focused towards ducting's influence on received signal strength [4, 5, 6, 7, 8]. Many more studies have revolved around simulations of radio wave propagation through known refractive environments [9, 10], typically performed using some form of the parabolic equation (PE) method [11]. Recently, measurement and simulation have been combined in *refractivity inversion*, where the atmospheric refractivity profile is inferred from radar clutter measurements [12, 13, 14, 15, 16, 17, 18]. While refractivity inversion has demonstrated some success, it is not perfect and suffers from several known issues [19, 20].

The issues that must be addressed in refractivity inversion include the computationally

costly nature of the PE forward model and the difficult non-convex optimization involved in producing the refractivity estimate. While advances in commercially available computational power may partially address these issues, refractivity inversion may further be improved through the inclusion of additional measurement parameters. We propose that by incorporating measurements that can only be taken by a phase coherent array system such as direction of arrival (DOA) of the wavefront and array signal to noise ratio (ASNR), the search space of possible refractivity estimates may be narrowed. For instance, DOA can be modeled using ray trace algorithms which are computationally efficient relative to PE modeling [21, 22]. By combining inversions using DOA, ASNR, and propagation loss measurements it may be possible to increase both the efficiency and accuracy of the inversion.

This work is a preliminary measurement campaign to collect DOA and ASNR measurements of electromagnetic (EM) waves propagating through a refractive environment. Many theoretical works state that variation in atmospheric refractivity within a transmission channel will cause variation in the DOA of EM waves propagating through that channel [23, 24, 25], however, little has been done towards proving this to be true [26]. If it is found that variations in the refractivity profile within a radio channel can cause the measured DOA of the radio signal to vary by a measurable amount (as is expected), then work can proceed towards incorporating such measurements into a stronger refractivity inversion framework.

The measurement campaign was conducted over a period of 15 days from November 19 through December 03, 2019. The pilot tone from a digital television (DTV) station, was recorded by a phase coherent receiver array positioned 168 km from the transmission sight. The transmission channel was located in coastal Southern California, a region known for ducting [3]. Only the narrowband pilot tone from the DTV station, at 584.33 MHz, was used to determine the DOA.

The paper is structured as follows. In Sec. 5.2 the experimental setup is detailed, including details about the receiver array, the transmitted signal, and a review of refractivity

and EM propagation. In Sec. 5.3, the theoretical model for the array measurements is detailed, array calibration process is described, and DOA estimation is reviewed. In Sec. 5.4 the data are analyzed and results displayed. The findings are discussed and the paper is concluded in Sec. 5.5. An Appendix is included with specifications of the array system and part numbers.

5.2   Experiment Description

The pilot tone of a digital television (DTV) station was recorded continuously by a vertical line array located on the Southern coast of California, Fig. 5.1. The DTV transmitter was located over the horizon (OTH) relative to the receiver array and over a partial marine propagation channel. The focus of the study was to make observations concerning the long term stability of the DOA of radio waves propagating over the horizon. We theorize that by measuring the DOA of signals propagating through a refractive environment, some additional information about the refractive environment can be obtained that isn't given by the propagation loss of the signal.

5.2.1   Measured Signal

The signal being measured was the pilot tone from a DTV station broadcasting from Mt. Wilson in Angeles national forest (34° 13' 27.0" N, 118° 3' 47.2" W). The signal path is displayed in Fig. 5.1. The transmitter was located 167.8 km from the receiver array at an elevation of 1765 m above mean sea level. At the time of measurements the DTV station (callsign KTBN-TV) was transmitting a horizontally polarized signal at 1000 kW effective radiated power over a 6 MHz bandwidth between 584–590 MHz. Only the amplitude and phase of the DTV station pilot tone at frequency $f_c = 584.33$ MHz was recorded at the receiver array.
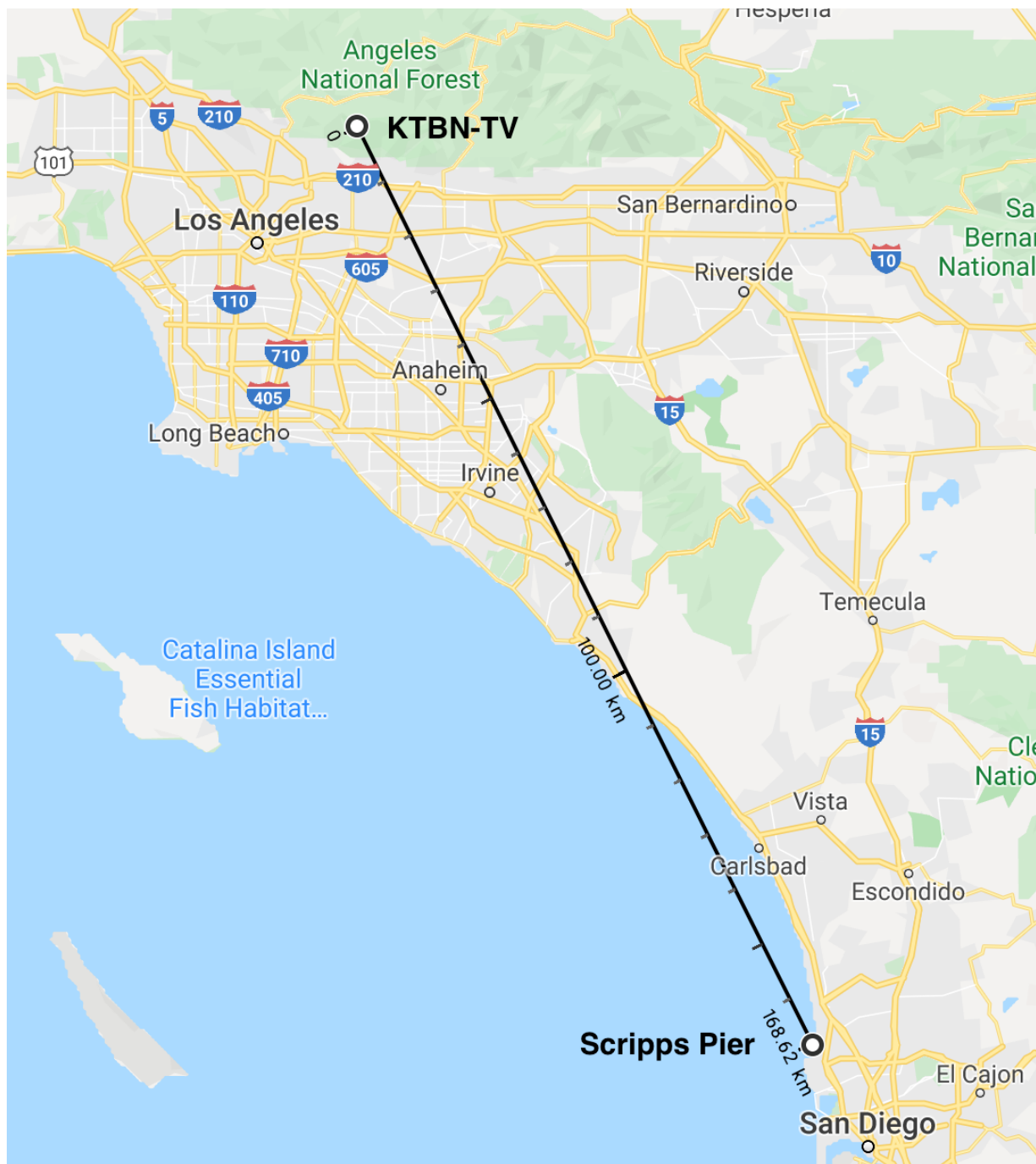
Figure 5.1: Map of signal path from KTBN-TV transmitter to receiver array at Scripps Pier.

5.2.2   Receiver Array

EM measurements were observed by a 24 element phase coherent array composed of six software defined radios (SDR). Each radio consisted of 4 receive channels connected to vertically polarized monopole antennas by 9.14 m cables. The antennas were affixed to a vertical mast with uniform inter-element spacing of .257 m, giving the array a total aperture of $a_r = 5.91$ m. The bottom-most antenna was positioned at an elevation of 10.8 m above mean sea level. The array was located at the end of Ellen Browning Scripps Memorial Pier (lat $32°52'1.4''$ N, long $117°15'26.7''$ W). An image of the antenna mast and system setup is provided in Fig. 5.2, and a system diagram is provided in Fig. 5.3.

All radios were driven using the same external 10 MHz reference clock and pulse per second (PPS) signal derived from the 10 MHz reference. The reference clock and PPS signals were split using an 8 way clock splitter, and connected to each radio through identical length cables. The reference clock was fed to a frequency synthesizer to produce a tone at the desired center frequency 584.25 MHz, which was split again and used as a local oscillator (LO) for each radio. The signals captured by each radio were recorded by a data server using open source GNUradio software. A list of hardware used in the receiver array is provided in Appendix 5.6.

All radios recorded at a sample rate of $f_s = 244.14$ k samples per second, using the LO as the carrier frequency. The in-phase and quadrature (IQ) data streams from each channel were recorded continuously by the data server. The data server, clocks, and radios were stored in a temperature and humidity controlled building nearby the antenna mast. The data streams from each antenna were labeled channels 1 through 24, with channel 1 as the lowest elevation receiver and channel 24 as the highest. One additional antenna was placed below channel 1, which transmitted a calibration sequence across the array from array endfire ($-90°$ elevation angle).

Figure 5.2: Coherent receiver array positioned on the end of Scripps Pier and control station setup inside nearby shed.
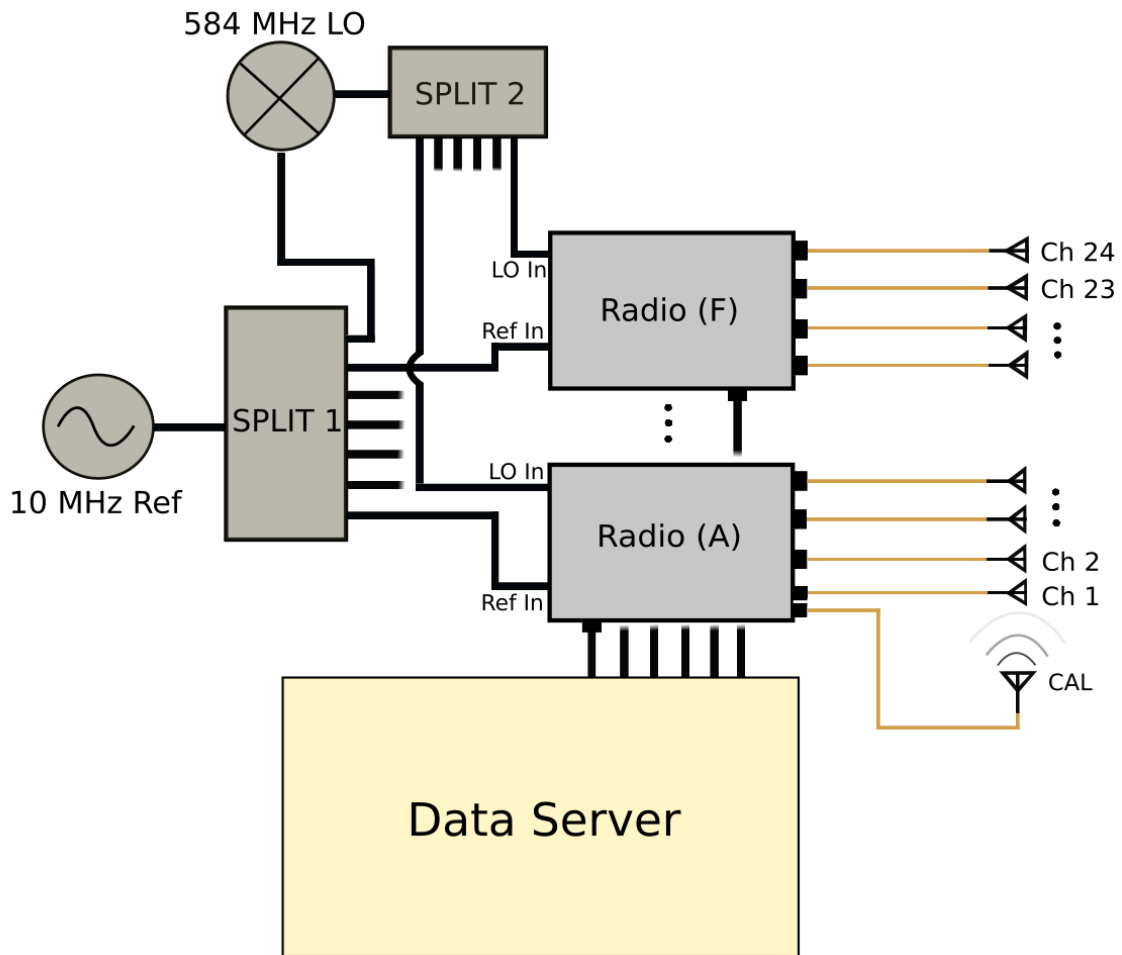
Figure 5.3: Receiver array system diagram.

5.2.3 Theoretical Background

Refractivity and Ducting

It is well known that the propagation of electromagnetic (EM) waves can be significantly influenced by the vertical refractive structure of the troposphere [27]. The index of refraction, n, or refractivity, $N = (n-1) \times 10^6$, is a measure of the propagation velocity of an EM wave in a medium,

$$n = \frac{c}{v} \tag{5.1}$$

where $c = 3 \times 10^8$ m/s is the speed of light in a vacuum and v is the speed of propagation in a particular medium. Any medium with non constant refractive index will cause EM waves propagating through it to bend. One such medium is the Earth's troposphere, which has a vertical refractive gradient dependent on several atmospheric thermodynamic properties,

$$N = \frac{77.6}{T}(p + 4810\frac{e}{T}), \tag{5.2}$$

where T is air temperature (K), p is atmospheric pressure (hPa), and e is water vapor pressure (hPa). Taking into account Earth's curvature, modified refractivity, M, is used to more easily classify the effects of refractivity by transforming Earth to an idealized flat surface,

$$M(z) = N + \frac{z}{R} \times 10^6, \tag{5.3}$$

where z is height above the earth's surface and R is the radius of the Earth.

There are several well known propagation regimes which are defined by the gradient of $M(z)$. These propagation regimes include standard troposphere ($0.079 \leq \frac{\partial M}{\partial z} \leq 0.157$), super-refraction ($0 \leq \frac{\partial M}{\partial z} < 0.079$), sub-refraction ($0.157 < \frac{\partial M}{\partial z}$), and ducting ($\frac{\partial M}{\partial z} < 0$), where $\frac{\partial M}{\partial z}$ has units of M-units/m. Standard troposphere and super-refraction result in radio waves bending

slightly towards Earth's surface, while sub-refraction results in radio waves being bent away from Earth, into outer space. Of the propagation regimes, ducting is the most studied because it has a 'trapping' effect for EM waves caught within the duct. The result is that ducts act as pseudo-waveguides that can bend EM waves over the radio horizon to be detectable at significantly longer ranges than would otherwise be expected.

The trapping layer of a duct is defined as the region in which $\frac{dM}{dz} < 0$, and can either start at the surface of the earth (surface based duct) or at some non-zero elevation (elevated duct). An important subset of surface based ducts are known as evaporation ducts, which are common above water and are caused by a large humidity gradient just above the water's surface. Evaporation ducts can range in height from a few meters to several tens of meters, and are known to be common in warm coastal regions such as the Southern coast of California [28]. The seasonal frequency of ducting events is thought to be maximum in the summer months [29].

There has been significant effort towards modeling the propagation loss experienced by EM waves propagating through ducts using simulation tools such as the split step parabolic equation [10, 15, 30, 19]. In response to the success of PE modeling, measurement campaigns have been launched towards observing the actual propagation loss experienced by ducted signals [8]. The ultimate goal is comprehensive modeling and prediction of the troposphere's refractivity structure in real time. Often lost in simulation and experimental measurements is the spatial phase pattern of the recorded wavefronts, which could be used to determine the DOA of the incoming signal. Through physical measurement of wavefront DOA, this work aims to provide an answer to how the DOA of a signal propagating through a refractive environment might change over time.

Wireless Propagation

It is generally accepted that for a signal to be received without significant propagation loss due to diffraction, the direct path between the transmitter and receiver must have adequate

clearance. The obstacle created by the curvature of the Earth for signals propagating over the horizon is known as '*Earth's bulge*', and because Earth's standard troposphere has a negative modified refractivity gradient, RF waves generally bend towards the surface of the Earth. This effectively reduces Earth's bulge height and extends the radio horizon.

To compensate for curvature in the path of an RF wave propagating through standard atmospheric conditions, it is common to substitute Earth's radius with 4/3rds of its true value to estimate the radio harizon [31]. This is sufficient for signals propagating over terrestrial paths in mid to high latitude regions of the Earth because standard atmospheric conditions are common in those locations, however marine environments are known to experience higher variability in refractive conditions [32] and are less well predicted using the 4/3rds approximation. Because the vertical refractivity gradient determines the effective Earth's radius when calculating the radio horizon, we expect it to influence both DOA and propagation loss of the wavefront at the receiver.

The amount of clearance required between a transmitter and receiver for clear signal reception is calculated using the radii of the first Fresnel zone,

$$F_1 = \frac{1}{2}\sqrt{\lambda D}, \qquad (5.4)$$

where $\lambda = \frac{v}{f_c} = .5134$ m is the signal wavelength and $D = 167.8$ km is the distance between the transmitter and receiver, thus the first Fresnel radii of the channel was 146.8 m.

In the strict sense, a 'line of sight' connection between a transmitter and receiver is defined as a connection where the first Fresnel zone is completely unobstructed. In practice it has been reported that 60% of the first Fresnel zone should be unobstructed for strong signal reception [31]. Figure 5.4 depicts the first Fresnel zone of the propagation path (to scale) for Earth's true radius and the 4/3rds augmentation. In neither case is the propagation path completely unobstructed.

Slight changes in the atmospheric refractivity gradient correspond to changes in the radio horizon experienced by the DTV signal, which in turn should translate to measurable quantities
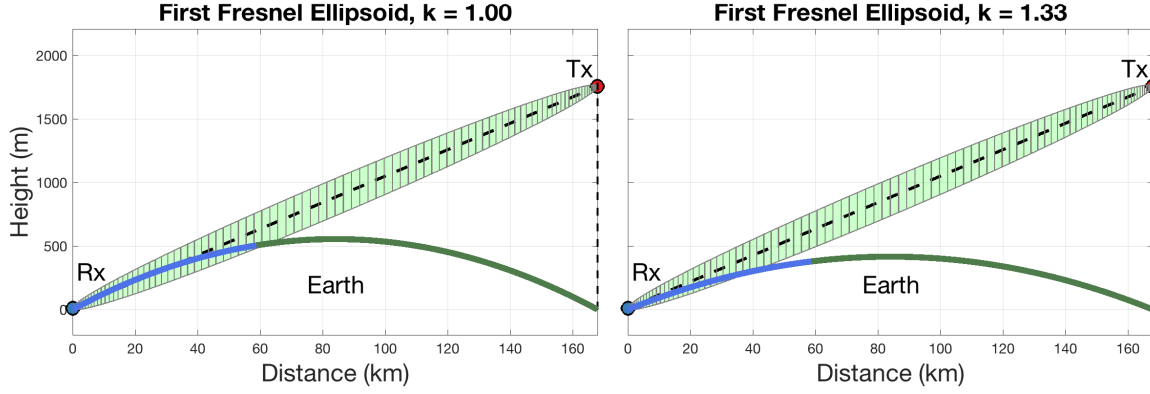
Figure 5.4: First Fresnel zone diagrams (to scale) using standard Earth's radius ($k = 1$) and $k = 4/3$rds Earth's radius ($k = 1.33$). Green represents portion of channel over terrestrial path, blue represents portion of channel over marine path.

such as ASNR and DOA. Because the atmospheric refractivity gradient fluctuates over marine channels, we expect the effect of these fluctuations to be observable in long term measurements of the DTV signal. Abnormally clear reception likely corresponds to super-refraction or ducting within the channel while abnormally low signal reception corresponds to sub-refraction.

5.3   Array Calibration and Processing

5.3.1   Signal Model

Consider a uniform linear array (ULA) of M antennas receiving K narrowband far field signals. A common array measurement model is concerned only with the magnitude and phase of a narrowband signal (i.e. the value at a particular DFT bin) as it is measured at each element of an array

$$\mathbf{y}[t] = \mathbf{A}\mathbf{s}[t] + \mathbf{n}[t], \tag{5.5}$$

where $\mathbf{y}[t] \in \mathbb{C}^M$ is the complex valued measurement snapshot vector composed of the signal received at each of M antennas at time t, $\mathbf{s}[t] \in \mathbb{C}^K$ is a vector of signals arriving from K directions,

$\mathbf{n}[t] \in \mathbb{C}^M$ is a vector of noise at time t, and $\mathbf{A} = [\mathbf{a}(\theta_1) \ldots \mathbf{a}(\theta_K)]$ is known as the *array manifold matrix*. The columns of the array manifold matrix are known as *array steering vectors*, and contain the phase pattern across the array expected from a signal arriving at angle θ. The array steering vector of a ULA is

$$\mathbf{a}(\theta) = \begin{bmatrix} 1 \; e^{j2\pi d \sin(\theta)} \; \ldots \; e^{j2\pi(M-1)d\sin(\theta)} \end{bmatrix}^\mathsf{T}, \tag{5.6}$$

where $\theta \in [-90°, 90°)$, d is the inter-element array spacing in wavelengths of the narrowband signal being detected. The receiver array measured the pilot tone of a DTV station at frequency $f_c = 584.33$ MHz. Assuming the DTV signal propagates at the speed of light, $c = 3 \times 10^8$ m/s, the wavelength is $v/f_c = .5134$ m and the array elements, which are separated by .257 m, have half wavelength inter-element spacing.

5.3.2   Data Format

The continuous data streams from each channel were buffered into frames of 2^{12} consecutive time samples. Each channel used a receiver gain of 30 dB, and signals were recorded at their absolute magnitude without normalization. We denote the time domain data frame from channel i and time t as $r_i[t] \in \mathbb{C}^{4096}$. Two operations were performed on each data frame:

1. A length 2^{12} discrete Fourier transform was applied to each data frame using a Hamming window. The value of the frequency bin containing the DTV pilot tone for each channel was collected in a vector $\mathbf{y}[t] \in \mathbb{C}^{24}$. We refer to $\mathbf{y}[t]$ as the data 'snapshot' at time t. The FFT bin containing the pilot tone was decided at the start of the measurement campaign and held constant over the measurements.

2. Each data frame was correlated with the calibration sequence (detailed in Sec. 5.3.3) and the phase of the correlator peak was collected in a calibration vector $\varphi[t]$, used to correct the phase of $\mathbf{y}[t]$.
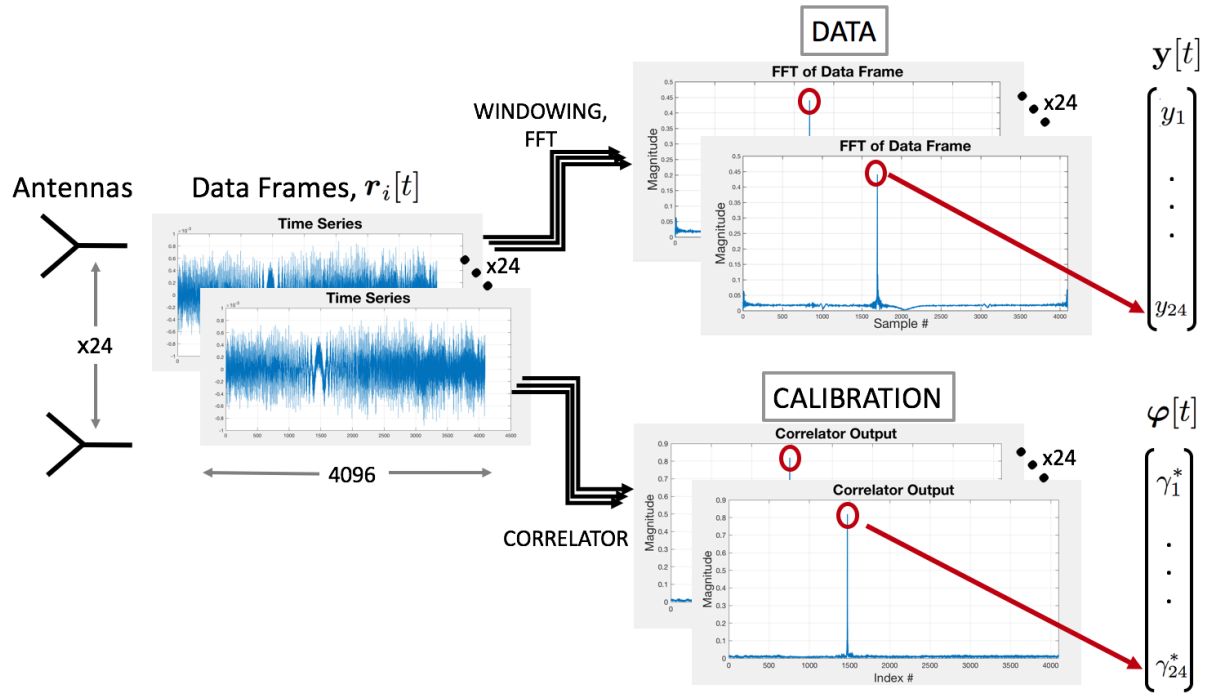
Figure 5.5: Depiction of the signal processing path taken by samples as they are recorded at the array. All subfigures generated from Cliffside test data (see Sec. 5.3.8).

A dataflow diagram is presented in Fig. 5.5.

The relatively large frame size was chosen to reduce the amount of storage required for the measurements. Each radio was run at a sample rate of 244.14 kHz, thus one snapshot was recorded every .0168 seconds, effectively reducing the amount of data to be stored by a factor of 2^{12}. The receiver array recorded continuously for 15 days between November 19 and December 3, 2019.

5.3.3   Array Calibration

The array steering vector defined in (5.6) is valid only for array measurements which are both *synchronous* and *phase coherent*. An array which is said to be synchronous samples each array element at identical sample rates. Phase coherent refers to a synchronous array system where the sample clock edge occurs at the same time instant on each channel.

For theoretical applications, the RF signal is often assumed to be sampled as it is received at the antenna, though in practice the signal propagates down a coaxial cable, through various stages of the 'RF chain' (for example filtering and mixing), and is finally sampled at an analog to digital converter (ADC). For phase coherent measurements, the phase pattern experienced by the antennas must be preserved through the cables and RF chain. Calibration is used to mitigate errors caused by differences in cable lengths and RF chain components due to manufacturing imperfections.

Continuous array calibration is necessary for two reasons: first, the mixer in each RF chain will adopt an unknown phase offset at startup (i.e. the sample clock edges are not aligned for each channel). The result is that each channel will have a unknown phase offset which is modeled by expanding (5.5)

$$\mathbf{y}[t] = \boldsymbol{\phi} \odot (\mathbf{A}\mathbf{s}[t] + \mathbf{n}[t]), \tag{5.7}$$

where $\boldsymbol{\phi} \in \mathbb{C}^M$ is a vector of unit magnitude complex numbers representing the unknown phase offset at each channel and $\odot$ is the Hadamard (element-wise) product. Next, the effects of system aging and temperature influences (i.e. expansion of cables and system components due to heating applied unevenly across the system, for instance by sunlight hitting some cables but not others).

The same reference clock and PPS signal were fed to all radios to achieve synchronous sampling. A repeating length 2^{12} Zadoff-Chu (ZC) calibration sequence, $z \in \mathbb{C}^{4096}$ with root parameter $R = 501$ [33] was transmitted from array endfire ($-90°$ elevation angle). The cross correlation was taken between the calibration sequence and the data frame from each channel as

$$\gamma_i[t] = \mathcal{F}^{-1}\left(\mathcal{F}(z)\overline{\mathcal{F}(r_i[t])}\right), \tag{5.8}$$

where $\mathcal{F}$ represents the discrete Fourier transform, $r_i \in \mathbb{C}^{4096}$ is the data frame from channel i, and $^-$ denotes the complex conjugate.

The element of $\gamma_i[t]$ with largest magnitude was taken from each channel and placed in a vector,

$$\varphi[t] = \begin{bmatrix} \gamma_1^*[t] \cdots \gamma_{24}^*[t] \end{bmatrix}^\mathsf{T}, \quad \gamma_i^*[t] = \max\left(\gamma_i[t]\right), \tag{5.9}$$

where the max function is understood to return the complex value of the element with largest magnitude. The phase angle of each element of φ represents the phase of the calibration signal as it arrived at each array element. Because the calibration signal arrived from $-90°$ below the array, its phase across the array is known (see eq. (5.6)). Thus the unknown phase offset at each channel at time t is estimated as

$$\phi_i[t] = \frac{\varphi_i[t]}{|\varphi_i|[t]}\overline{\mathbf{a}(-90°)_i}. \tag{5.10}$$

Calibration was taken for each data frame and applied to the measurements. The data path through the array is visualized in Fig. 5.5. We remark that the calibration sequence was transmitted continuously and potential exists for interference between the calibration sequence and the DTV pilot.

5.3.4 Conventional DOA (CBF)

The conventional beamformer (CBF), also known as the Bartlett beamformer is the oldest and most robust of the DOA estimation techniques [34]. The first step of CBF involves forming the sample covariance matrix (SCM) of the measurements,

$$\mathbf{R}_{yy} = \frac{1}{T}\sum_{t=1}^{T}\mathbf{y}[t]\mathbf{y}[t]^\mathsf{H}, \tag{5.11}$$

where $^\mathsf{H}$ denotes the conjugate transpose. The SCM is an estimate of the true covariance matrix of the measurements. If the source directions are static then a longer resolution period (larger

T) will produce a SCM which better estimates the true covariance matrix, in turn enhancing the accuracy of CBF.

CBF is performed by calculating the angular power spectrum of the sample covariance matrix over the range of possible DOAs. The angular power spectrum of CBF is

$$P_{\text{CBF}}(\theta) = \mathbf{a}^{\mathsf{H}}(\theta)\mathbf{R}_{yy}\mathbf{a}(\theta), \tag{5.12}$$

for $\theta \in [-90°, 90°)$. The DOAs of the signals composing the measurements will produce peaks in $P_{\text{CBF}}(\theta)$. Note that (5.12) covers only the 180° in-front of the array, and signals arriving from the other 180° produce the same phase pattern across the array as their positive angle counterparts (i.e. $\mathbf{a}(0°) = \mathbf{a}(180°)$), thus an ambiguity exists between signals arriving at the front and back of the array.

The classical beamformer is reliable and has been proven effective on experimental data [35, 36], however, it is also known to have poor angular resolution. In particular, the spectral response from any strong signal can have significant sidelobes which can obscure the spectral response of weaker signals arriving at nearby angles. To ensure accurate DOA estimates, a high resolution algorithm known as *Gridless* DOA estimation is also employed.

5.3.5 Gridless DOA Estimation

Gridless DOA estimation is an advancement of compressive sensing based DOA estimation [37] in which the DOAs are found by minimizing the atomic ℓ_0 norm of atoms defined by the manifold of the array steering matrix [38, 39, 40, 41, 42]. The technique is named for its ability to resolve DOAs at any angle, an improvement over earlier compressive DOA estimation methods in which DOAs were limited to lie on a user specified grid. Gridless DOA estimation is achieved

as the optimal solution of the following rank constrained optimization problem

$$\underset{\mathbf{T}\in\mathcal{T},\mathbf{Q}}{\text{minimize}} \quad \text{rank}(\mathbf{T}), \quad \text{subject to} \quad \mathbf{S}\succeq 0, \tag{5.13}$$

where

$$\mathbf{S} = \begin{bmatrix} \mathbf{T} & \mathbf{Y} \\ \mathbf{Y}^{\mathsf{H}} & \mathbf{Q} \end{bmatrix}, \tag{5.14}$$

$\mathcal{T}$ is the set of Toeplitz matrices, $\mathbf{Q}$ is a free variable, and $\mathbf{Y} = \begin{bmatrix} \mathbf{y}[t_1] & \dots & \mathbf{y}[t_n] \end{bmatrix}$ is a matrix of measurement snapshots of arbitrary size. Once the optimal $\mathbf{T}$ is found the DOAs are recovered through Vandermonde decomposition of $\mathbf{T}$.

Because (5.13) is non-convex, it has no well known general solution. In practice (5.13) is substituted for its convex relaxation [41],

$$\underset{\mathbf{T}\in\mathcal{T},\mathbf{Q}}{\text{minimize}} \quad \text{Tr}(\mathbf{T}) + \text{Tr}(\mathbf{Q}), \quad \text{subject to} \quad \mathbf{S}\succeq 0. \tag{5.15}$$

where $\text{Tr}(.)$ is the matrix trace. When the matrix rank is substituted for the matrix trace the optimization of (5.13) takes the form of a semi-definite program (SDP), to which there are many available solvers. In this work (5.15) is solved using the popular alternating directions method of multipliers (ADMM) algorithm [43]. A derivation of the algorithm is found in [40].

5.3.6 Carrier Frequency Offset Removal

In applications where the transmitter and receiver do not share the same clock, it is well known that the receiver will experience a carrier frequency offset (CFO) [44]. CFO is defined as the frequency difference between the clocks used at the transmitter and receiver. If both clocks are stable over short time periods then their CFO is constant. In this case, the phase of a received narrowband signal will progress linearly in time at a rate proportional to the CFO. Over longer

intervals the CFO between clocks tends to drift randomly.

For the proposed application there are two ways in which CFO could present an issue. Firstly, the linear phase progression between subsequent measurements can cause DOA estimation errors by reducing the accuracy SCM. To avoid these errors the linear phase progression must be removed. We leverage the fact that the receiver array is synchronous, thus each channel experiences identical linear phase progression due to CFO. In this case the effects of CFO can be canceled by rotating each measurement snapshot $\mathbf{y}[t]$ by the conjugate phasor of any channel's measurements.

$$\hat{\mathbf{y}}[t] = \mathbf{y}[t]e^{-j\angle \mathbf{y}_1[t]}, \quad \forall t. \tag{5.16}$$

In this work we use channel 1. Equation (5.16) has the effect of eliminating phase drift in time while preserving the spatial phase pattern across the array elements. Because the DOA of a signal manifests as the spatial phase pattern across the array, CFO correction can be performed without impacting the DOA estimate.

The second issue that can arise due to CFO is the potential for the DTV pilot tone to drift between FFT frequency bins over the measurement campaign. Figure 5.6 tracks hourly CFO mean in radians per snapshots over the measurement period. Over 95% of hourly CFO mean fell between 1.15 and 1.3 radians per snapshot. At 4096 samples per snapshot, $f_s/4096 = 59.6$ measurement snapshots were recorded per second, thus the transmitter and receiver experienced a relative drift of $(1.3 - 1.15)59.6/(2\pi) = 1.42$ Hz over the measurement campaign. The FFT applied to each data frame had a bin width of $f_s/4096 = 59.6$ Hz, therefore we conclude the system was stable enough that the DTV pilot tone did not shift between FFT bins.
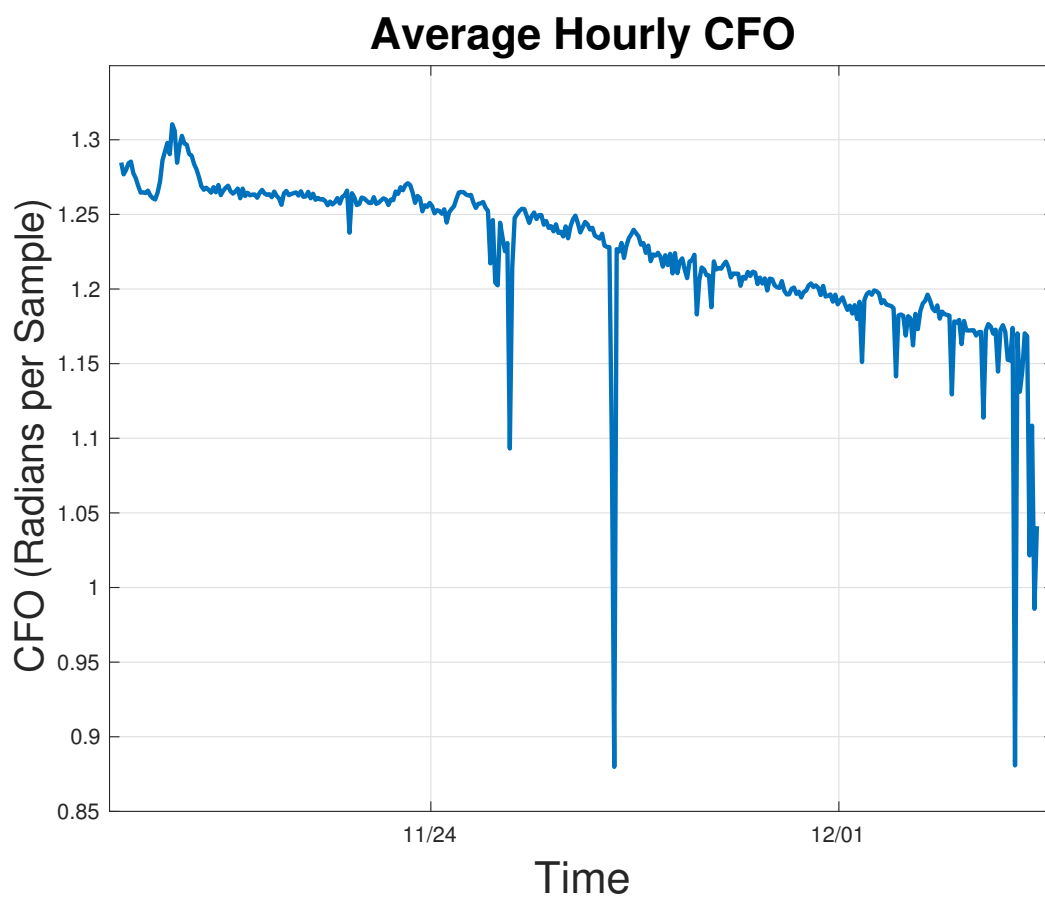
Figure 5.6: Mean CFO over each hour of recorded data.

5.3.7 SCM, Overlap, and Normalization

Several parameters which must be considered are how many measurement snapshots should be used to generate each SCM, and how much overlap should exist between measurements used to generate successive SCMs. Figure 5.7 depicts the time progression of the CBF spectrum from the same dataset using 1, 100, and 500 snapshot constructions of $\mathbf{R}_{yy}$.

If too few snapshots are used to construct the SCM the true covariance may not be accurately approximated, leading to a CBF spectrum dominated by noise. If too many snapshots are used to construct the SCM the underlying assumption of stationarity may be violated (i.e. the true covariance may change over the period spanned by the snapshots), producing a blurry realization of the CBF spectrum. A general rule of thumb is that the SCM should be generated using 2–3 times as many snapshots as their are sensors to avoid producing a rank deficient SCM.

Overlap refers to the amount of shared measurements used to generate subsequent SCMs, and has the effect of further smoothing the spectrum in time. For instance, if the first SCM is constructed using measurement snapshots taken at time $t = 1, \ldots, 10$, the next SCM can be estimated from snapshots at time $t = 6, \ldots, 15$ for 50% overlap between consecutive estimates.

Once generated, each spectrum is normalized such that the peak spectral power is 1. This allows a time series of spectra from measurements with fluctuating ASNR to be displayed together.

5.3.8 Array Verification

Array functionality was verified by performing DOA estimation of test tones transmitted from three known locations within line of sight of the array. The view to or from each test location is displayed in Figure 5.8. The locations included the top floor of a nearby building, a cliffside, and the pilot tone from a DTV station transmitting from atop a nearby mountain. The building was University of California San Diego's Nierenberg Hall, positioned at elevation angle $5.3°$ relative
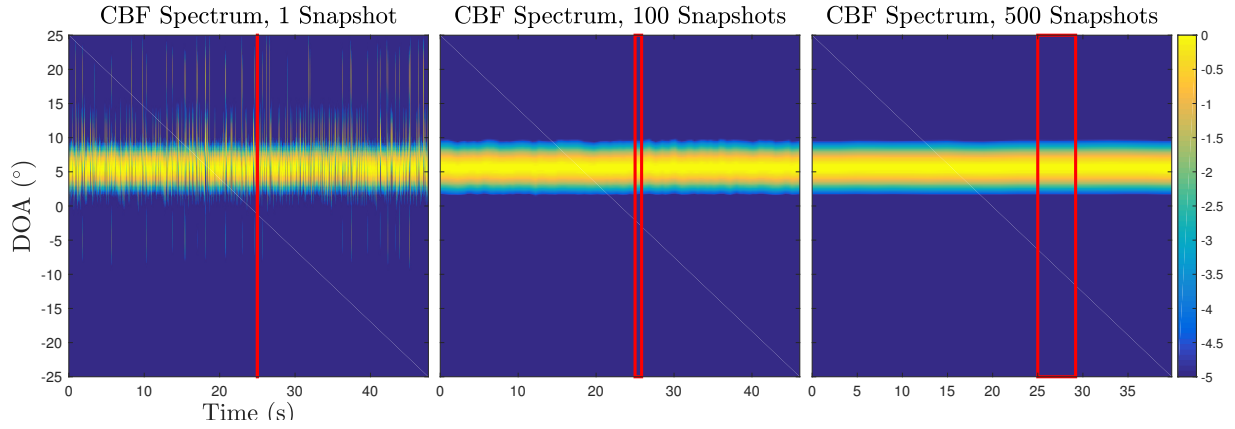
Figure 5.7: DOA estimates for sample covariance matrix estimated using varying snapshot counts. Left: 1 snapshot. Middle: 100 snapshots, 50% overlap. Right: 500 snapshots, 50% overlap. Red box shows snapshot window.

the receiver array (measured at site and confirmed using elevation data from the U.S. geographical service). Test tones were transmitted from Nierenberg Hall at frequencies 423, 915, 1265, and 2394 MHz, (U.S. amateur radio bands). The tone transmitted from the cliffside (elevation angle $4.8°$ relative to array) was centered at 915 MHz. DTV station KBNT-CD broadcast from Mt. Soledad, 2.2 km from the array, (elevation angle $4.7°$ relative to array) had pilot tone frequency of 530.33 MHz.

In all tests the transmitter and receiver positions were fixed and the propagation path was line of sight, thus the DOA in all cases was expected to be constant. Any fluctuation in the spectrum peak can be attributed to noise within the system. The total variation of the test tone DOA estimates provides a good benchmark for DOA estimation accuracy.

Figure 5.9 gives the time evolution of the CBF spectrum for each test tone transmitted from Nierenberg Hall using one second of measurement snapshots per SCM, and 50% overlap between estimates (see Sec. 5.3.2 and 5.3.7). As expected, the peak of the spectra are constant and centered at $5.3°$. The spectrum peak angle for all tones are plotted on top of each other, and the dominant DOA detected using gridless DOA is given alongside the CBF spectrum peak. DOAs estimated using the gridless method showed strong agreement with those estimated from

Figure 5.8: View from each test location. Left: view from UCSD Nierenberg Hall. Middle: view from cliffside transmitter sight (transmitter is log-periodic antenna on left). Right: view from reciever array to Mt. Soledad transmitter.

the CBF spectrum peak. The largest fluctuation in estimated DOA was from the CBF spectrum peak of the 423 MHz test tone, having a standard deviation of $0.051°$.

Figures 5.10 and 5.11 give the time evolution of the CBF spectrum and spectral peaks for the test tone broadcast from the cliffside location and pilot tone from KBNT-CD. Again, the estimated DOAs are constant at the expected arrival angle and gridless measurements exhibit strong agreement with the CBF spectrum peak. The standard deviation of the spectral peak DOAs from cliffside and KBNT-CD test locations were $0.016°$ and $0.044°$ respectively.

The performance of the array over all tests indicates the receiver array system was capable of detecting the DOA of the pilot tone from KTBN-TV with accuracy greater than $0.1°$.

5.4 Data Analysis

The CBF spectrum from Los Angeles station KTBN-TV was estimated using a sliding window of size $N_t = 128$ snapshots (roughly 2 minutes), and 50% overlap in measurements between consecutive spectrum estimates. Gridless DOA was also used to estimate the peak arrival
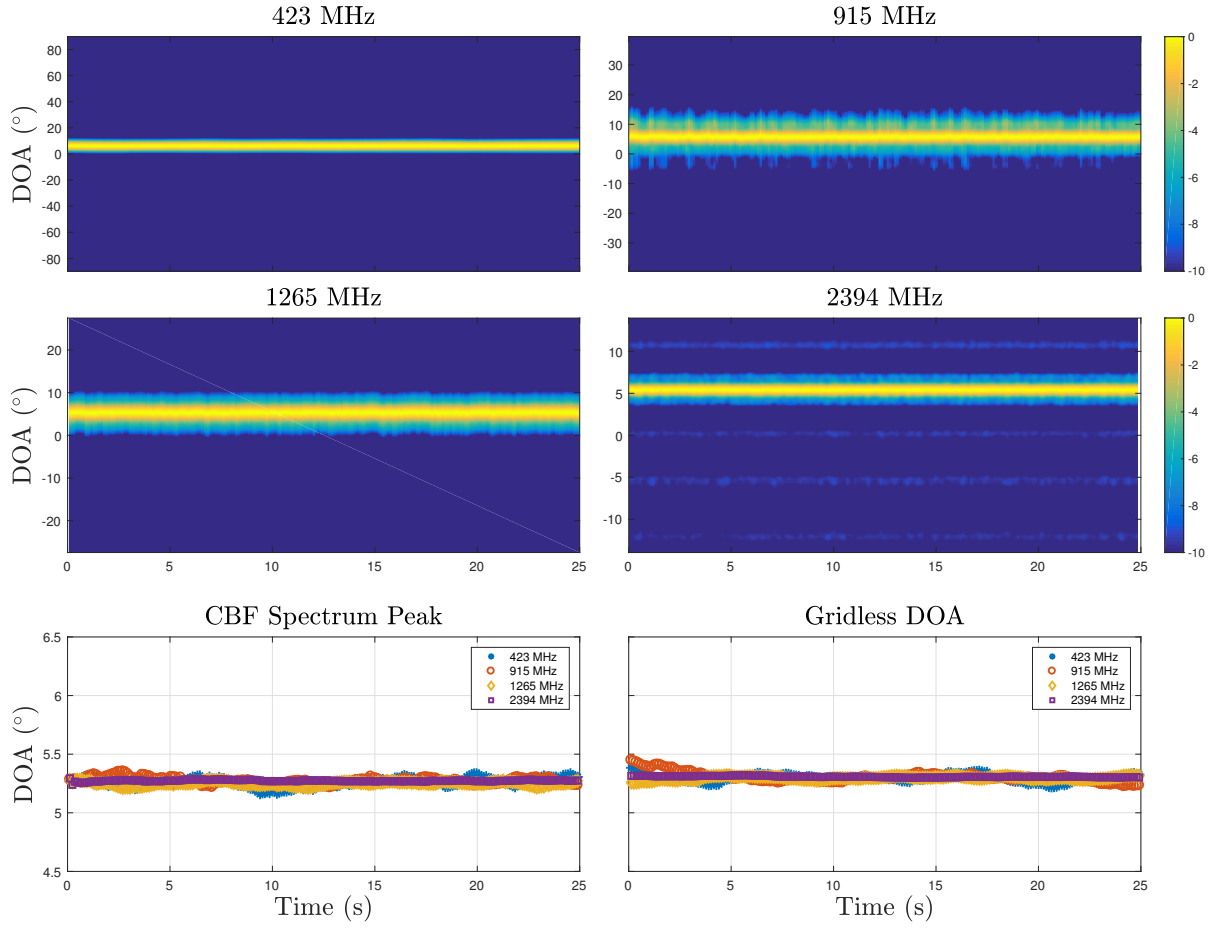
Figure 5.9: Receiver array DOA estimation test, CBF spectrum for 423, 915, 1265, and 2394 MHz narrowband tones transmitted from UCSD Nierenberg Hall (elevation angle = 5.3° relative to array). Top- CBF spectra for each test tone. Bottom- Peak of CBF spectra (left) and Gridless DOA estimate (right). Several minutes delay between measurements.
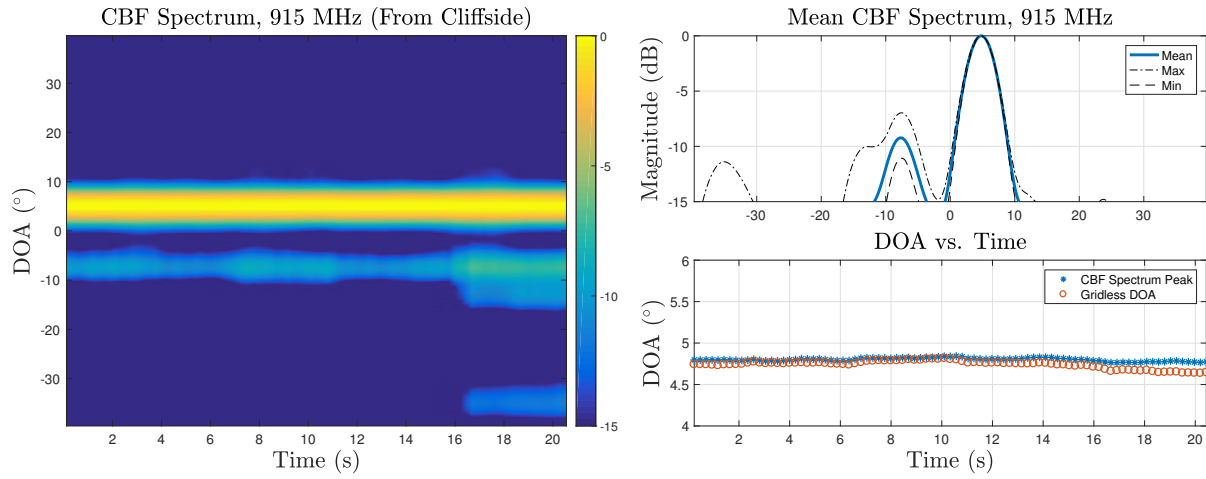
Figure 5.10: CBF spectrum from 915 MHz narrowband test tone transmitted from nearby cliffside (elevation angle 4.8° relative to array). Left- CBF spectrum in time. Right- mean spectrum over all measurements (top) and spectrum peak/gridless DOA estimate vs. time (bottom).
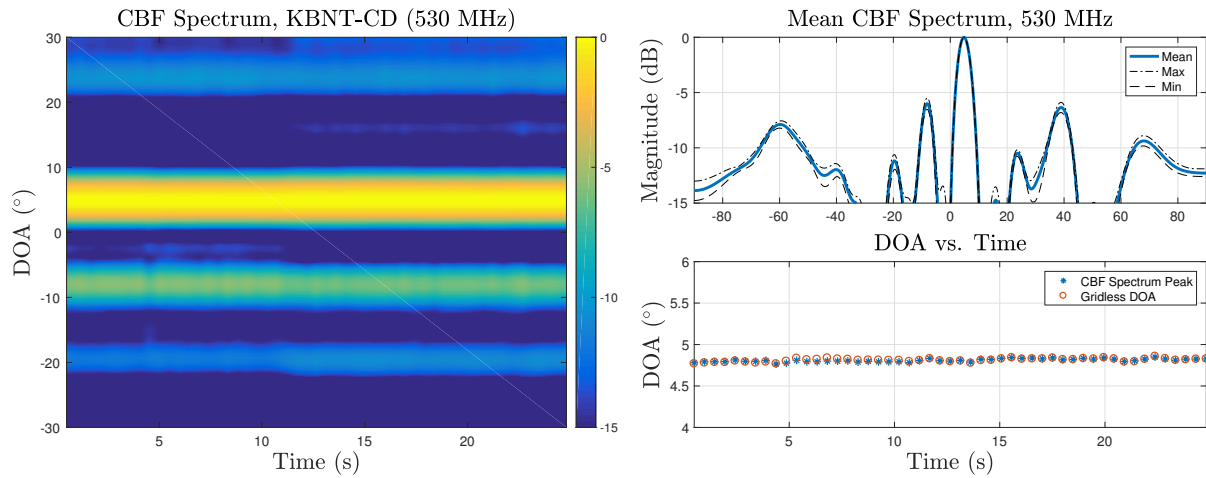
Figure 5.11: Third receiver array DOA verification, CBF spectrum for 530 MHz pilot tone transmitted from KBNTCD (located at nearby Mt. Soledad, elevation angle 4.7° relative to array). Left- CBF spectrum in time. Right- mean spectrum over all measurements (top) and spectrum peak/gridless DOA estimate vs. time (bottom).

angle. Other measured values include single channel received signal strength (RSS) and array signal to noise ratio (ASNR) at the receiver array, defined as

$$\text{RSS}_i[t] = 10\log_{10}\Big(|\mathbf{y}_i[t]|^2 \Big), \tag{5.17}$$

$$\text{ASNR} = 10\log_{10}\Big(\frac{\lambda_1}{\sum_{i=2}^{24} \lambda_i} \Big), \tag{5.18}$$

where $\text{RSS}_i[t]$ is the RSS at channel i and time t, and λ_i is the ith largest eigenvalue of an estimated SCM. RSS is a measure similar to propagation loss while ASNR represents the power ratio between the largest eigenvalue and all other eigenvalues of a SCM. If only one signal is being received then the SCM will be rank 1, however there is always noise within a system which causes the SCM to lose rank 1 structure and limits total ASNR.

Results of the measurement campaign are displayed in Figs. 5.12–5.16 alongside air temperature and precipitation taken at the time of measurement. Air temperature was recorded by the National Oceanic and Atmospheric Administration (NOAA) collection site located on Scripps Pier beside the receiver array. Hourly precipitation measurements were taken from the National Center for Atmospheric Research (NCAR), stage IV surface precipitation dataset [45] at the location of the receiver array. Figure 5.17 gives precipitation maps along the propagation channel during the period of most intense precipitation.

Dramatic changes in the CBF spectrum typically occur at the beginning of periods of precipitation or at times when ASNR dropped dramatically, for instance on November 20, 27, and 28 (see Figs. 5.12 and 5.15). This may be due to partial obstruction of the main signal path due to cloud cover or other obstructions, which causes signal energy from other DOAs to appear relatively stronger in comparison.

It has already been demonstrated that evaporation duct height can be estimated from RSS measurements across an array [46, 47], even without phase coherence between array elements. If
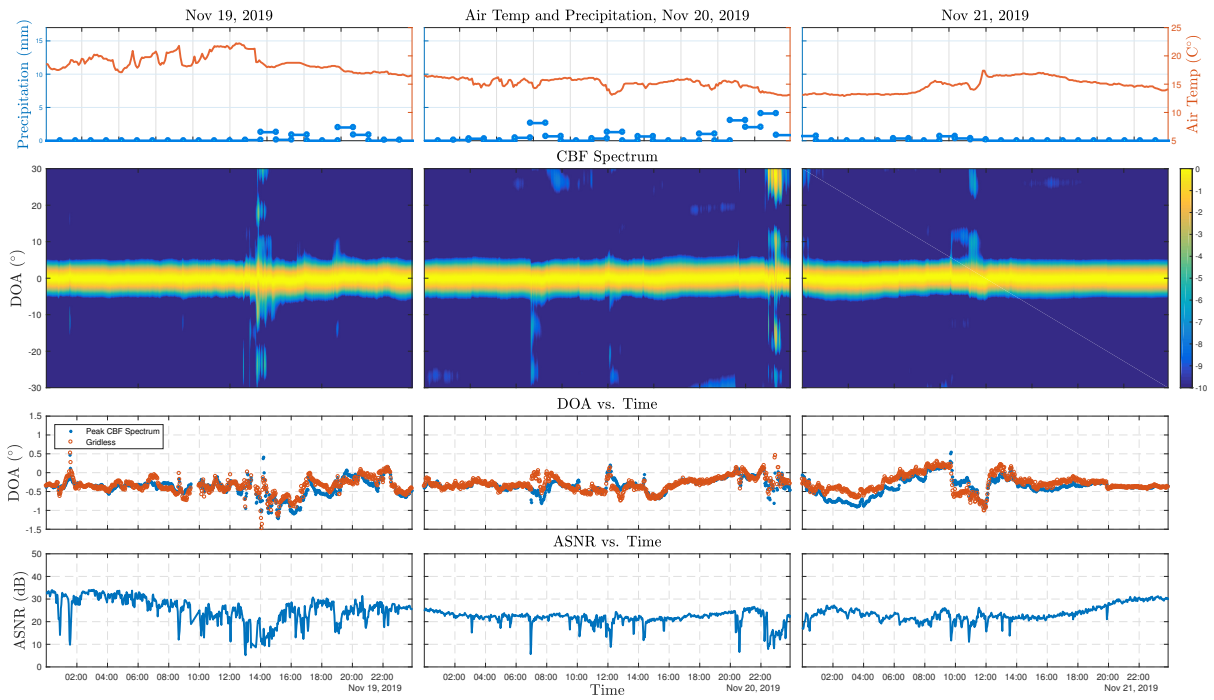
Figure 5.12: CBF spectrum of measurements taken on November 19–21, 2019. Top- Air temperature and precipitation vs. time. Middle: CBF spectrum vs. time using 128 snapshot sliding window with 50% overlap between windows, and spectrum peak plotted against gridless DOA estimation strongest DOA. Bottom- ASNR vs time.

147
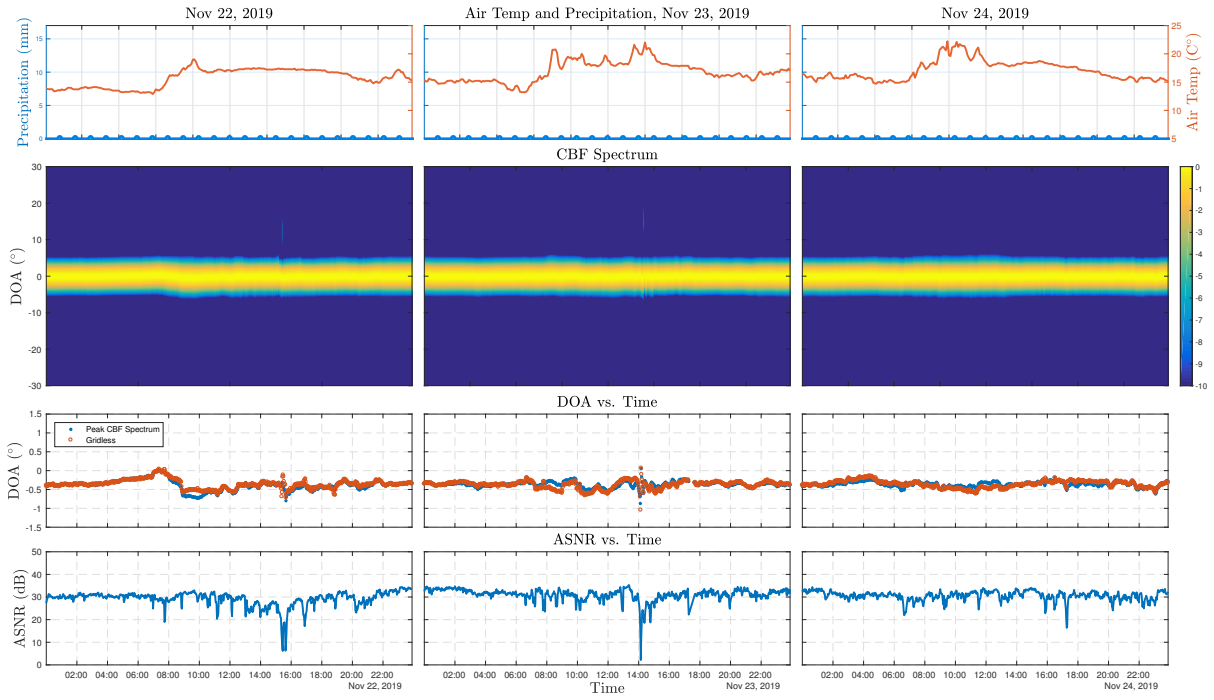
Figure 5.13: As in Figure 5.12, November 22–24, 2019.
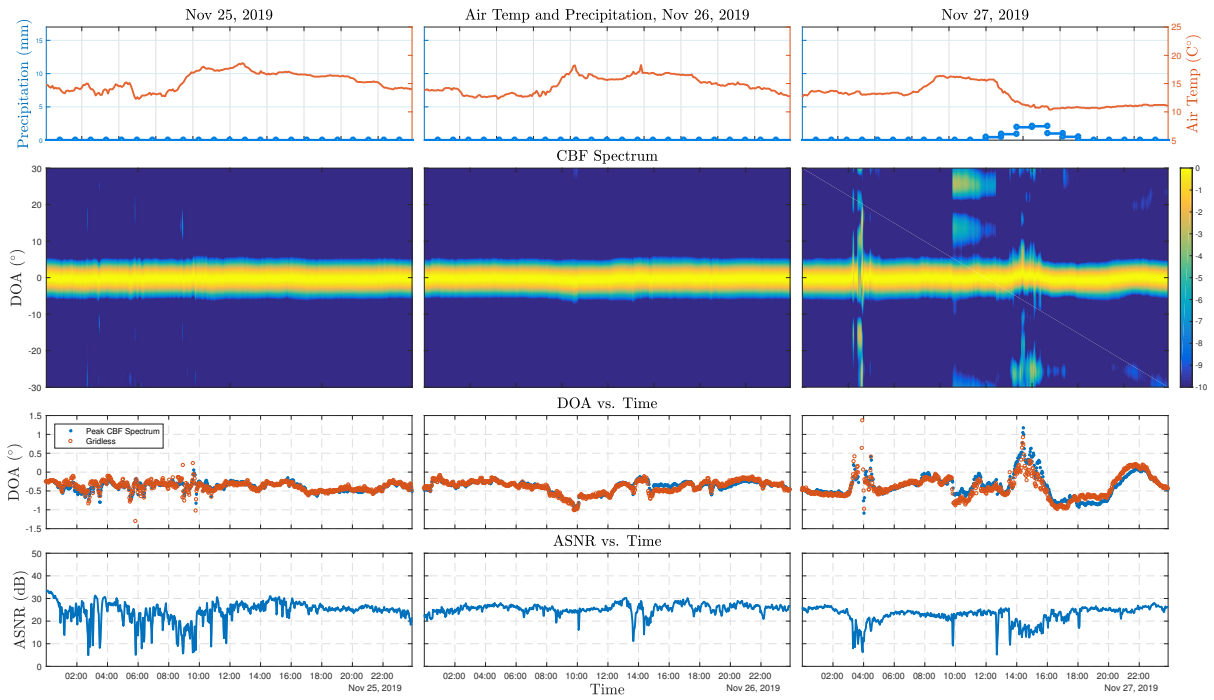
Figure 5.14: As in Figure 5.12, November 25–27, 2019.

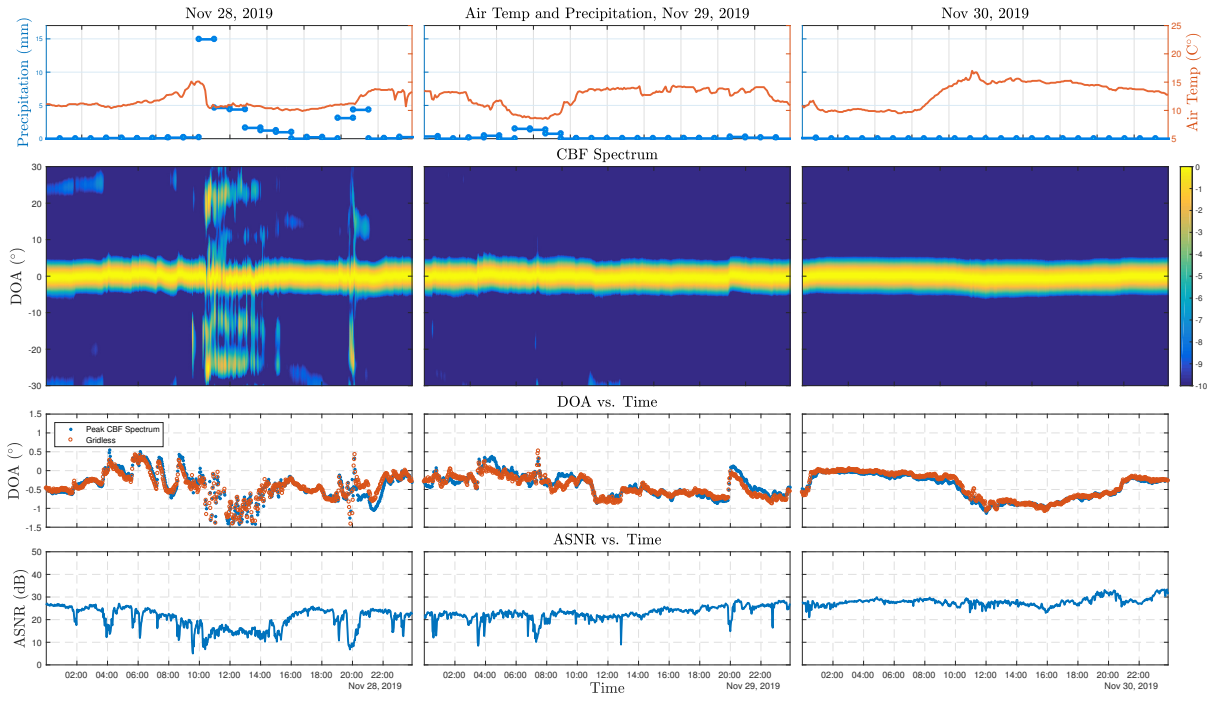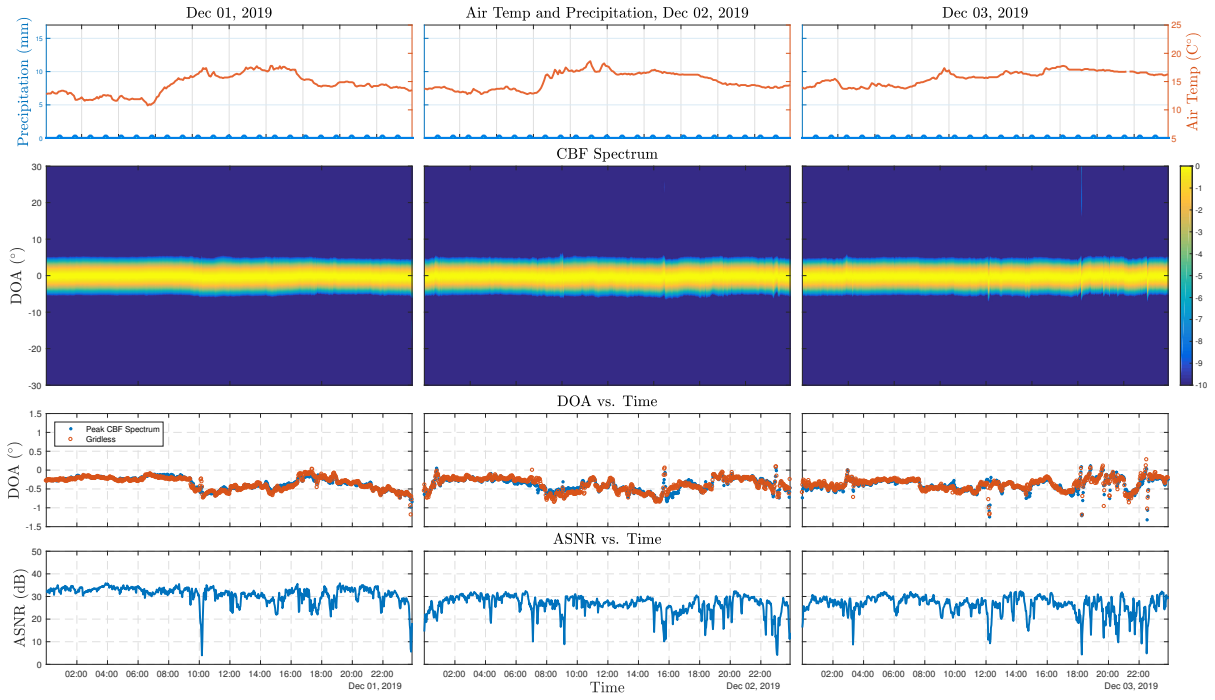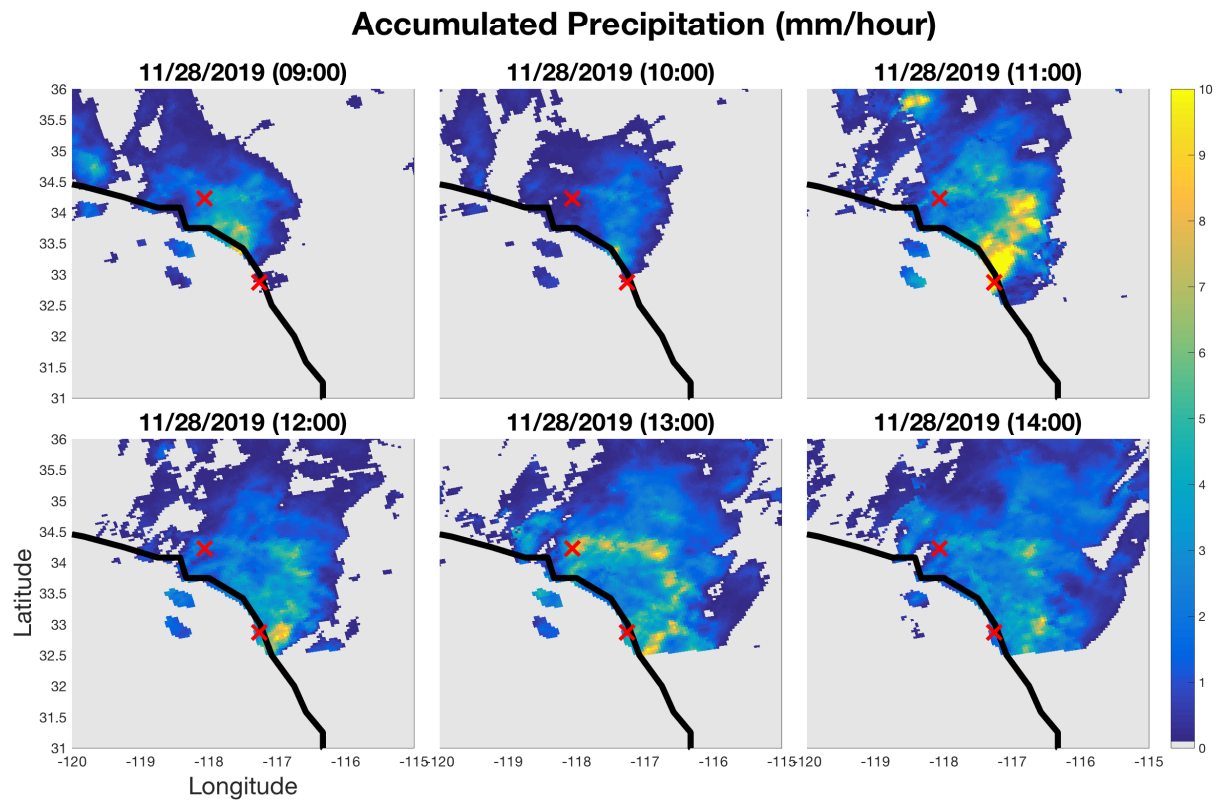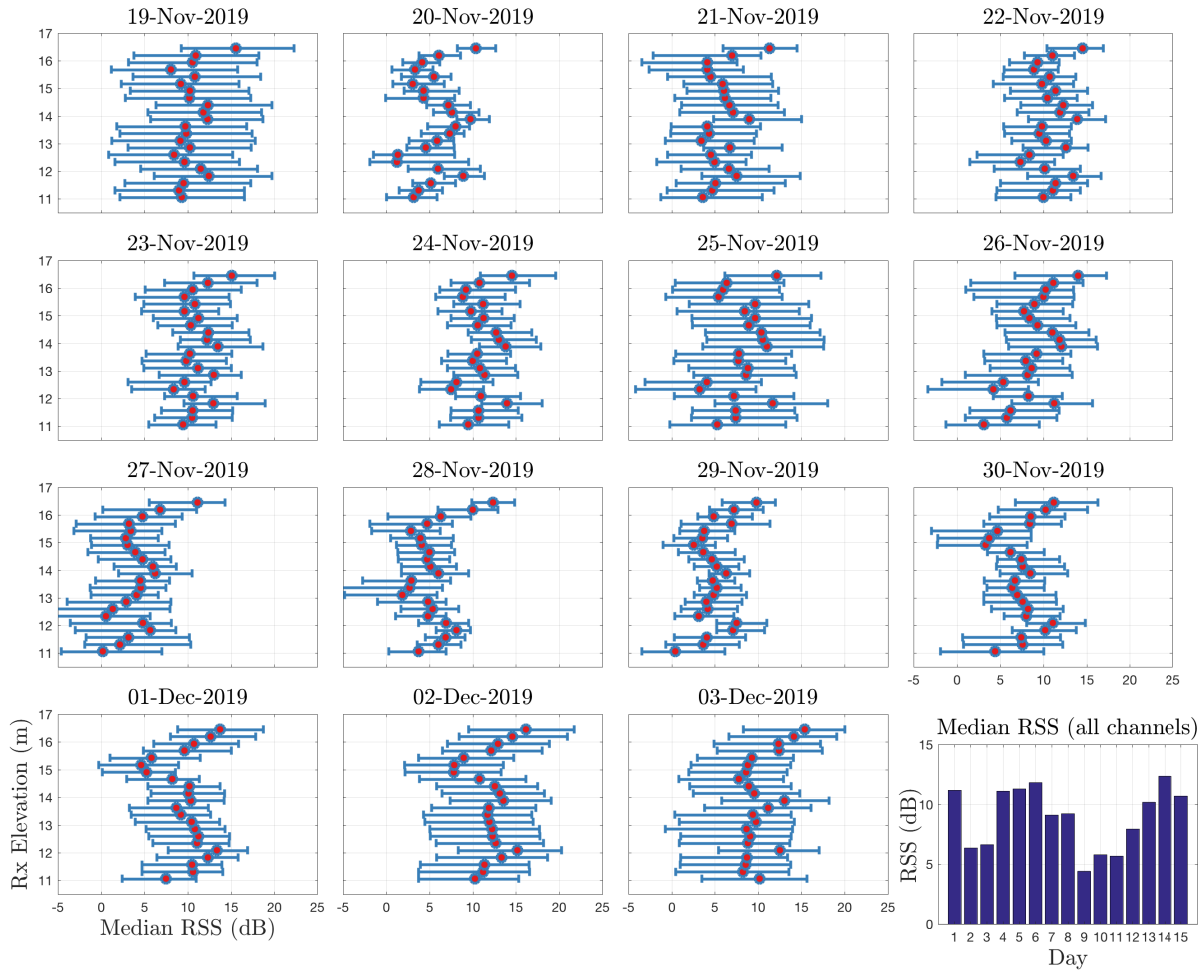**Figure 5.15**: As in Figure 5.12, November 28–30, 2019.

Figure 5.16: As in Figure 5.12, December 01–03, 2019.

Figure 5.17: One hour accumulated precipitation (mm/hour) time evolution, Nov 28, 2019. Black lines indicate the California coastline, red 'x's indicate transmit and receive sites.

Figure 5.18: Daily median received signal strength (RSS) and 10–90% quantile ranges. Each value calculated from 3 channel median RSS across array. Channels 2–22 displayed.

signals propagating over the horizon arrive as a single plane wave at array broadside then RSS should be constant across the array and there would be no benefit to taking measurements at different heights. Figure 5.18 gives the median daily RSS generated as the median of each set of 3 neighboring channels at each time. Clearly there is variation across the array, indicating the signal is actually composed of many plane waves interfering constructively and destructively with one another. Our goal is to determine the DOAs of the signals' multipath components.

Figure 5.19 gives the DOAs found using Gridless DOA estimation the three strongest signal paths. Clearly the direct path around 0° is dominant at all times. Sporadic secondary
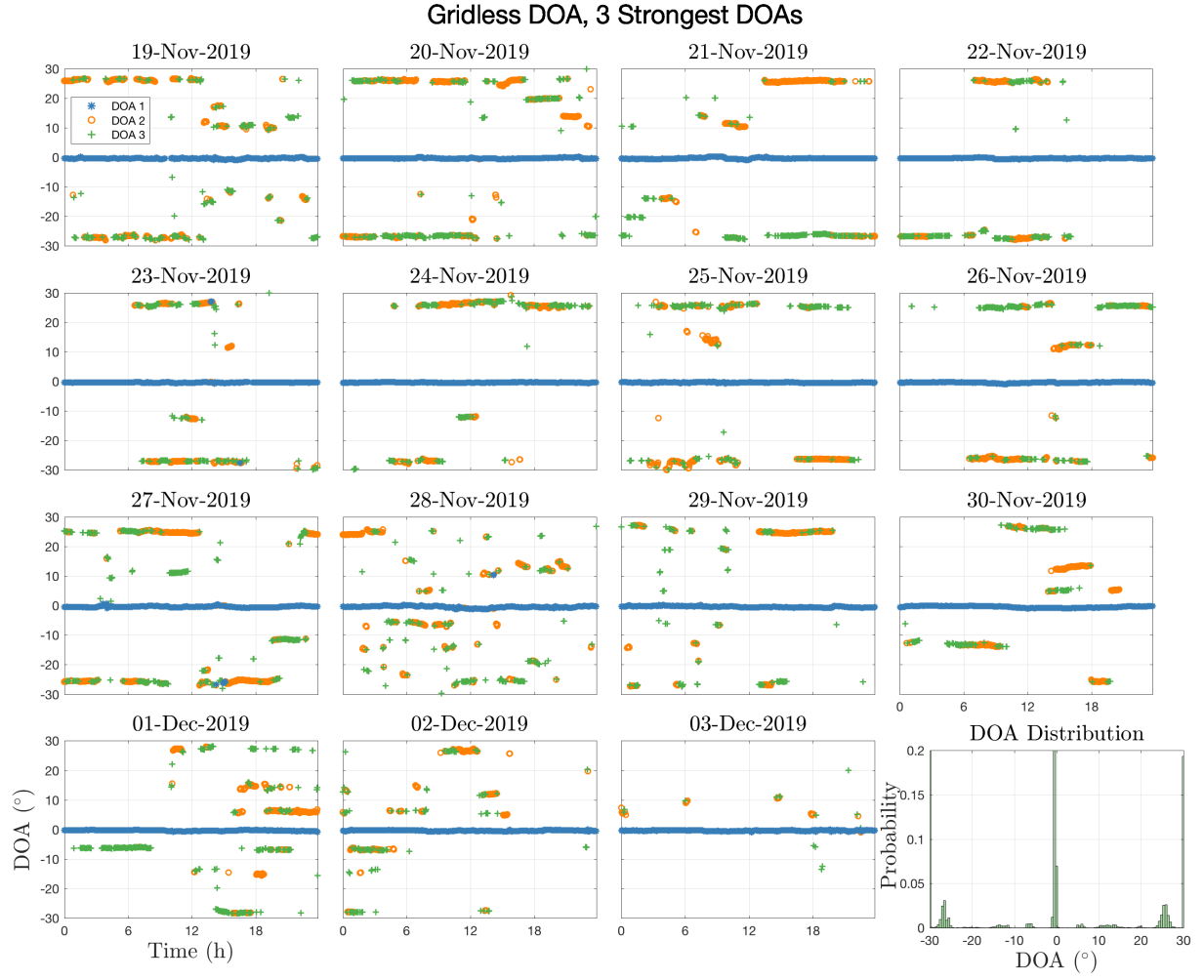
Figure 5.19: Gridless DOA estimation, 3 strongest peaks using gridless DOA.

and tertiary paths appear occasionally, most notably around $+26°$ and $-28°$. It is likely that some secondary paths were very close to the direct path at $0°$, but could not be resolved due to limitations in the resolution capability of DOA estimation. This problem can be solved only by using an array with significantly larger aperture (in wavelengths), which is impractical at DTV frequencies but may be achievable at higher frequencies.

Figure 5.20 compares observed distributions of measurements taken during periods with and without precipitation. Precipitation resulted in a roughly 7 dB decrease in mean ASNR, though the overall ANSR distribution maintained a somewhat bimodal appearance in both cases.
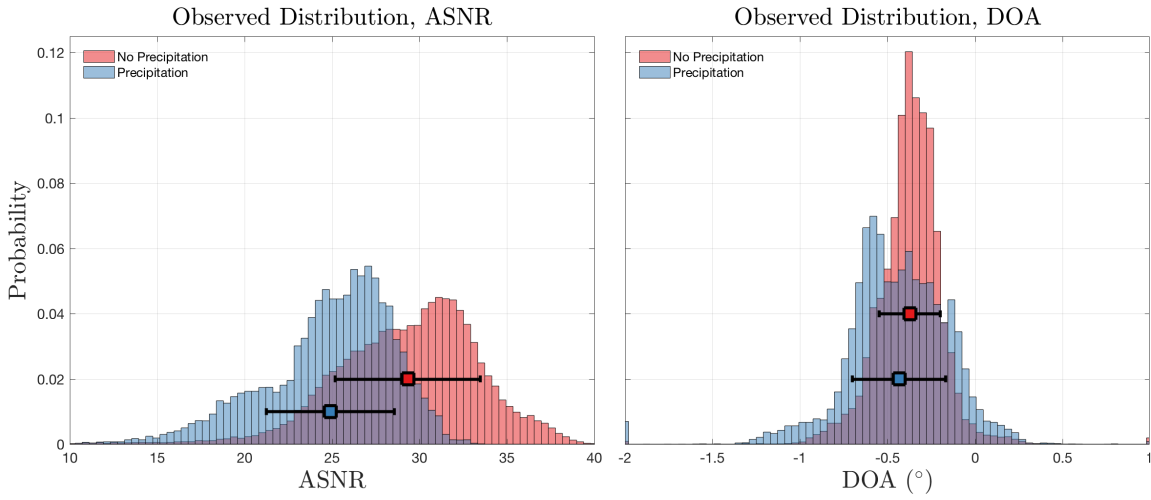
Figure 5.20: Empirical probability distributions (histograms) of ASNR and gridless DOA during periods with and without precipitation. Colored bars indicate mean and standard deviation of each observed distribution.

The dominant DOA (from gridless DOA) is consistently negative, however the magnitude of the negative angle is not significant compared to potential measurement error. For instance, a $0.3°$ deflection from broadside could be caused by $a_r\sin(\theta) = 5.91\sin(0.3) = 3.1$ cm horizontal deviation between the top and bottom receivers.

DOA appears Gaussian distributed during periods without precipitation, but becomes somewhat bimodal during precipitation events. The mean DOA observed during periods of precipitation was shifted by approximately $-0.1°$ against observations made without precipitation. The increase in DOA variance during precipitation is expected as precipitation was shown to decrease the strength of the main signal path, reducing the accuracy of its DOA estimate.

Figure 5.21 gives histograms of RSS for channels 1 and 24, alongside ASNR. Clearly RSS was not constant across the array, and in general increased with transmitter height. ASNR distribution did not closely resemble RSS distribution, and in general exhibited lower variance than RSS. It has previously been demonstrated that RSS across an array can vary significantly for arrays located in refractive channels [26, 47], thus the clear difference between channel 1 and channel 24 is not surprising. What is unexpected is that ASNR is more tightly distributed
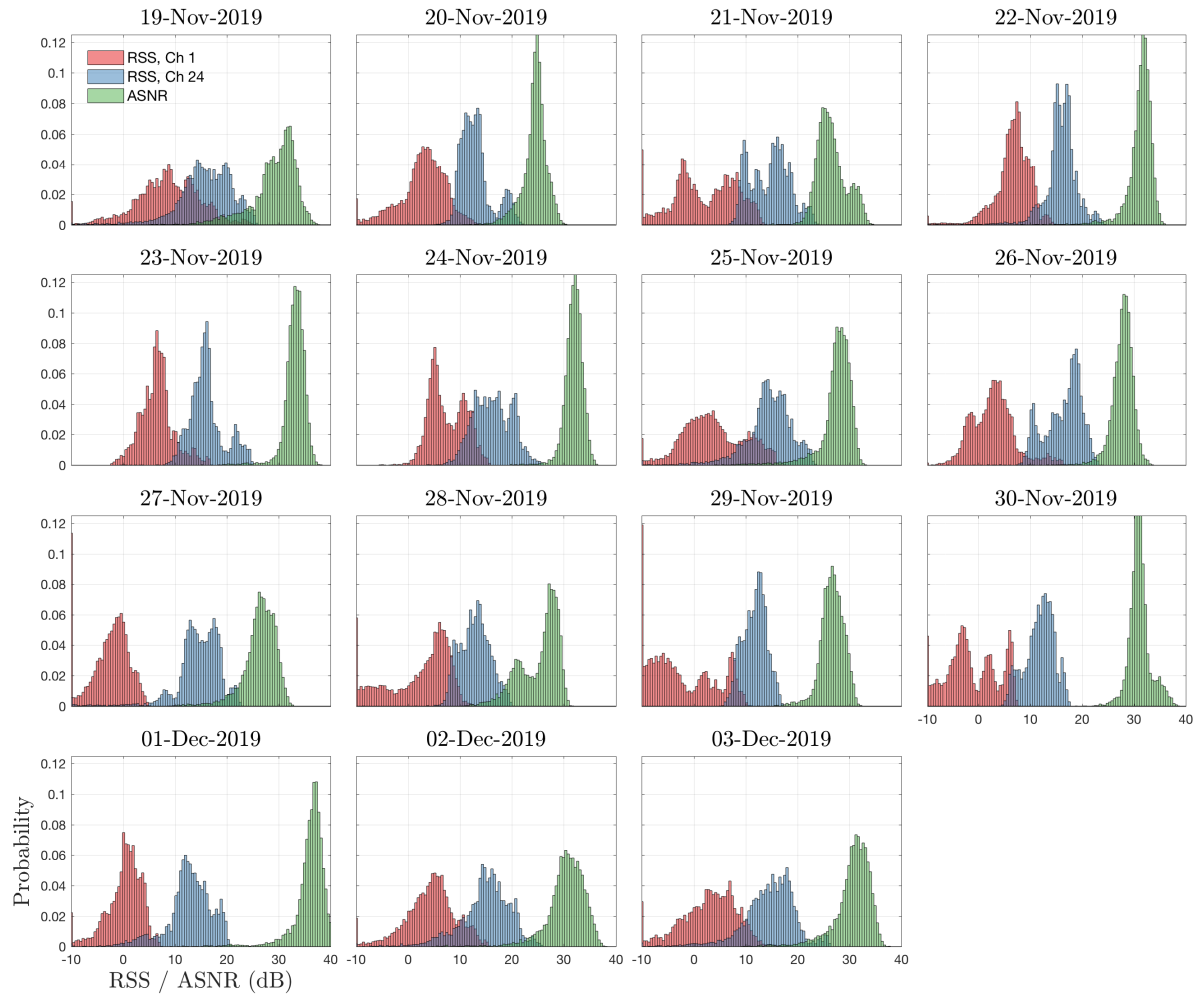
Figure 5.21: Daily empirical probability distributions (histograms) of RSS at receiver elements 1 and 24, and ASNR over full measurement period.

than single channel RSS. This indicates that while the amount of signal energy arriving at a single receiver can fluctuate significantly, the total signal energy arriving across the array is more predictable. Such fluctuations may be the result of atmospheric turbulence, which is known to affect EM propagation [20].

Figure 5.22 gives the correlation coefficient between measurements taken by the array and several atmospheric parameters measured during the campaign. Atmospheric measurements included air temperature, water temperature, barometric pressure, precipitation, wind speed, and
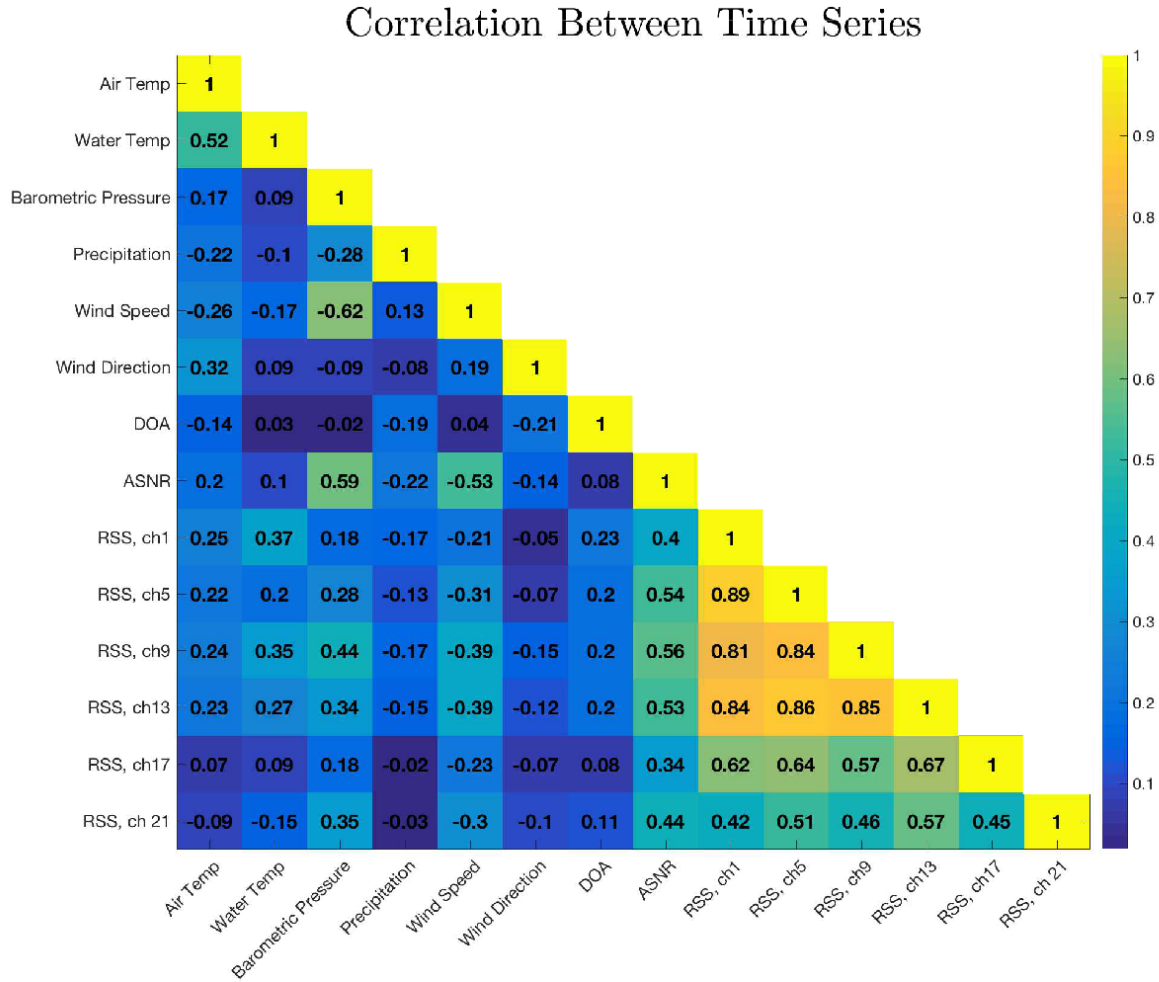
Figure 5.22: Correlation coefficient between atmospheric time series and array time series.

wind direction. All atmospheric measurements were recorded by the NOAA station located on Scripps Pier beside the receiver array, except for precipitation which was provided by NCAR stage IV precipitation maps. Because refractivity affects RF propagation and refractivity is a function of temperature, pressure, and water vapor pressure (see eq. (5.2)) it is reasonable to expect that air temperature and barometric pressure should show some correlation with the array measurements.

The atmospheric measurements with largest correlation to array measurements were ASNR and barometric pressure. Correlation between single element RSS and barometric pressure were significantly lower than that of ASNR and barometric pressure, indicating that ASNR can

provide more information about atmospheric parameters over RSS. Wind speed also demonstrated surprisingly high correlation with ANSR and RSS measurements. We speculate wind speed is a good predictor of evaporation duct height, which in turn influences RSS [48]. The DOA estimated using gridless DOA showed only minor correlation with precipitation, air temperature, and wind direction.

5.5   Summary and Conclusions

A 24 element phase coherent vertical receiver array was set up on the coast of Southern California and set to record the pilot tone from a distant DTV station transmitting OTH relative the receiver array. The goal of the study was to observe variability in array exclusive measurements such as wavefront DOA and ASNR to determine their viability for enhancing refractivity inversion research.

It was found that DOA fluctuations in the DTV signal main path were observable and varied on the order of $1°$. Several DOAs from minor paths were observable, though appeared sporadically and could not be clearly attributed to any atmospheric parameter. ASNR was found to be strongly correlated with barometric pressure and wind speed, significantly more so than single channel RSS. This result strongly suggests that ASNR is a superior predictor of atmospheric refractivity than RSS.

While DOA showed little correlation between atmospheric parameters, it was demonstrated that wavefront DOA can fluctuate measurably over large time scales. Future studies employing larger scale measurement campaigns may reveal more complicated connections between DOA and atmospheric refractivity.

The results of the measurement campaign reported herein mark a preliminary step in incorporating array measurements for prediction of atmospheric refractivity. There is already extensive literature on refractivity estimation from measures of RSS, particularly those taken from

marine radar [49, 12, 13, 14, 15, 30, 19]. This work has demonstrated that refractivity estimation can likely be improved by using ASNR measurements in place of single channel RSS.

5.6   Appendix A: Part Specifications

A list of specific hardware used in the receiver array, depicted in Fig. 5.3. Additional details provided in the data sheets available for each part number.

- **Antennas:** Abracon (APAMSTJ-138) Passive Multiband Antenna.

- **Radios:** Ettus USRP N310 Software Defined Radio.

- **10 MHz Reference:** Novus (NR3623-O) Triple Output 10 MHz OCXO Low Phase Noise PPS Source.

- **Local Oscillator (LO):** Valon 5009 Frequency Synthesizer Module.

- **Splitter 1:** Ettus OctoClock-G CDA-2990.

- **Splitter 2:** ZN6PD1-63-S+ 6-way Power splitter/combiner.

- **Data Server:**

  - CPU: 1 x AMD EPYCTM 7351P Processor (2.4Ghz,155/170W).

  - Memory: 8 x 8GB DDR4 2666 ECC RDIMM Memory.

  - SSD: 24 x SAMSUNG 860 Pro Series 2.5" 1TB SATA III V-NAND 2-bit MLC.

- **Cabling (antenna to radio)**: LMR-240 30 ft SMA male to SMA female Coax.

- **Climate Control:**

  - Dehumidifier: Quest Hi-E Dry 120 Dehumidifier Model 4036730.

  - Air Conditioner: KWIB1411 Portable Water-Cooled Air Conditioner.

5.7 Acknowledgements

Bibliography

[1] H.V. Hitney, J.H. Richter, R.A. Pappert, K.D. Anderson, and G.B. Baumgartner, "Tropospheric radio propagation assessment," *Proceedings of the IEEE*, vol. 73, no. 2, pp. 265–283, 1985.

[2] S.M. Babin, G.S. Young, and J.A. Carton, "A new model of the oceanic evaporation duct," *J. Applied Meteorology*, vol. 36, no. 3, pp. 193–204, 1997.

[3] R.A. Pappert and C.L. Goodhart, "Case studies of beyond-the-horizon propagation in tropospheric ducting environments," *Radio Sci.*, vol. 12, no. 1, pp. 75–87, 1977.

[4] V.W. Pidgeon, "Frequency dependence of radar ducting," *Radio Sci.*, vol. 5, no. 3, pp. 541–549, 1970.

[5] K.D. Anderson, "Radar detection of low-altitude targets in a maritime environment," *IEEE Trans. Antennas. Prop.*, vol. 43, no. 6, pp. 609–613, 1995.

[6] C.Y.D. Sim and E.M. Warrington, "Signal strength measurements at frequencies of around 300 mhz over two sea paths in the british channel islands," *Radio Sci.*, vol. 41, no. 03, pp. 1–13, 2006.

[7] W.T. Thompson and T. Haack, "An investigation of sea surface temperature influence on microwave refractivity: The wallops-2000 experiment," *J. Appl. Meteorol. Climatol.*, vol. 50, no. 11, pp. 2319–2337, 2011.

[8] Q. Wang, D.P. Alappattu, S. Billingsley, B. Blomquist, R.J. Burkholder, A.J. Christman, E.D. Creegan, T. De Paolo, D.P. Eleuterio, and H.J.S. Fernando, "Casper: Coupled air–sea processes and electromagnetic ducting research," *Bulletin of the American Meteorological Society*, vol. 99, no. 7, pp. 1449–1471, 2018.

[9] G.D. Dockery, "Modeling electromagnetic wave propagation in the troposphere using the parabolic equation," *IEEE Trans. Antennas. Prop.*, vol. 36, no. 10, pp. 1464–1470, 1988.

[10] A.E. Barrios, "A terrain parabolic equation model for propagation in the troposphere," *IEEE Trans. Antennas. Prop.*, vol. 42, no. 1, pp. 90–98, 1994.

[11] D.J. Thomson and N.R. Chapman, "A wide-angle split-step algorithm for the parabolic equation," *J. Acoust. Soc. Am.*, vol. 74, no. 6, pp. 1848–1854, 1983.

[12] D.F. Gingras, P. Gerstoft, and N.L. Gerr, "Electromagnetic matched-field processing: Basic concepts and tropospheric simulations," *IEEE Trans. Antennas. Prop.*, vol. 45, no. 10, pp. 1536–1545, 1997.

[13] P. Gerstoft, D.F. Gingras, L.T. Rogers, and W.S. Hodgkiss, "Estimation of radio refractivity structure using matched-field array processing," *Antennas and Propagation, IEEE Transactions on*, vol. 48, no. 3, pp. 345–356, 2000.

[14] P. Gerstoft, L.T. Rogers, J.L. Krolik, and W.S. Hodgkiss, "Inversion for refractivity parameters from radar sea clutter," *Radio science*, vol. 38, no. 3, 2003.

[15] C. Yardim, P. Gerstoft, and W.S. Hodgkiss, "Estimation of radio refractivity from radar clutter using Bayesian Monte Carlo analysis," *IEEE Trans. Antennas. Prop.*, vol. 54, no. 4, pp. 1318–1327, 2006.

[16] C. Yardim, P. Gerstoft, and W.S. Hodgkiss, "Sensitivity analysis and performance estimation of refractivity from clutter techniques," *Radio Science*, vol. 44, no. 1, pp. 1058–1070, 2009.

[17] S.E. Penton and E.E. Hackett, "Rough ocean surface effects on evaporative duct atmospheric refractivity inversions using genetic algorithms," *Radio Sci.*, vol. 53, no. 6, pp. 804–819, 2018.

[18] M.A. Gilles, C. Earls, and D. Bindel, "A subspace pursuit method to infer refractivity in the marine atmospheric boundary layer," *IEEE Trans. Geosci. Remote Sens.*, vol. 57, no. 8, pp. 5606–5617, 2019.

[19] A. Karimian, C. Yardim, P. Gerstoft, W.S. Hodgkiss, and A.E. Barrios, "Refractivity estimation from sea clutter: An invited review," *Radio Sci.*, vol. 46, no. 06, pp. 1–16, 2011.

[20] M. Wagner, P. Gerstoft, and T. Rogers, "Estimating refractivity from propagation loss in turbulent media," *Radio Sci.*, vol. 51, no. 12, pp. 1876–1894, 2016.

[21] G.B. Baumgartner, H.V. Hitney, and R.A. Pappert, "Duct propagation modelling for the integrated-refractive-effects prediction system (ireps)," in *IEEE Proc. F (Comm., Radar and Sig. Process.)*. IET, 1983, vol. 130, pp. 630–642.

[22] A. Barrios, "Estimation of surface-based duct parameters from surface clutter using a ray trace approach," *Radio Sci.*, vol. 39, no. 6, 2004.

[23] H.W. Ko, J.W. Sari, and J.P. Skura, "Anomalous microwave propagation through atmospheric ducts," *JHATD*, vol. 4, pp. 12–26, 1983.

[24] H.V. Hitney, "Refractive effects from vhf to ehf. part a: Propagation mechanisms," *PMDA*, 1994.

[25] D. Crouse, "Basic tracking using nonlinear 3d monostatic and bistatic measurements in refractive environments," *IEEE Aerospace and Electronic Systems Magazine*, vol. 29, no. 8, pp. 54–75, 2014.

[26] M. Wagner, S. Nannuru, and P. Gerstoft, "Compressive MIMO beamforming of data collected in a refractive environment," *Radio Sci.*, vol. 52, no. 12, pp. 1458–1471, 2017.

[27] V.I. Tatarski, *Wave propagation in a turbulent medium*, McGraw-Hill, 1961.

[28] Q. Wang, K. Franklin, R. Yamaguchi, D.G. Ortiz-Suslow, D.P. Alappattu, C. Yardim, and R. Burkholder, "Ducting conditions during casper-west field campaign," in *2018 IEEE International Symposium on Antennas and Propagation*. IEEE, 2018, pp. 877–878.

[29] Q. Zhang, K. Yang, and Y. Shi, "Spatial and temporal variability of the evaporation duct in the gulf of aden," *Tellus A*, vol. 68, no. 1, pp. 29792, 2016.

[30] C. Yardim, P. Gerstoft, and W.S Hodgkiss, "Tracking refractivity from clutter using Kalman and particle filters," *IEEE Trans. Antennas. Prop.*, vol. 56, no. 4, pp. 1058–1070, 2008.

[31] G. Kizer, *Digital microwave communication: engineering point-to-point microwave systems*, John Wiley and Sons, 2013.

[32] P. Lopez, "A 5-yr 40-km-resolution global climatology of superrefraction for ground-based weather radars," *J. Appl. Meteorol. Climatol.*, vol. 48, no. 1, pp. 89–110, 2009.

[33] D. Chu, "Polyphase codes with good periodic correlation properties (corresp.)," *IEEE Transactions on information theory*, vol. 18, no. 4, pp. 531–532, 1972.

[34] H.L. Van Trees, *Optimum array processing: Part IV of detection, estimation, and modulation theory*, John Wiley & Sons, 2004.

[35] Y. Qu, G. Liao, S.Q. Zhu, X.Y. Liu, and H. Jiang, "Performance analysis of beamforming for MIMO radar," *Prog. Electromagn. Res.*, vol. 84, pp. 123–134, 2008.

[36] F. Quitin, M.U. Rahman, R. Mudumbai, and U. Madhow, "Distributed beamforming with software-defined radios: frequency synchronization and digital feedback," in *2012 IEEE Global Communications Conference (GLOBECOM)*. IEEE, 2012, pp. 4787–4792.

[37] P. Gerstoft, A. Xenaki, and C.F. Mecklenbräuker, "Multiple and single snapshot compressive beamforming," *J. Acoust. Soc. Am.*, vol. 138.4, pp. 2003–2014, 2015.

[38] G. Tang, B.N. Bhaskar, P. Shah, and B. Recht, "Compressed sensing off the grid," *IEEE Trans. Inf. Theory*, vol. 59, no. 11, pp. 7465–7490, 2013.

[39] Z. Yang and L. Xie, "On gridless sparse methods for line spectral estimation from complete and incomplete data," *IEEE Trans. Signal Process.*, vol. 63, no. 12, pp. 3139–3153, 2015.

[40] Y. Li and Y. Chi, "Off-the-grid line spectrum denoising and estimation with multiple measurement vectors," *IEEE Trans. Signal. Process.*, vol. 64, no. 5, pp. 1257–1269, 2016.

[41] Z. Yang, J. Li, P. Stoica, and L. Xie, "Chapter 11 - sparse methods for direction-of-arrival estimation," in *Academic Press Library in Signal Processing, Volume 7*, R. Chellappa and S. Theodoridis, Eds., pp. 509 – 581. Academic Press, 2018.

[42] T.L. Hansen, B.H. Fleury, and B.D. Rao, "Superfast line spectral estimation," *IEEE Trans. Sig. Proc.*, vol. 66, no. 10, pp. 2511–2526, 2018.

[43] S. Boyd and L. Vandenberghe, *Convex optimization*, Cambridge University Press, 2004.

[44] J. Van de Beek, M. Sandell, and P.O. Borjesson, "Ml estimation of time and frequency offset in ofdm systems," *IEEE Trans. Sig. Proc.*, vol. 45, no. 7, pp. 1800–1805, 1997.

[45] Y Lin, "GCIP/EOP surface: Precipitation NCEP/EMC 4km gridded data (GRIB) stage IV data. version 1.0. UCAR/NCAR-earth observing laboratory," 2011.

[46] X. Zhao, "Evaporation duct height estimation and source localization from field measurements at an array of radio receivers," *IEEE Trans. Antennas. Prop.*, vol. 60, no. 2, pp. 1020–1025, 2011.

[47] J. Pozderac, J. Johnson, C. Yardim, C. Merrill, T. de Paolo, E. Terrill, F. Ryan, and P. Frederickson, "*x*-band beacon-receiver array evaporation duct height estimation," *IEEE Trans. Antennas. Prop.*, vol. 66, no. 5, pp. 2545–2556, 2018.

[48] P.A. Frederickson, "Software design description for the navy atmospheric vertical surface layer model (NAVSLaM) csci, version 1.0," *Prepared for the Naval Oceanographic Office, Systems Integration Division*, p. 36, 2010.

[49] F. Fabry, C. Frush, I. Zawadzki, and A. Kilambi, "On the extraction of near-surface index of refraction using radar phase measurements from ground targets," *J. Atmos. and Ocean Tech.*, vol. 14, no. 4, pp. 978–987, 1997.

Chapter 6

Conclusions and Future Work

As has been long predicted, our measurements confirm that the DOA of EM signals propagating over the horizon through a refractive channel do change over time. Despite advances in DOA estimation algorithms, even the most classic technique of CBF can be used to detect this change given the array hardware can produce sufficient measurements. Due to the broad scope of this work, it is difficult to reach succinct conclusions that summarize the work as a whole. Instead, a list of conclusions over range of subtopics is provided in the proceeding section.

6.1   Conclusions

The conclusions provided here are itemized in order of the works covered in this dissertation, from chapter 2 through chapter 5. Some elements from conclusions made in one chapter may be repeated in another chapter when relevant.

6.1.1   Conclusions: Chapter 2

The effects of turbulence on refractivity inversion were explored. A model for including turbulence in parabolic equation simulation of propagation loss was proposed, then refractivity

inversion was attempted on simulated propagation loss measurements including turbulence. Conclusions are as follows:

- The Parabolic Equation model for EM propagation simulation is limited in accuracy for long range propagation prediction due to the effects of turbulence. The effects of slight variation in the atmospheric refractivity profile at one range cascade into large differences in estimated PL at long ranges.

- The genetic algorithm is not an efficient or reliable tool for refractivity inversion. The issue of how to invert between a forward model and refractivity is still an open question. The main obstacle is the non-convex nature of the forward model.

- It is far easier to invert for strong surface based duct conditions because these conditions have the largest impact on propagation loss, however surface based ducts make up only a small fraction of the actual ducts observed.

- Correct description and modeling of turbulence is important for improving refractivity inversion. By defining the expected error due to turbulence it may be possible to construct bounds on the likelihood of correct estimation of the refractivity profile.

6.1.2   Conclusions: Chapter 3

MIMO measurements from a communication channel in a refractive environment were evaluated using compressive sensing based DOA estimation techniques. Conclusions are as follows:

- MIMO communications arrays offer an improved method of estimating DOA of over the horizon signals by allowing for direction of departure estimation in addition to direction of arrival estimation.

164

- Compressive DOA estimation adds improved resolution over conventional 2D DOA estimation techniques such as CBF and MUSIC.

- Compressive DOA estimation is limited by several factors, including grid mismatch and computational complexity.

- The measurements clearly depicted a fluctuating communications channel with several distinct directions of departure and arrival.

- Larger scale MIMO systems are necessary for higher fidelity measurements of the evolving refractive channel.

6.1.3 Conclusions: Chapter 4

An algorithm for gridless DOA estimation of measurements from a non-uniform array of known geometry was developed and evaluated. Conclusions are as follows:

- Root-MUSIC, commonly thought to apply only to measurements from uniform linear arrays, is suitable for measurements from non-uniform arrays with only minor generalizations of background theory.

- The concept of Vandermonde decomposition of a Toeplitz matrix can be generalized to decompose 'irregular Toeplitz matrices' to 'irregular Vandermonde matrices'. The union of all sets of irregular Toeplitz matrices is the set of positive semi-definite matrices. The decomposition is likely not unique, though the number of decompositions of an irregular Toeplitz matrix producing low rank irregular Vandermonde matrices is typically only one.

- Alternating projections (AP) is suitable for solving rank minimization optimizations with high likelihood of convergence to the correct solution. The AP algorithm has the same computational complexity as the best (known) solution using convex relaxation of the problem, but is conceptually simpler and can be extended to non-uniform array geometries.

- The extension to non-uniform array geometries results in only minor decreases in DOA estimation performance.

6.1.4   Conclusions: Chapter 5

A phase coherent EM array was constructed to record the carrier tone of a digital television (DTV) station broadcast from 168 km away. DOA estimation was performed on the array measurements and a 15 day history of fluctuations in the DOA was recorded. Conclusions are as follows:

- The DOA of signals propagating over the horizon through a refractive environment does fluctuate on the scale of hours to days.

- The total DOA fluctuations were on the order of $.75°$, which means that any array deployed for such measurements should be designed such that it can detect sub $1°$ fluctuations, i.e. the array aperture should be very large relative the signal wavelength.

- Precipitation appears to be the dominant factor determining DOA.

- DOA and SNR were not well correlated, indicating that DOA may be a useful secondary parameter for refractivity inversion over propagation loss.

6.2   Future Work

In some sense, the research presented in this dissertation is only a small piece of work in the larger literature on refractivity estimation. Towards the goal of full incorporation of signal DOA into refractivity inversion, this is an early text showing that the concept holds merit. We have demonstrated that signal DOA is in fact a parameter that can be measured practically alongside propagation loss, and is sufficiently independent of propagation loss that it may confer additional information useful for inferring the refractivity profile along the channel path.

There is a long list of future studies which must now be conducted. Firstly, we have demonstrated that DOA is variable within a refractive channel, but only for one single channel. There are many variables describing a communications channel, including but not limited to:

- signal frequency and bandwidth

- transmitter and receiver hardware specifications

- location of channel and medium of propagation

- propagation distance and terrain within the channel

- weather conditions within the channel.

The study detailed in chapter 5 must be repeated in many different channels over a range of conditions listed above to better detail how DOA is affected by the different parameters.

Most importantly, refractivity within the propagation channel should be recorded in high detail to determine a relationship between the DOA and refractivity profile. Simultaneously, modeling software must be advanced to give realistic estimates of the DOA experienced by a receiver array at any given point. When simulation and reality are well matched DOA measurements can enhance refractivity predictions. Then it is a matter of developing efficient algorithms that can map between DOA/PL and refractivity. Advances in machine learning may be key in this issue.

Finally, it is technically challenging to develop an array system capable of measuring signal DOA using modern hardware. The evolution of better tools, such as software defined radios specifically designed to operate multiple channels coherently, is important to promote smaller scale research by institutions that do not have access to prohibitively expensive equipment.